Corrosion Resistant Alloys for Reinforced Concrete

PUBLICATION NO. FHWA-HRT-07-039

JULY 2007

U.S. Department of Transportation
Federal Highway Administration

Research, Development, and Technology
Turner-Fairbank Highway Research Center
6300 Georgetown Pike
McLean, VA 22101-2296

Foreword

Initial cost considerations have historically precluded widespread utilization of high performance (corrosion resistant) reinforcements such as stainless steels in bridge construction. However, with the advent of life-cycle cost analysis as a project planning tool and of a requirement that major bridge structures have a 75- to 100-year design life, the competitiveness of such steels has increased such that enhanced attention has focused in recent years upon these materials.

This investigation was initiated to evaluate the corrosion resistance of various types of corrosion resistant reinforcement, including new products that are becoming available, in bridge structures that are exposed to chlorides. Both long-term (4-year) test yard exposures and accelerated laboratory experiments in simulated concrete pore waters are being performed. The ultimate objective is to, first, evaluate the corrosion properties and rank the different candidate materials and, second, develop tools whereby long-term performance in actual structures can be projected from short-term tests. This interim report presents results from the initial 3 years of an overall 5-year program.

Gary L. Henderson
Director, Office of Infrastructure
Research and Development

Notice

Quality Assurance Statement

The Federal Highway Administration (FHWA) provides high-quality information to serve Government, industry, and the public in a manner that promotes public understanding. Standards and policies are used to ensure and maximize the quality, objectivity, utility, and integrity of its information. FHWA periodically reviews quality issues and adjusts its programs and processes to ensure continuous quality improvement.

Technical Report Documentation Page

1. Report No.	2. Government Accession No.	3. Recipient's Catalog No.
FHWA-HRT-07-039		

4. Title and Subtitle	5. Report Date
Corrosion Resistant Alloys for Reinforced Concrete	July 2007
	6. Performing Organization Code FAU-OE-CMM-0601

7. Author(s)	8. Performing Organization Report No.
William H. Hartt,* Rodney G. Powers,** Diane K. Lysogorski,* Virginie Liroux,* Y. Paul Virmani*** (See Boxes 9 and 12)	

9. Performing Organization Name and Address	10. Work Unit No. (TRAIS)
*Florida Atlantic University—Sea Tech Campus, 101 North Beach Road, Dania Beach, FL 33004 **Florida Department of Transportation—State Materials Office, 5007 NE 39th Street, Gainesville, FL 32609	11. Contract or Grant No.

12. Sponsoring Agency Name and Address	13. Type of Report and Period Covered
***Office of Infrastructure Research and Development Federal Highway Administration 6300 Georgetown Pike McLean, VA 22012	Interim Report
	14. Sponsoring Agency Code

15. Supplementary Notes

Contracting Officer's Technical Representative (COTR): Y.P. Virmani, HRDI-10

16. Abstract

Infrastructure deterioration, which includes corrosion of reinforcing steel in concrete bridges, has been identified as a major economic and societal cost to the United States. For the past 30 years, epoxy-coated reinforcing steel (ECR) has been specified for reinforced concrete bridges exposed to deicing salts and coastal environments. Premature corrosion induced cracking of marine bridge substructures in Florida indicated, however, that ECR is of little benefit for this type of exposure; and while performance of ECR in northern bridge decks has been generally good to-date (30-plus years), still the degree of corrosion resistance to be afforded in the long term to major structures with design lives of 75 to 100 years is uncertain. This concern, combined with increased utilization of life-cycle cost analysis in project planning and materials selection, has caused renewed interest in corrosion resistant reinforcements, stainless steels in particular. The present research study is being performed jointly by Florida Atlantic University and the Florida Department of Transportation to evaluate alloys that have been identified as candidate corrosion resistant reinforcements. These include MMFX-II™ (ASTM A 1035), solid stainless steels 3Cr12 (UNS-S41003), 2201LDX (ASTM A955-98), 2205 (UNS 31803), and two 316L (UNS S31603) alloys; and two 316 stainless steel clad black bar products. Black bar (ASTM A615) reinforcement was included for comparison purposes. Testing methods included three types of short-term exposures: (1) a previously developed method that involves cyclic exposure to synthetic pore solution (SPS) with incrementally increasing chlorides and then to moist air, (2) anodic potentiostatic exposure in SPS with incrementally increasing chlorides, and (3) potentiodynamic polarization scans in saturated $Ca(OH)_2$ at different chloride concentrations. Long-term exposures involve four specimen types: (1) simulated deck slabs, (2) 3-bar columns, (3) macro-cell slab specimens, and (4) field columns. Specimen types (1) and (3) are being cyclically wet-dry ponded with a sodium chloride (NaCl) solution and are intended to simulate northern bridge decks exposed to deicing salts, whereas types (2) and (4) are partially submerged continuously, the former in a NaCl solution and the latter at a coastal marine site in Florida. This report details findings for the initial 3 years of this 5 year project.

17. Key Word	18. Distribution Statement
Reinforced concrete, bridges, corrosion resistance, corrosion testing, high performance reinforcement, stainless steel, MMFX-II™	No restrictions. This document is available to the public through NTIS, Springfield, VA 22161

19. Security Classif. (of this report)	20. Security Classif. (of this page)	21. No. of Pages	22. Price
Unclassified	Unclassified	132	

Form DOT F 1700.7 (8-72) **Reproduction of completed page authorized**

SI* (MODERN METRIC) CONVERSION FACTORS

APPROXIMATE CONVERSIONS TO SI UNITS

Symbol	When You Know	Multiply By	To Find	Symbol
		LENGTH		
in	inches	25.4	millimeters	mm
ft	feet	0.305	meters	m
yd	yards	0.914	meters	m
mi	miles	1.61	kilometers	km
		AREA		
in^2	square inches	645.2	square millimeters	mm^2
ft^2	square feet	0.093	square meters	m^2
yd^2	square yard	0.836	square meters	m^2
ac	acres	0.405	hectares	ha
mi^2	square miles	2.59	square kilometers	km^2
		VOLUME		
fl oz	fluid ounces	29.57	milliliters	mL
gal	gallons	3.785	liters	L
ft^3	cubic feet	0.028	cubic meters	m^3
yd^3	cubic yards	0.765	cubic meters	m^3
	NOTE: volumes greater than 1000 L shall be shown in m^3			
		MASS		
oz	ounces	28.35	grams	g
lb	pounds	0.454	kilograms	kg
T	short tons (2000 lb)	0.907	megagrams (or "metric ton")	Mg (or "t")
		TEMPERATURE (exact degrees)		
^oF	Fahrenheit	5 (F-32)/9 or (F-32)/1.8	Celsius	^oC
		ILLUMINATION		
fc	foot-candles	10.76	lux	lx
fl	foot-Lamberts	3.426	candela/m^2	cd/m^2
		FORCE and PRESSURE or STRESS		
lbf	poundforce	4.45	newtons	N
lbf/in^2	poundforce per square inch	6.89	kilopascals	kPa

APPROXIMATE CONVERSIONS FROM SI UNITS

Symbol	When You Know	Multiply By	To Find	Symbol
		LENGTH		
mm	millimeters	0.039	inches	in
m	meters	3.28	feet	ft
m	meters	1.09	yards	yd
km	kilometers	0.621	miles	mi
		AREA		
mm^2	square millimeters	0.0016	square inches	in^2
m^2	square meters	10.764	square feet	ft^2
m^2	square meters	1.195	square yards	yd^2
ha	hectares	2.47	acres	ac
km^2	square kilometers	0.386	square miles	mi^2
		VOLUME		
mL	milliliters	0.034	fluid ounces	fl oz
L	liters	0.264	gallons	gal
m^3	cubic meters	35.314	cubic feet	ft^3
m^3	cubic meters	1.307	cubic yards	yd^3
		MASS		
g	grams	0.035	ounces	oz
kg	kilograms	2.202	pounds	lb
Mg (or "t")	megagrams (or "metric ton")	1.103	short tons (2000 lb)	T
		TEMPERATURE (exact degrees)		
^oC	Celsius	1.8C+32	Fahrenheit	^oF
		ILLUMINATION		
lx	lux	0.0929	foot-candles	fc
cd/m^2	candela/m^2	0.2919	foot-Lamberts	fl
		FORCE and PRESSURE or STRESS		
N	newtons	0.225	poundforce	lbf
kPa	kilopascals	0.145	poundforce per square inch	lbf/in^2

*SI is the symbol for the International System of Units. Appropriate rounding should be made to comply with Section 4 of ASTM E380.
(Revised March 2003)

TABLE OF CONTENTS

LIST OF FIGURES

LIST OF TABLES

1. INTRODUCTION

The United States has a major investment in its highway system, the operational performance of which, in conjunction with that of other transportation modes, is critical to the Nation's economic health and societal functionality. While deterioration of structures with time is a normal and expected occurrence, the rate at which this has occurred for highway bridges since advent in the 1960s of a clear roads policy, as affected by winter application of deicing salts in northern locations, has been abnormally advanced and has posed significant challenges, both economically and technically. Also important is similar advanced deterioration of reinforced concrete bridges in coastal locations, both northern and southern, as a consequence of sea water or spray exposure. In both cases (deicing salts and marine exposure), the deterioration is a consequence of the aggressive nature of the chloride ion in combination with moisture and oxygen.[1] Over half of the total bridge inventory in the United States is of the reinforced concrete type, and these structures have proved to be particularly susceptible. A recent study[2] has indicated that the annual direct cost of corrosion to bridges is $5.9 to $9.7 billion. If indirect factors are included also, this cost can be as much as 10 times higher.[3]

As this problem has manifested itself during the past 40 or so years, technical efforts have been directed towards, first, understanding the deterioration mechanism and, second, developing prevention and intervention strategies. With regard to the former, steel and concrete are in most aspects mutually compatible, as exemplified by the fact that, in the absence of chlorides, the relatively high pH of concrete pore solution (pH ≈ 13.0-13.8) promotes formation of a protective oxide (passive) film such that corrosion rate is negligible and decades of relatively low maintenance result. In the presence of chlorides, even at concentrations at the steel depth as low as 0.6 kilograms per cubic meter ($kg/m^{3)}$ (1.0 pound per cubic yard (lb/yd^3)) (concrete weight basis),[4] the passive film may become locally disrupted and active corrosion commence. Once this occurs, solid corrosion products form progressively near the steel-concrete interface and lead ultimately to concrete cracking and spalling. Figure 1.1 shows a photograph illustrating such damage for the case of a coastal bridge piling. Because corrosion induced deterioration is progressive, inspections for damage assessment must be performed routinely; and present Federal guidelines require a visual inspection every 2 years.[5] If indicators of deterioration are not addressed, then public safety is at risk. As an example, corrosion induced concrete spalls occur as potholes in a bridge deck and contribute to unsafe driving conditions. In the extreme, structural failure and collapse result.

Figure 1.1. Photo. Cracked and spalled marine bridge piling.

Corrosion induced deterioration of reinforced concrete can be modeled in terms of three component steps: (1) time for corrosion initiation, T_i, (2) time, subsequent to corrosion initiation, for appearance of cracking on the external concrete surface (crack propagation), T_p, and (3) time for surface cracks to progress into further damage and develop into spalls, T_d, to the point where, if repairs and rehabilitations are not performed, the functional service life, T_f, is reached.[6] Figure 1.2 illustrates these parameters schematically as a plot of cumulative damage versus time. Of the three component terms, T_i normally occupies the longest period and, as such, is the predominant factor in determining useful service life. Based upon the corrosion deterioration model represented by figure 1.2, methods of life-cycle cost analysis (LCCA) are now commonly employed to evaluate and compare different materials selection and design alternatives. This approach considers both initial cost and the projected life history of maintenance, repair, and rehabilitation that are required until the design life is reached. These are evaluated in terms of the time value of money, from which present worth is determined; and comparisons between different options can then be made on a cost normalized basis.

In the early 1970s, research studies were performed that qualified epoxy-coated reinforcing steel (ECR) as an alternative to black bar;[7,8] and for the past 30 years ECR has been specified by most State Departments of Transportation (DOTs) for bridge decks and substructures exposed to chlorides. At the same time, ECR was augmented by use of low water-to-cement ratio (w/c) concrete, possibly with pozzolans or corrosion inhibitors (or both), and concrete covers of 65 millimeters (mm) or more.[9] However, premature corrosion induced cracking of marine bridge substructures in Florida[10,11,12,13] indicated that ECR is of little benefit for this type of exposure; and while performance of ECR in northern bridge decks has been generally good to-date (30-plus years), still the degree of corrosion resistance afforded in the long term for major structures with design lives of 75 to 100 years is uncertain. In response to this, interest has focused during the past decade upon more corrosion resistant alternatives to ECR, stainless steels in particular.

Such corrosion resistant steels become particularly competitive on a life-cycle cost basis, since the higher initial expense of the steel per se may be recovered over the life of the structure via reduced repairs and rehabilitations.

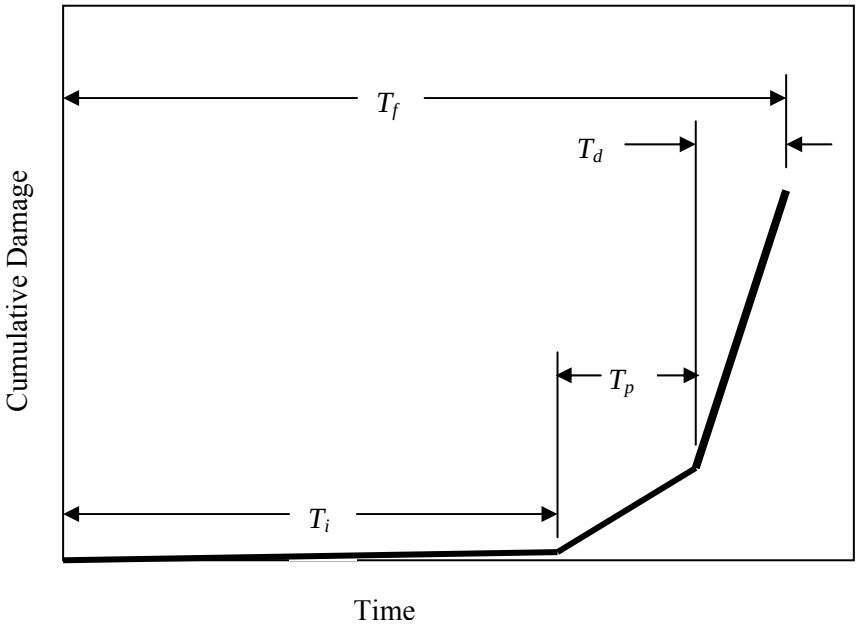

Figure 1.2. Schematic illustration. Various steps in deterioration of reinforced concrete due to chloride induced corrosion.

The present research study is being performed jointly by Florida Atlantic University and the Florida Department of Transportation as a 6-year effort to evaluate the suitability of various corrosion resistant reinforcements for bridges exposed to chlorides. An initial phase of the study provided a critical literature review of corrosion resistant reinforcements.[14] The present report details research findings during the initial 3 years of the project.

2. PROJECT OBJECTIVES

Objectives for this research are as listed below:

I. Determine the extent to which high performance metallic reinforcement has been employed in reinforced concrete bridges and other construction and critically review its performance.

II. Identify candidate high performance metallic reinforcement types that are appropriate for concrete bridge construction.

III. Perform an experimental program that consists of (1) accelerated short-term screening tests and (2) service realistic long-term exposures to establish data from which selection and service life of high performance metallic reinforcement in concrete can be projected.

IV. Analyze the data from III and identify the utility and limitations of employing specific high performance metallic reinforcement in concrete bridge construction.

The purpose of this report is to document accomplishments for the initial 3 years of this 6-year overall effort. Results pertaining to Objective I have been reported elsewhere, as noted above.[14] Progress for Objectives II through IV is described below.

3. EXPERIMENTAL PROCEDURE

ACCELERATED SCREENING TESTS

General

Three categories of accelerated screening tests (ASTs)—wet-dry cycling (AST-1), chloride (Cl^-) threshold determinations (AST-2A), and pitting potential determinations (AST-2B)—were performed. The first of these, AST-1, was modeled after an earlier program[15] and focused upon measurement of corrosion rate of rebar specimens upon exposure to repetitive 1.75 hours wet—4.25 hours dry cycles for a total of 84 days. The test solution was 0.30N potassium hydroxide (KOH)—0.05N sodium hydroxide (NaOH) (pH ~ 13.40) simulated pore water that contained 3.00 weight percent (w/o) sodium chloride (NaCl) (1.82 w/o chloride (Cl^-)) during the initial 28 days exposure, 9.00 w/o NaCl (5.46 w/o Cl^-) for the next 28 days, and 15.00 w/o NaCl (9.10 w/o Cl^-) for the last 28 days. Corrosion rate of the different rebar specimens was determined by both weight loss and polarization resistance measurements.

The second test method, AST-2A, consisted of continuous immersion of specimens in simulated pore solution of the same composition as for AST-1. In this case, however, no chlorides were present initially but were subsequently introduced incrementally as NaCl at time intervals ranging from one to several days. Also, AST-2A specimens were anodically polarized potentiostatically to +0.100 V_{SCE}. For both AST-1 and AST-2A experiments, the test solution was periodically titrated for hydroxide (OH^-); and pH was then calculated using the equation,

$$pH = 14+\log (\gamma_{OH} \cdot [OH^-]) \tag{3.1}$$

where γ_{OH} is the activity coefficient for OH^-, which was taken as 0.7[16] and $[OH^-]$ is molality of that species. An example calculation is provided in Appendix A. The purpose of these experiments was to determine the critical Cl^- concentration for loss of passivity and onset of active corrosion.

The AST-2B experiments, on the other hand, involved anodic potentiodynamic polarization scans upon individual specimens in deaerated, saturated calcium hydroxide ($Ca(OH)_2$) with different chloride ion concentrations ($[Cl^-]$). The objective in this case was to determine the critical pitting potential for the different types of rebar. In effect, the AST-2B experiments are a sequel to the AST-2A, in that the former determined the potential for pitting at a given $[Cl^-]$ and the latter the critical $[Cl^-]$ at a specific potential (+0.100 V_{SCE} in this case).

Materials

Table 3.1 lists the various steels that were acquired based upon a review of the literature and bar availability. The fact that Type 316L stainless steel (SS) was acquired from two sources resulted because Type 304SS was requested from one of these, but chemical analysis of the received material indicated that it qualified as Type 316LSS instead. Composition for all bars is shown in table 3.2. Bar size in all cases was number 5 (16 mm diameter). The two types of clad bars (Stelax and SMI) were fabricated by two distinct processes, the former by packing a stainless

steel tube with steel scrap followed by rolling, and the latter by plasma applying stainless steel to a carbon steel billet and then rolling. Unless noted otherwise, bars were tested in the as-received surface condition subsequent to acetone cleaning.

Table 3.1. Listing of reinforcing steel types.

Designation./Spec.	Common Design.	As-Rec'd. Cond.	Microstructure	PREN[1]	Supplier
UNS-S31603	Type 316LSS	Pickled[2]	Austenitic	26[3]	Slater Steels Corporation
				24[4]	Dunkirk Specialty Steel
UNS-S31803	Type2205SS	As-Rolled	Duplex (Austinite plus Ferrite)	35	Gerdau AmeriSteel Corp.
ASTM A955-98	Type 2201LDXSS	As-Rolled	Lean Duplex (Austinite plus Ferrite)	25	Gerdau AmeriSteel Corp.
ASTM A615, Grade 75	MMFX-II	As-Rolled	Microcomposit austenite-martensite.	9	MMFX Corporation
-	Nouvinox	Pickled	316 Clad/Carbon Steel Core	-	Stelax Industries, Ltd.
-	SMI	Pickled	316 Clad/Carbon Steel Core	-	CMC Steel Group
UNS-S41003	Type 3Cr12SS	Pickled	Ferritic	12	American Utility Metals
ASTM A615	Black Bar	As-Rolled	Ferrite/Pearlite	0	Gerdau AmeriSteel Corp.

[1] PREN (Pitting Resistance Equivalent Number) where $PREN = \%Cr + 3.3 \cdot \%Mo + 16 \cdot \%N$.
[2] Pickled with HF and Nitric acid per ASTM A380.
[3] Subsequently designated as 316.16.
[4] Subsequently designated as 316.18.

Table 3.2. Chemical composition of the rebar types.

Alloy	C	Mn	P	S	Si	Cr	Ni	Mo	Cu	N	Fe
Type 316LSS(316.16)	0.03	1.55	0.025	0.001	0.59	18.43	10.06	2.08	0.42	0.068	Bal.
Type 316LSS(316.18)	0.03	1.66	0.026	0.005	0.42	16.97	10.07	2.15	0.85	0.065	Bal.
Type2205SS	0.029	1.68	0.028	0.004	0.63	21.58	4.8	2.64	-	0.15	Bal.
Type 2201LDXSS	0.04	4.70	0.019	0.001	0.80	22.47	1.68	0.24	0.38	0.117	Bal.
MMFX-II	0.05	0.45	0.012	0.015	0.23	9.30	0.10	0.03	0.12	-	Bal.
Type 3Cr12SS	0.04	0.38	0.018	0.024	0.71	11.69	0.50	0.09	0.02	-	Bal.
Black Bar	0.3	1.22	0.013	0.032	0.26	0.21	0.19	0.04	-	-	Bal.

AST-1: Wet-Dry Exposures

Specimens

Both straight and bent rebar specimens were tested in this phase of the program. The former were sectioned directly from the as-received rebars to a length of 152 mm. In the latter case (bent bar specimens), the rebar was bent 180^{o} to a radius that was four times the bar diameter. Specimens were acquired by then sectioning the bent portion of the rebar such that the circumferential length was approximately 200 mm. An electrical lead was mechanically attached to one end of each specimen via a screw and drilled and tapped hole. Specimens were then cleaned and the ends encapsulated with West System Brand marine epoxy type 105 and hardener type 207, a commercially available slow cure epoxy. Figures 3.1 and 3.2 show photographs of these two specimen types. In addition, MMFX-II™ and clad bars were prepared in surface abraded (A) and surface damaged (D) conditions. For clad bars, the intention in testing specimens with the A and D surface preparations was to evaluate possible effects of two degrees

Figure 3.1. Photo. Straight, as-received, Stelax bar with epoxy-mounted ends and electrical lead.

Figure 3.2. Photo. Three bent, as-received Type 2201 stainless steel bars with electrical leads.

of clad disruption on corrosion performance. The A condition did not penetrate the cladding, whereas the D condition did. Also, because MMFX-II™ is a relatively new alloy that involves proprietary thermo-mechanical processing, the possibility was considered that corrosion properties of the near surface might differ from the bulk. Abrasion (condition A) involved pressing the side surface of a rebar specimen for 30 seconds against a rotating round steel wire brush that was mounted in a drill press. This resulted in two, approximately two cm diameter abraded areas on each rebar specimen, as shown in figure 3.3. The D condition, on the other hand, involved drilling a 4.8 mm diameter hole to a depth of three mm on a bar side. Figure 3.4 shows a photograph of a specimen prepared in this manner. Type 2201 stainless steel specimens were tested as-rolled (unpickled) and in addition with surface blasting using (1) steel shot, (2) stainless steel shot, and (3) silica sand.

Test Procedure

Figure 3.5 shows a photograph of this test system, which consisted of two polyethylene chambers, an elevated one in which rebar specimens were suspended and a lower one which served as a reservoir for the solution during the nonsubmerged period of each cycle. A timer and solenoid valve controlled the solution exchange between chambers. Figure 3.6 is a photograph of specimens under test. The exposure chamber was covered such that a high relative humidity was maintained during the dry period in order to maximize test severity during this

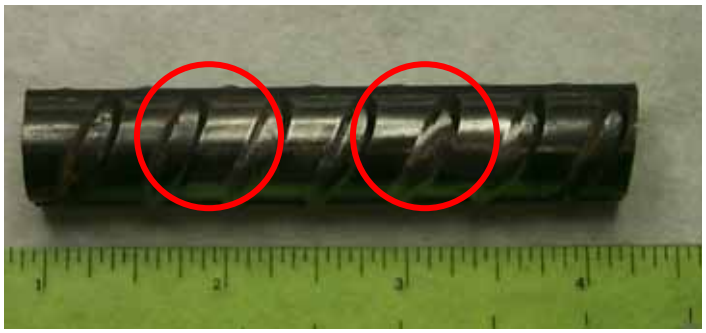

Figure 3.3. Photo. Abraded MMFX-II™ specimen.

Figure 3.4. Photo. Damaged MMFX-II™ specimen.

Figure 3.5. Photo. AST-1 wet-dry exposure setup.

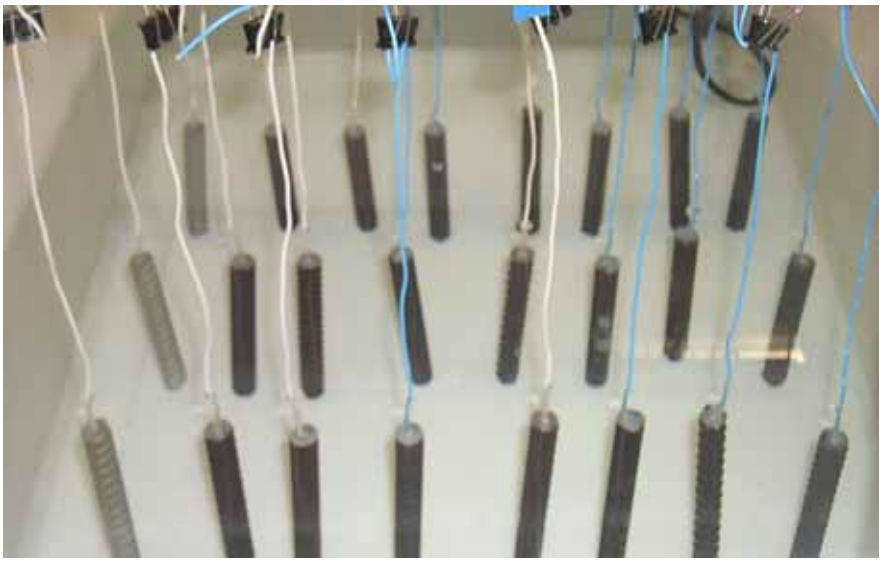

Figure 3.6. Photo. AST-1 specimens under test in the upper hold tank (figure 3.5).

phase. Triplicate specimens of a given material and specimen type were tested in a particular run. Polarization resistance (PR) measurements were made periodically on the rebar specimens during the submerged phase of the exposures using a Gamry CMS100 potentiostat with a scan rate of 0.33 mV/sec and polarizations of ±0.020 V referenced to the free corrosion potential. Prior to scanning, rebar potential was monitored for 300 seconds or until any potential variations were less than 0.1 mV/sec. From the measured PR, corrosion rate, CR, was calculated using a modified form of the Stern-Geary equation,

$$CR = 3.15 \cdot 10^{7} \cdot \frac{Z}{n \cdot F \cdot \rho} \cdot \frac{B}{PR}, \tag{3.2}$$

where Z is atomic weight, n is the number of electrical equivalents, F is Faraday's constant, ρ is alloy density, and B is a constant that depends on the Tafel constants. In the present determinations, B was taken as 0.052 V for the metals that were assumed to be corroding passively (316, 2205, 2201, and 3Cr12) and 0.026 V for the actively corroding ones (MMFX-II™ and black bar). An example calculation is provided in Appendix B.

In addition, one rebar specimen of each material was removed at the completion of each 28-day period for weight loss determination. The average CR over the exposure duration was determined from before and after specimen weight measurements using the expression,

$$CR = \frac{W}{\rho \cdot A \cdot T}, \tag{3.3}$$

where W is weigh loss, ρ is metal density, A is exposed rebar specimen surface area, and T is exposure time. An example calculation is provided in Appendix C. Overall, there were five separate AST-1 runs with the rebar and specimen type for each being as listed in table 3.3. This indicates that a total of 267 specimens were tested, with anywhere from 24 to 69 specimens being exposed in a particular run. Multiple runs on the same rebar type were performed to confirm run-to-run PR and corrosion rate reproducibility. Also, for a given run there were

triplicate specimens of the alloys tested. The lack of a pattern with regard to what rebars were exposed in a particular run was due, in part, to delays in acquiring some of the materials.

Table 3.3. Listing of AST-1 runs and the rebar and specimen type for each ("x" indicates that the indicated alloy was tested during that run, and "2" indicates two sets of triplicate specimens).

	AST-1 Run Number									
	1	2		3		4		5		6
Material	S	S	B	S	B	S	B	S	B	S
Black Bar	x	x	x	x	x	x	x		-	-
MMFX-II	x	x	x	x	x	-	-	x	-	-
MMFX-II(A)	x	x	x	x	x	-	-	x	-	-
MMFX-II(D)	x	x	x	x	x	-	-	x	-	-
3Cr12	-	-	-	-	-	x(2)	x(2)	x	-	-
Type2201	x	x	x	x	x	x	x	x	-	-
Type 2205	x	x	x	x	x	x	x	x	-	-
Type 2201P	x	x	-	x	-	x	-	x	-	-
Type 2201(Fe Blast)	-	-	-	-	-	x	-	x	-	-
Type 2201(SS Blast)	-	-	-	-	-	x	-	x	-	-
Type 2201(Sand Blast)	-	-	-	-	-	x	-	x	-	-
Type 316.16	-	-	-	-	-	x(2)	x(2)	x	-	-
Type 316.18	x	x	x	x	x	x	x	-	-	-
Clad/Nouvinox	-	x	x	x	x	x	-	x	-	x
Clad/Nouvinox(A)	-	x	-	x	-	x	-	-	-	x
Clad/Nouvinox(D)	-	x	-	x	-	x	-	-	-	x
Clad /SMI	-	-	-	-	-	-	-	x	-	x
Clad/SMI(A)	-	-	-	-	-	-	-	x	-	x
Clad/SMI(D)	-	-	-	-	-	-	-	x	-	x

AST-2A: Chloride Threshold Determinations

The specimen type in this case was the same straight 152 mm long number 5 rebar employed in AST-1. The test procedure involved concurrent exposure of 20 rebar specimens which were potentiostatically polarized using a single, locally designed and constructed potentiostat. Current to each rebar specimen was calculated from the voltage drop across an individual 10-ohm resistor that was in series with each specimen. Chloride as NaCl was incrementally added to the simulated pore solution at time intervals of from one to several days. Figure 3.7 shows a schematic representation of this test system, and figure 3.8 provides a photograph. Figure 3.9 is a photograph of specimens under test. The rationale behind this approach considers that the polarized potential (+0.100 V_{SCE}) is about 100 mV more positive than the upper value of the free corrosion (half-cell) potential that is likely to occur for rebar in concrete under outdoor atmospheric or splash zone exposure. As such, the critical chloride concentration (threshold) to cause loss of rebar passivity and onset of active corrosion, $\left[Cl^-_{th}\right]$, should be less at this potential (+0.100 V_{SCE}) than in actual service, thereby providing a conservative determination of this parameter. A current density of 10 $\mu A/cm^2$ was defined as indicative of corrosion initiation; and

the corresponding [Cl^-] was taken as $\left[Cl^-_{th}\right]$. While this current density is somewhat arbitrary, it is the same as has been employed by others in similar experiments.[17] The chloride threshold concentration is an important parameter for projection of time-to-corrosion, maintenance planning, and life-cycle cost analysis for reinforced concrete structures.

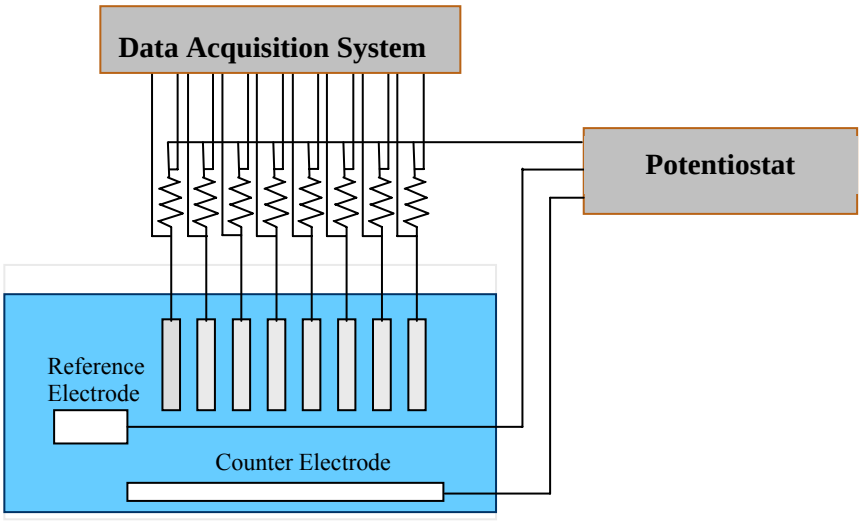

Figure 3.7. Schematic illustration. AST-2A experimentation.

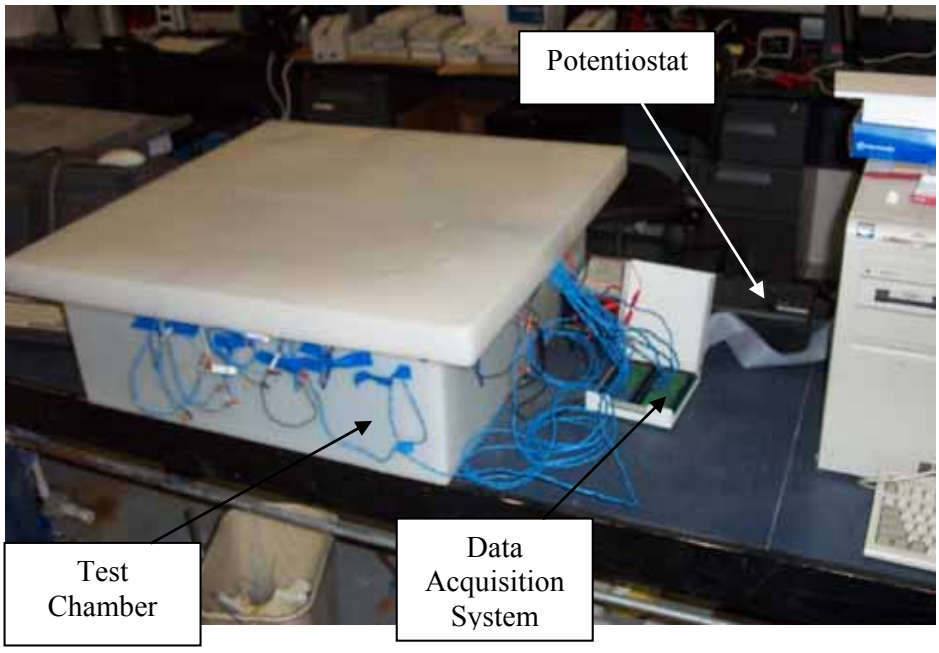

Figure 3.8. Photo. AST-2A test system.

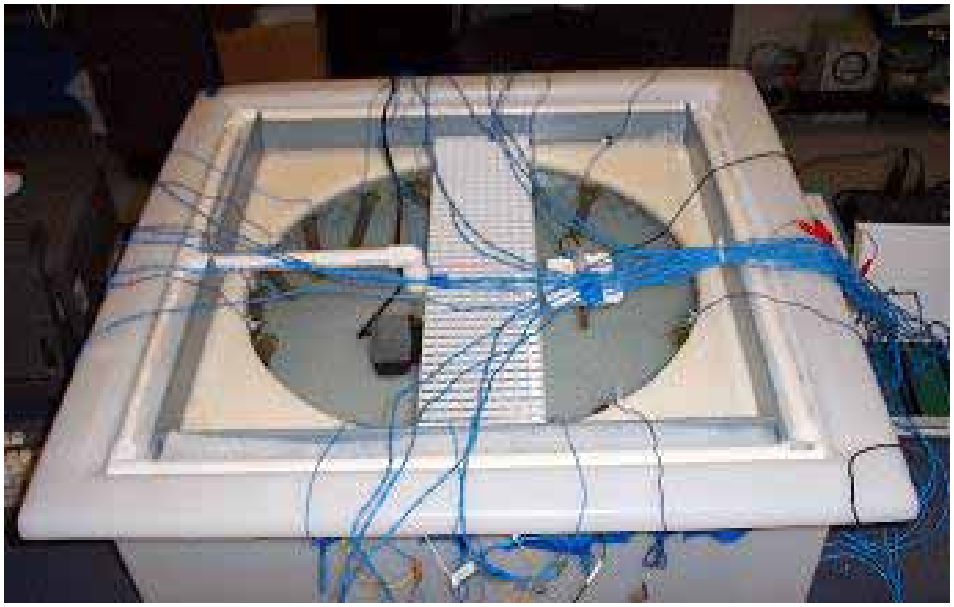

Figure 3.9. Photo. Test chamber with specimens.

An initial, trial AST-2A run employed either one or two rebar specimens for six of the alloys. Subsequent runs employed 10 identical specimens of two rebar types. Table 3.4 provides a listing of these for the three runs that have been completed (total of 52 specimens). The relatively large number of specimens of each alloy in the latter two runs serves as a basis for statistical treatment of the resulting $\left[Cl^-_{th}\right]$ data. Thus, considering that $\left[Cl^-_{th}\right]$ is a statistically distributed parameter and that the results from this study can be related to actual service in concrete, then it should be possible to project the percentage of rebar for which corrosion initiates at a given [Cl^-]. This is directly related to practice in the sense that repairs and rehabilitations are often initiated in response to a certain percentage of substructure spalling or deck delamination.

Table 3.4. Listing of each AST-2A run according to rebar type and number of specimens.

			Number of Specimens						
AST-2A Run Number	BB	3Cr12	MMFX-II™	MMFX-II™ (A)	MMFX-II™ (D)	2201	2205	316.16	316.18
1	1	1	2	2	2	1	1	1	1
2	-	-	10	-	-	10	-	-	-
3	10	10	-	-	-	-	-	-	-

AST-2B: Pitting Potential Determinations

Specimens

Three types of specimens, defined according to orientation and preparation of the exposed surface, were tested in order to determine the respective pitting potentials. These included (1) longitudinally oriented rebar specimens that were similar to the AST-1 and AST-2A ones except that length was 30 mm with (a) the as-received surface condition and (b) a machined and 600 grit polished surface condition and (2) sectioned rebar specimens where the cross-section (machined

and 600 grit polished) was exposed. The objective of employing multiple specimen orientations and surface conditions was to determine any effect these might have upon corrosion properties. Figures 3.10 through 3.13 show schematic illustrations and photographs of these three specimen types. Four rebar types, 316.16, 2201, MMFX-II™, and 3Cr12, were tested using this protocol.

Test Procedure

These experiments utilized a one liter glass container with a threaded Teflon-lined lid. Five holes were drilled in the lid for insertion of electrical leads and tubing for nitrogen gas purging. Each of the leads and the tubing were mounted in a sealed rubber stopper which was fitted into the lid. The immersion solution for the rebar specimens was saturated $Ca(OH)_2$ containing 0 to 10 w/o NaCl (0-6.07 w/o Cl^-). The rebar specimen potential normally stabilized after about 20 minutes of high purity nitrogen gas purging of the solution. Purging continued throughout the experiments. Figure 3.14 provides a photograph of the test cell. The same Gamry system as for the AST-1 experiments (see above) was employed to perform the scans. These were initiated at a potential of −0.600 V_{SCE} in order to reduce surface oxides and reduce any effect of these on electrochemical response. The scans proceeded positively to +1.000 V_{SCE} or 2.00 mA/cm^2, whichever occurred first. This assured that a relatively broad potential range was covered. The scan was then reversed and terminated at −0.500 V_{SCE}. The forward and reverse scan rates were both 0.50 mV/s, but a limited number of experiments were performed at 0.33 and 1.00 mV/s. A minimum of three replicate experiments was performed for each set of variables with each scan using a newly prepared specimen. Table 3.5 lists the number of tests for each rebar and specimen type and surface condition. A total of 116 scans were performed.

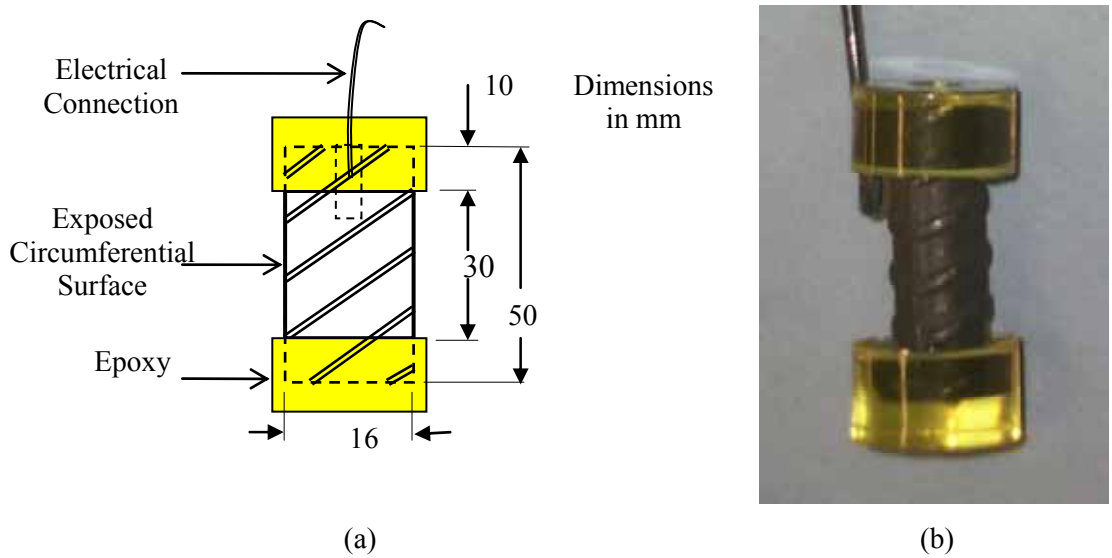

Figure 3.10. Illustration and photo. Schematic illustration (a) and photograph (b) of the as-received, circumferential AST-2B test specimen.

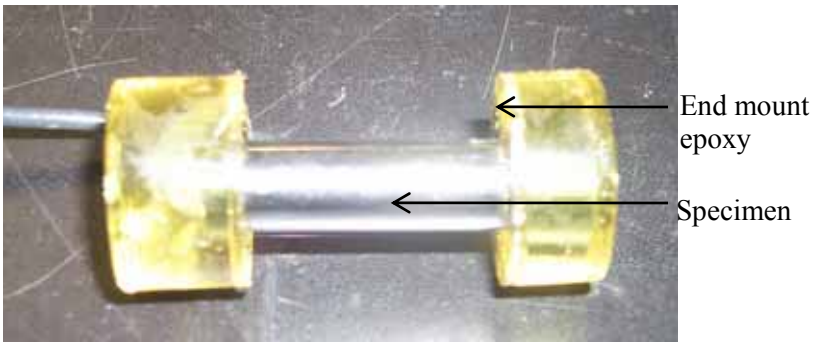

Figure 3.11. Photo. Polished circumferential specimen.

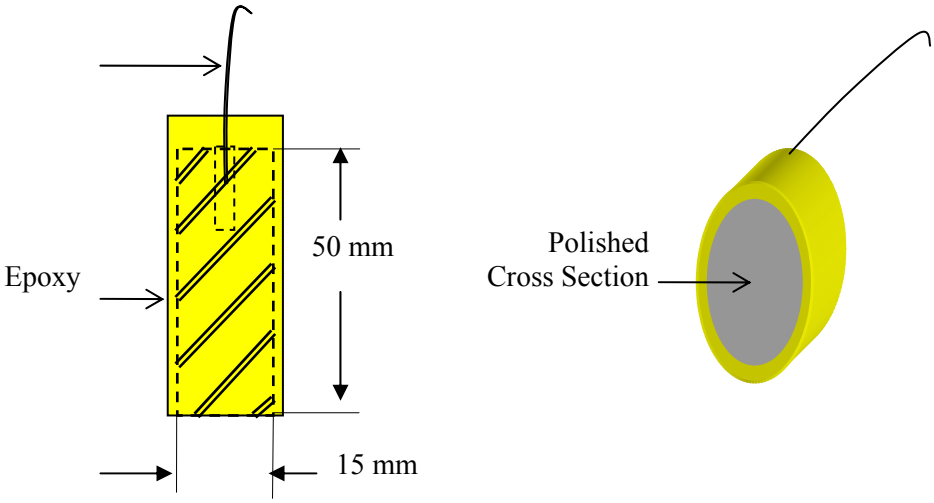

Figure 3.12. Schematic illustration. Polished cross section surface specimen.

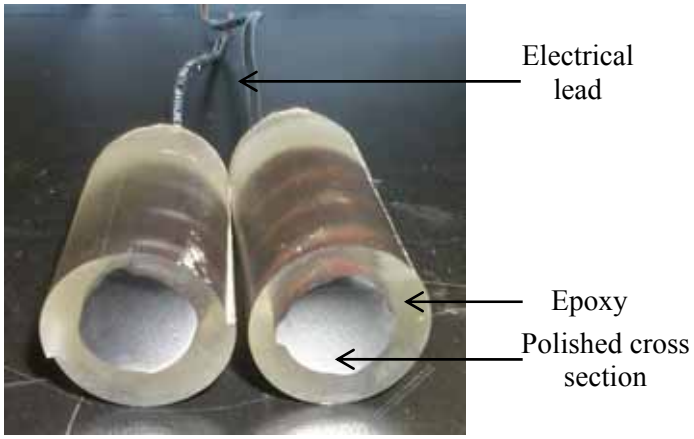

Figure 3.13. Photo. Two polished cross section specimens.

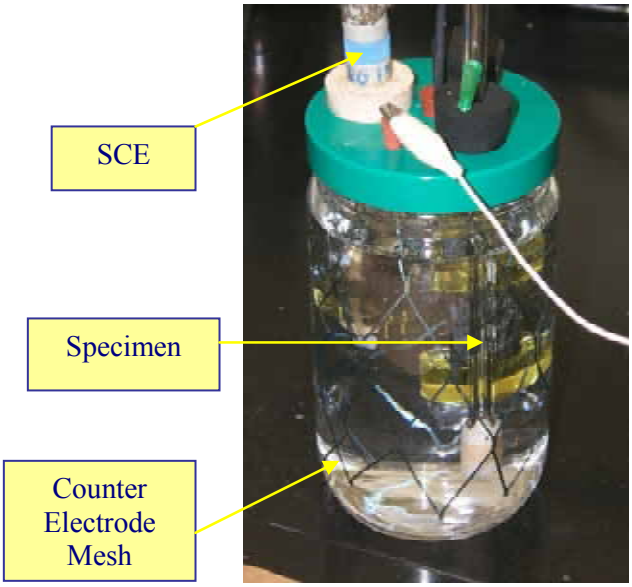

Figure 3.14. Photo. Test cell for potentiodynamic polarization measurements.

Table 3.5. Listing of the number of AST-2B tests for each specimen type and surface condition.

Rebar Type	Specimen Type/Surface Condition	Scan Rate, mV/sec.	Number of Specimens Concentration, w/o NaCl					
			0.05	0.50	1.00	2.00	5.00	10.00
MMFX-II™	Cross Section/Polished	0.50	-	3	-	-	-	-
	Circumferential/Polished	0.50	-	3	-	-	-	-
	Circumferential/As-Received	0.33	-	3	-	-	-	-
		0.50	3	3	3	4	3	4
		1.00	-	3	-	-	-	-
3Cr12	Circumferential/As-Received	0.50	3	3	6	4	3	4
2201	Circumferential/As-Received	0.50	3	4	4	3	4	3
	Circumferential/Pickled	0.50	3	4	3	3	3	5
316.16	Circumferential/As-Received	0.50	3	3	3	3	4	3

LONG-TERM TESTS

Specimen Design

General

Four different types of reinforced concrete specimens, designated (1) simulated deck slabs (SDS), (2) two different types of three bar column specimens (designations S3BC and 3BTC),[1] (3) macro-cell slabs (MS), and (4) field columns (FC), were fabricated by the Florida

[1] The S3BC designation signifies a square column specimen with three rebars, and 3BTC indicates a tombstone column (rectangular cross section) specimen with three rebars. Each is described subsequently in detail.

Department of Transportation State Materials Office (FDOT-SMO) in Gainesville. Three concrete mix designs, designated (1) STD1 (5 bags cement and 0.5 w/c) which yields a high permeability concrete, (2) STD2 (7 bags of cement and 0.41 w/c) which results in moderate permeability, and (3) STD3 (7 bags of cement and 0.50 w/c) which is of intermediate permeability, were employed. Target mix designs are listed in table 3.6. The various corrosion resistant alloy types in addition to black bar (table 3.1) were used as reinforcement. Table 3.7 provides a listing of the different specimen types and bar configurations that were prepared, each of which is discussed in detail below. The clad bars were placed in the as-received condition with and without intentional damage (3 mm diameter clad penetrations spaced 25 mm apart). Specimens were cured subsequent to casting and prior to exposure for a minimum of 6 months in a warehouse with no temperature or humidity control. All bars were nominally 16 mm in diameter (number 5) and, unless noted otherwise, had the as-received surface finish (table 3.1).

Table 3.6. Concrete mix designs.

Material	STD1	STD2	STD3
Cement (Bags)	5	7	7
Cement, kg	213	300	300
Water, kg	107	122	149
Water/Cement	0.5	0.41	0.5
Fine Aggregate (silica sand), kg	652	540	489
Coarse Aggregate (limestone), kg	753	753	747

Simulated Deck Slabs

The simulated deck slab (SDS) specimens were fabricated with six bars; three of which comprised a top mat and three the bottom mat, as illustrated schematically in figure 3.15. Concrete cover for all bars was 25 mm; and triplicate specimens were prepared for each bar type and specimen variable, as described below. Concrete mix designs STD1 and STD2 were employed but with most specimens being prepared using the former. Because of material inventory limitations, no Stelax bars with intentional clad damage were included in this phase of the study. Five different modifications to the above standard slab configuration have been prepared to date and are under test, as listed and described below.

1. Slabs with black bottom bars (designated BCAT). For these, the bottom mat was comprised of black bars whereas the top bars were one of the corrosion resistant alloys.
2. Slabs with a simulated concrete crack (designated CCON). In fabrication of these specimens, a 1.6 mm thick stainless steel shim was placed vertically in the form on top of and perpendicular to the upper bars at their center. The shim was removed subsequent to the initial concrete set.
3. Slabs with bar crevice (splice) (designated CREV). In this case, two bars that overlapped for a portion of their length replaced each of the three single top bars in the standard specimen. Hence, the top mat of reinforcement consisted of six rebars instead of three, as was the case for the other slab types. Cover for each of the bar pairs was maintained at 25 mm. Figure 3.16 illustrates this specimen type schematically.
4. Slabs with a bar crevice (splice) per configuration (3) but with a simulated concrete crack also (designated CCRV).
5. Slabs with a simulated concrete crack and black bar cathode (designated CCNB).

Table 3.7. Listing of the various specimen types, variables, and nomenclature for each.

Specimen Designation	Description	Specimen Type*
STD1	STD1 concrete mix.	SDS, S3BC, FC
STD2	STD2 concrete mix.	SDS, S3BC, 3BTC
STD3	STD3 concrete mix.	3BTC
BCAT	STD1 concrete, bottom mat black steel.	SDS, MS
CCON	STD1 concrete mix, simulated concrete crack.	SDS, MS
CCNB	STD1 concrete mix, bottom mat (cathode) black bars, simulated concrete crack.	SDS, MS
CREV	STD1 concrete mix, top bar crevice.	SDS
CCRV	STD1 concrete mix, simulated concrete crack, top bar crevice.	SDS
BENT	STD1 concrete mix, top bar bent	S3BC, MS
	STD3 concrete mix, top bar bent	3BTC
BNTB	STD1 concrete mix, top bar bent, bottom bars black steel.	MS
CBNT	STD1 concrete mix, simulated concrete crack, top bar bent.	MS
CBNB	STD1 concrete mix, simulated concrete crack, bottom bars black steel, top bar bent.	MS
ELEV	STD1 concrete mix, one bar elevated.	S3BC
	STD3 concrete mix, one bar elevated.	3BTC
WB	STD1 concrete mix, top bars wire brushed.	SDS
ARWB	STD1 concrete mix, top bars as received.	MS
USDB	STD1 concrete mix, 3 mm diameter clad holes 25 mm apart on top bars.	MS
UBDB	STD1 concrete mix, 3 mm diameter clad holes 25 mm apart on top bars, top bar bent.	MS
CSDB	STD1 concrete mix, simulated concrete crack, 3 mm diameter clad holes 25 mm apart.	SDS, MS
CBDB	STD1 concrete, cracked concrete, 3 mm diameter clad holes 25 mm apart on top bars, top bar bent.	MS
BCCD	STD1 concrete mix, 3 mm diameter clad holes 25 mm apart on top bars, bottom bars black steel.	SDS. MS
ACID	STD1 concrete mix, top bars lab pickled, cathode as received.	SDS

* SDS: Simulated deck slab.
S3BC: Square 3-bar column.
3BTC: 3-bar tombstone column.
MS: Macroslab
FC: Field column.

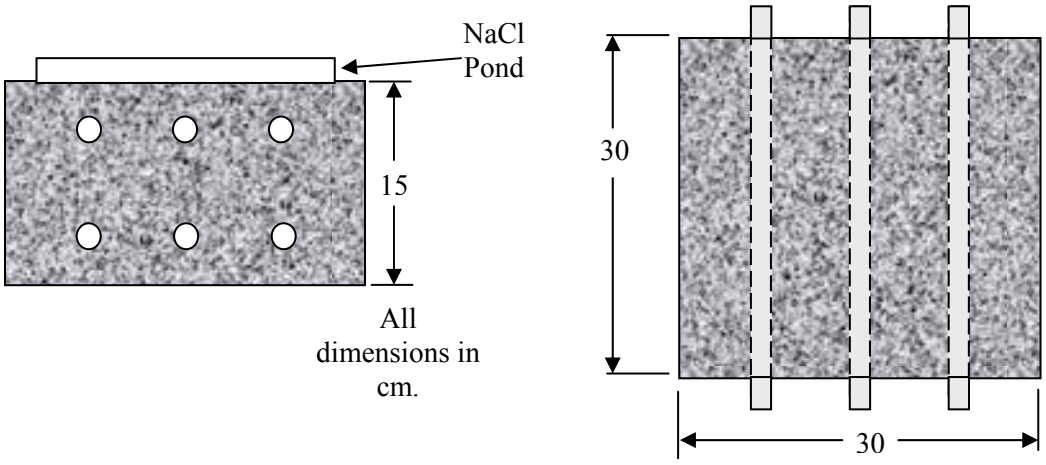

Figure 3.15. Schematic illustration. Standard simulated deck slab specimens.

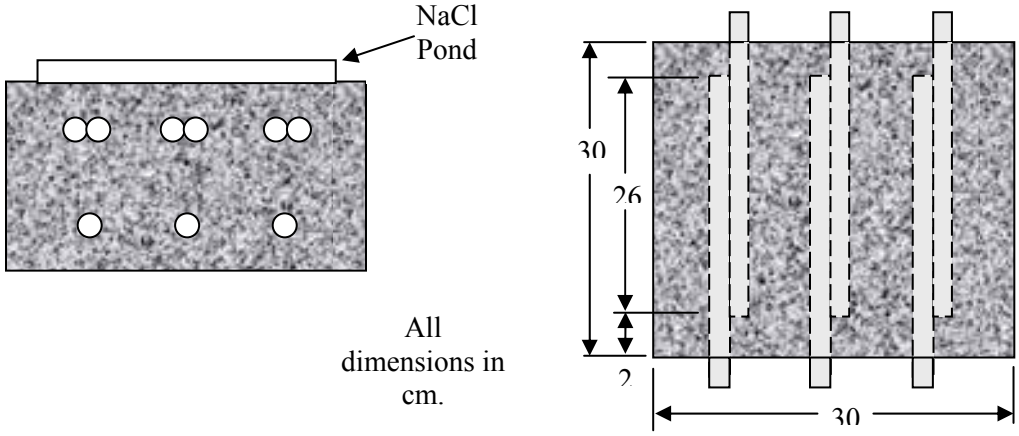

Figure 3.16. Schematic illustration. CREV type simulated deck slab specimens.

Because the specimens were fabricated over a period of time, they were delivered to FAU on three separate occasions. The following example illustrates the nomenclature that was adapted to identify a standard specimen:

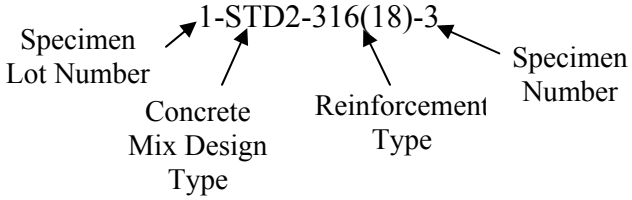

Figure 3.17. Graphic. Standard specimen nomenclature.

There were three Specimen Lot Numbers corresponding to one of the three groups of specimens that were delivered to FAU by FDOT at different times. Likewise, designation of specimens that were nonstandard (BCAT, CCON, …) is illustrated by the following example:

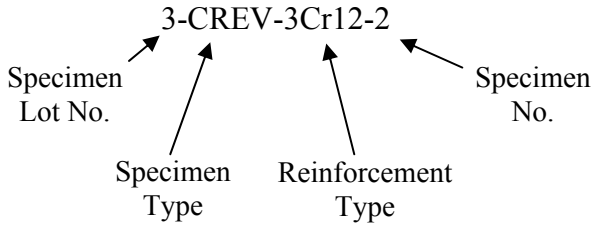

Figure 3.18. Graphic. Nonstandard specimen nomenclature.

Thus, the latter identifies this as simulated deck slab specimen number 2 with 3Cr12 reinforcement in the crevice configuration from lot 3. The default mix design (no indication) was STD1.

Once slabs were delivered to FAU, their condition between the different lots was normalized by placement in air conditioned space for 2 months. During this time, a hard electrical connection was established between bars in each of the two mats of each slab using a stainless steel wire in conjunction with a screw and drilled and tapped hole in each bar end. The wires from each mat were normally connected; but the circuit was periodically interrupted during the exposures and a 10 Ω resistor temporarily inserted. This allowed measurement of the voltage drop between the mats from which macro-cell current was calculated. This current was then divided by the surface area of the three top bars to obtain current density. The specimen sides were epoxy coated, and a plastic bath with a vented lid was attached to the top concrete surface in preparation for ponding with a salt water solution. Exposure for the three sets of specimens commenced on June 9, August 5, and October 30, 2003, respectively. Salt water ponding consisted of a 1-week wet—1-week dry cycle with 15 w/o NaCl (9.10 w/o Cl^-). Figure 3.17 shows a single specimen under test, and figure 3.18 is a perspective view of the test site.

Three Bar Columns

Two different versions of this type specimen, the square 3-bar column (S3BC) and the 3-bar tombstone column (3BTC), were prepared. Each of these has three bar geometries: normal, bent, and elevated. The two configurations (S3BC and 3BTC) are illustrated schematically in figures 3.19 and 3.20, respectively, where the S3BC specimens were fabricated using concrete mixes STD1 and STD2 and the 3BTC using STD2 and STD3 (table 3.6). Initially, the square geometry only (S3BC) was to be employed; but subsequent to these being prepared, the 3BTC was developed, considering the fact that chlorides can reach the reinforcement from three sides rather than one which provides a more severe exposure. The normal reinforcement configuration has been employed by the FDOT for more than 10 years and was intended to provide baseline data that can be compared to results from previous studies. On the other hand, the bend bar configuration was considered particularly relevant in the case of the stainless clad and possibly the MMFX-II™ reinforcements. The elevated bar geometries were intended to provide different anode-cathode area ratio of bars and, possibly, enhance macro-cell activity. Six specimens of each rebar type were prepared and exposed for each test condition. Subsequent to curing, these were partially submerged in a 3.5 w/o NaCl solution to a depth of 152 mm for the purpose of facilitating formation of an electrochemical macro-cell on each of the long bars. Figure 3.21 shows the outside screen room at the FDOT-SMO facility (north central Florida) where the specimens are exposed.

Figure 3.19. Photo. Ponded deck slab specimen under test.

Figure 3.20. Photo. Perspective view of exposure site and specimens.

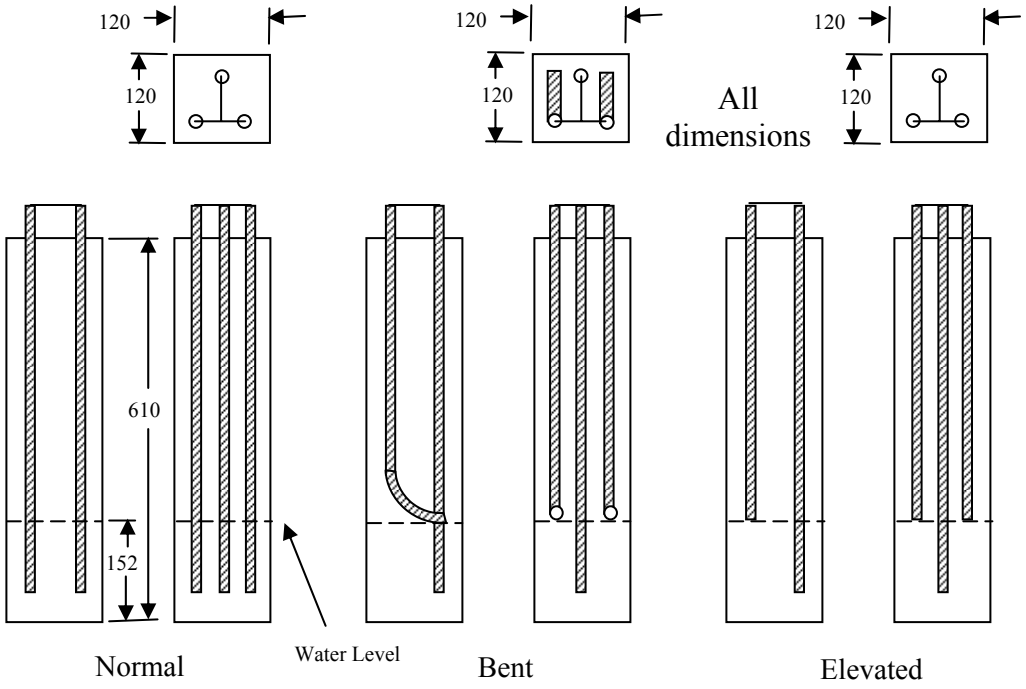

Figure 3.21. Schematic illustration. Square three bar column specimen for each of the three bar configurations.

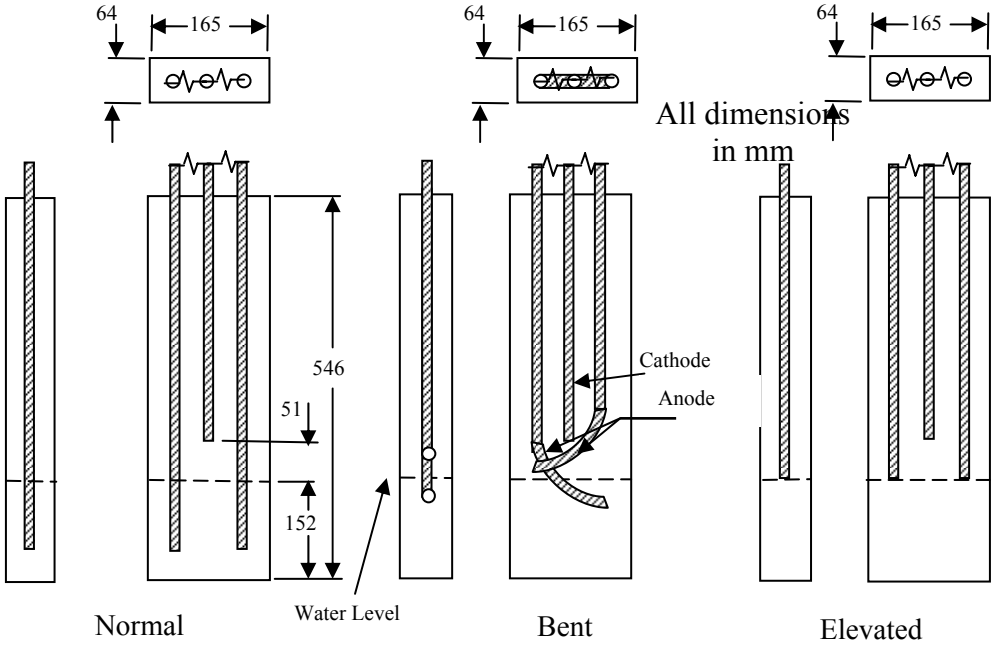

Figure 3.22. Schematic illustration. Tombstone type three bar column specimen for each of the three bar configurations.

Figure 3.23. Photo. Three bar column specimens under exposure.

Once exposure was initiated, the individual bar potentials in each of the two specimen types (S3BC and 3BTC) were measured monthly. In addition, for the 3-bar tombstone columns (3BTC) macro-cell current between the two long bars (anode) in each specimen and the short bar (cathode) was measured. The potential of all three bars coupled together was also measured. These readings were acquired daily using a custom designed data acquisition system. Specimen exposure was terminated upon concrete cracking or visible corrosion product bleed-out.

Macro-Cell Slab Specimens

Specimens of this type were fabricated with the reinforcement having been wire brushed, although one set was prepared using the bars as-received. Two bar configurations, straight and bent, were employed, as illustrated by figure 3.22. The macro-cell slab STD1 specimens were made with and without a simulated crack, but specimens based upon the STD2 concrete mix were standard (no crack). Subsequent to curing, the specimens were inverted; and a 76 x 152 mm pond was attached to what had been the bottom cast face. Specimens were exposed to 14 days wet—14 days dry cyclic ponding with 3.0 w/o NaCl solution until corrosion induced cracking occurred. Figure 3.23 shows the exposure arrangement, which was similar to the one for the 3-bar columns. As was done for the 3-bar columns, macro-cell current between the top single bar (anode) and lower four electrically connected bars (cathode) was recorded daily via a data acquisition system, whereas potential measurements were only made manually on a monthly basis.

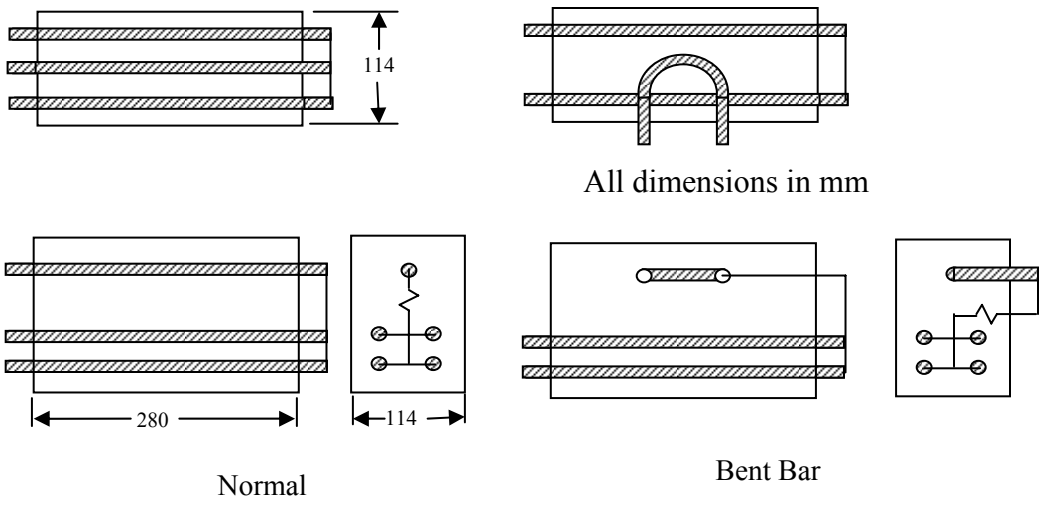

Figure 3.24. Schematic illustration. Geometry of the macro-cell slab type specimen with both bent and straight bars.

Figure 3.25. Photo. Macro-cell slab specimens under exposure.

Field Columns

These specimens were made using the STD1 concrete mix design only and with all bars in the as-received condition. Figure 3.24 is a schematic drawing that illustrates the specimen geometry. Each bar is electrically isolated from the others. The columns have been exposed in the inter-coastal waterway at Crescent Beach, FL by burying the bottom 1.2 m in bottom soil such that mean high water is 1.8 m from the specimen bottom; however, placement was delayed because of environmental permitting issues and only commenced in September 2005. Figure 3.25 is a photograph of the specimens and exposure site. Polarization resistance and potential of each individual bar was measured at the time of initial exposure. These measurements are to be obtained every 6 months until corrosion cracking or visible corrosion product bleed out is observed.

Tables 3.8 through 3.13 list the number of specimens for each specimen configuration and type of reinforcement (316.18 and 3Cr12, 2201, MMFX-II™, Stelax, SMI, and black bar).

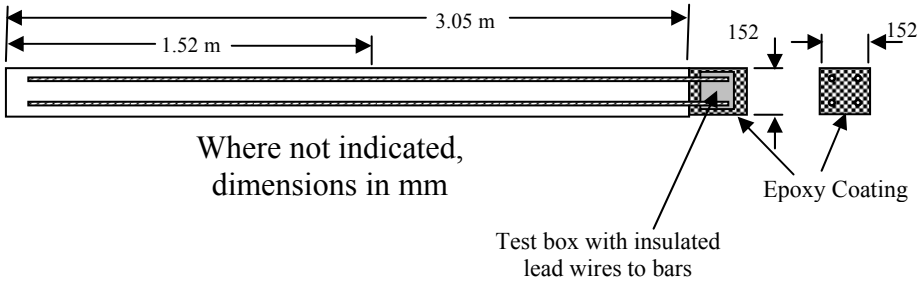

Figure 3.26. Schematic illustration. Geometry of the field column type specimen.

Figure 3.27. Photo. Field column specimens under exposure at the Intracoastal Waterway site in Crescent Beach, FL.

Table 3.8. Listing of specimens reinforced with 316.18 and 3Cr12.

Description	SDS	S3BC	3BTC	MS	FC
STD1 mix design, standard specimen.	3	6	-	6	3
STD3 mix design, standard specimen.	3	3	3	3	-
STD2 mix design, standard specimen.	-	-	6	-	-
STD1-BCAT.	3	-	-	3	-
STD1-CCON.	3	-	-	3	-
STD1-CCNB.	3	-	-	3	-
STD1-CREV.	3	-	-	-	-
STD1-CCRV.	3	-	-	-	-
STD1-BENT.	-	3	-	3	-
STD3-BENT.	-	-	3	-	-
STD1-BNTB.	-	-	-	3	-
STD1-CBNT.	-	-	-	3	-
STD1-CBNB.	-	-	-	3	-
STD1-ELEV.	-	3	-	-	-
STD3-ELEV.	-	-	3	-	-
STD1-WB.	3	-	-	-	-
STD1-ARWB.	-	-	-	3	-
Total	24	15	15	33	3
				TOTAL	90

Table 3.9. Listing of specimens with 2201 rebar (specimens in shaded cells not yet fabricated).

Description	SDS	S3BC	3BTC	MS	FC
STD1 mix design, standard specimen.	3	6	-	6	3
STD3 mix design, standard specimen.	3	3	3	3	-
STD2 mix design, standard specimen.	-	-	6	-	-
STD1-BCAT.	3	-	-	3	-
STD1-CCON.	3	-	-	3	-
STD1-CCNB.	3	-	-	3	-
STD1-CREV.	3	-	-	-	-
STD1-CCRV.	3	-	-	-	-
STD1-BENT.	-	3	3	3	-
STD3-BENT.	-	-	3	-	-
STD1-BNTB.	-	-	-	3	-
STD1-CBNT.	-	-	-	3	-
STD1-CBNB.	-	-	-	3	-
STD1-ELEV.	-	3	3	-	-
STD3-ELEV.	-	-	3	-	-
STD1-WB.	3	-	-	-	-
STD1-ARWB.	-	-	-	3	-
STD1-ACID.	3	-	-	-	
STD1-ABRD	3				
	30	15	15	33	3
				TOTAL	96

Table 3.10. Listing of specimens reinforced with MMFX-II™.

Description	SDS	S3BC	3BTC	MS	FC
STD1 mix design, standard specimen.	3	6	-	6	3
STD2 mix design, standard specimen.	3	3	3	3	-
STD3 mix design, standard specimen.	-	-	6	-	-
STD1-BCAT.	3	-	-	3	-
STD1-CCON.	3	-	-	3	-
STD1-CCNB.	3	-	-	3	-
STD1-CREV.	3	-	-	-	-
STD1-CCRV.	3	-	-	-	-
STD1-BENT.	-	3	-	3	-
STD3-BENT .	-	-	3	-	-
STD1-BNTB.	-	-	-	3	-
STD1-CBNT.	-	-	-	3	-
STD1-CBNB.	-	-	-	3	-
STD1-ELEV.	-	3	-	-	-
STD3-ELEV.	-	-	3	-	-
STD1-WB.	3	-	-	-	-
STD1-ARWB.	-	-	-	3	-
STD1-USDB.	3	-	-	3	-
STD1-ACID.	3	-	-	-	-
STD1-ABRD.	3	-	-	-	-
	33	15	15	36	3
				TOTAL:	102

Table 3.11. Listing of specimens reinforced with Stelax (specimens in shaded cells not yet fabricated).

Description	SDS	S3BC	3BTC	MS	FC
STD1 mix design, standard specimen.	3	6	-	6	3
STD2 mix design, standard specimen.	3	3	3	3	-
STD3 mix design, standard specimen.	-	-	6	-	-
STD1-CCON.	3	-	-	3	-
STD1-CREV.	3	-	-	-	-
STD1-CCRV.	3	-	-	-	-
STD1-BENT.	-	3	3	3	-
STD3-BENT .	-	-	3	-	-
STD1-CBNT.	-	-	-	3	-
STD1-ELEV.	-	3	3	-	-
STD3-ELEV.	-	-	3	-	-
STD1-WB.	3	-	-	-	-
STD1-ARWB.	-	-	-	3	-
STD1-USDB.	3	-	-	3	-
STD1-UBDB.	-	-	-	3	-
STD1-CSDB.	3	-	-	3	-
STD1-CBDB.	-	-	-	3	-
STD1-BCCD.	3	-	-	3	-
STD1-ACID.	3	-	-	-	-
STD1-ABRD.	3	-	-	-	-
STD1-CVNC .	3	-	-	-	-
	36	15	15	36	3
				TOTAL:	105

Table 3.12. Listing of specimens reinforced with SMI (specimens in shaded cells not yet fabricated).

Description	SDS	S3BC	3BTC	MS	FC
STD1 mix design, standard specimen.	3	-	-	6	3
STD2 mix design, standard specimen.	3	-	3	3	-
STD3 mix design, standard specimen.	-	-	6	-	-
STD1-CCON.	3	-	-	3	-
STD1-CREV.	3	-	-	-	-
STD1-CCRV.	3	-	-	-	-
STD1-BENT.	-	-	-	3	-
STD3-BENT .	-	-	3	-	-
STD1-CBNT.	-	-	-	3	-
STD1-ELEV.	-	-	-	-	-
STD3-ELEV.	-	-	3	-	-
STD1-WB.	3	-	-	-	-
STD1-ARWB.	-	-	-	3	-
STD1-USDB.	3	-	-	3	-
STD1-UBDB.	-	-	-	3	-
STD1-CSDB.	3	-	-	3	-
STD1-CBDB.	-	-	-	3	-
STD1-BCCD.	3	-	-	3	-
STD1-ABRD.	3	-	-	-	-
STD1-CVNC .	3	-	-	-	-
	33	0	15	36	3
				TOTAL:	87

Table 3.13. Listing of specimens reinforced with black bar.

Description	SDS	S3BC	3BTC	MS	FC
STD1 mix design, standard specimen.	3	6	-	9	3
STD2 mix design, standard specimen.	3	6	6	3	-
STD3 mix design, standard specimen.	-	-	6	-	-
CCON - STD1, Cracked concrete.	3	-	-	3	-
	9	12	12	15	3
				TOTAL:	51

4. EXPERIMENTAL RESULTS AND DISCUSSION

SIMULATED PORE WATER PH DATA FOR AST-1 AND AST-2

Figure 4.1 plots simulated pore water pH versus time for representative AST-1 and AST-2A experiments. Both sets of data approximately superimpose and show a progressive pH decrease with time from an initial value of 13.28 (AST-1) to a final of 13.12. This reflects a contribution of the common ion effect from addition of chlorides and possibly carbonation, the former being evidenced by the step decrease in pH of the AST-1 solution pH at 28 and 56 days (times at which $[Cl^-]$ was increased). This pH decrease is not a significant concern for interpretation of the AST-1 data, but it is important for projection of $\left[Cl^-_{th}\right]$, since this parameter is a function of Cl^- to OH^- ratio.

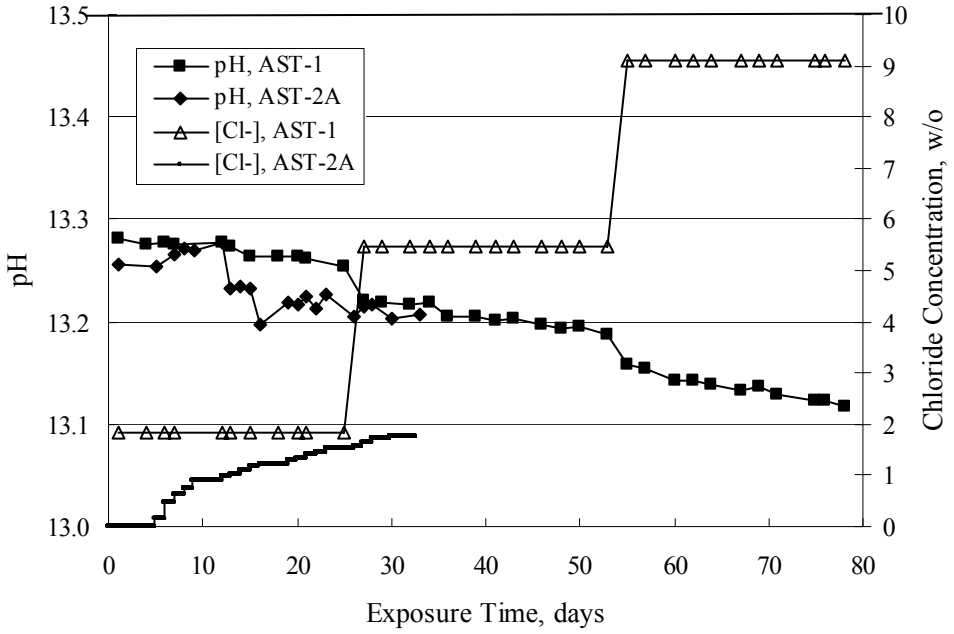

Figure 4.1. Graph. Change in pH and [Cl^-] as a function of time for AST-1 and AST-2 experiments.

AST-1

Table 4.1 lists the average PR for straight bar specimens of each alloy during the successive 28-day exposures of the six individual AST-1 runs. Likewise, table 4.2 shows the average PR for the individual straight bar specimens of each alloy. Figure 4.2 plots polarization resistance, PR, versus exposure time for straight, as-received bars and illustrates the range of behavior and data scatter that characterized these measurements. Thus, PR data scatter was relatively large (in excess of one order of magnitude) for the most resistant alloy represented here (316.18 as well as for 2205); but the overall trend was generally constant with time. Data scatter was less and conformed to a downward trend with time for MMFX-II™, 3Cr12, and black bars. This probably reflects localized passive film instabilities in the case of 3Cr12; however, these were probably

less of a factor, if a factor at all, for the actively corroding MMFX-II™ and black bars for which progressive oxygen concentration polarization was controlling. The decrease in PR with time, where this occurred, reflects an effect of time per se rather than increased [Cl^-], since the decay showed no abrupt changes at the times of Cl^- additions.

Table 4.1. Average polarization resistance for each alloy during each 28-day period of six individual AST-1 runs.

	Average Polarization Resistance (Run 1), ohm/cm^2					
	316(18)	2201P	MMFX	MMFX-A	MMFX-D	BB
3% NaCl	1.89E+06	6.59E+04	5.43E+04	5.43E+04	3.83E+04	2.16E+03
9% NaCl	1.71E+06	5.71E+04	1.98E+04	2.78E+04	2.13E+04	1.26E+03
15% NaCl	2.83E+06	3.07E+04	1.39E+04	1.29E+04	1.73E+04	8.15E+02

	Average Polarization Resistance (Run 2), ohm/cm^2						
	316(18)	2201	2201P	MMFX	MMFX-A	MMFX-D	BB
3% NaCl	3.19E+06	5.78E+04	8.13E+04	5.82E+04	7.30E+04	3.75E+04	2.71E+03
9% NaCl	4.18E+06	5.42E+04	5.85E+04	2.55E+04	3.04E+04	3.03E+04	1.68E+03
15% NaCl	6.60E+06	4.98E+04	1.49E+05	1.29E+04	1.41E+04	2.92E+04	8.86E+02

	Average Polarization Resistance (Run 3), ohm/cm^2							
	316(18)	2205	2201	2201P	MMFX	MMFX-A	MMFX-D	BB
3% NaCl	3.97E+06	6.83E+04	5.91E+04	5.30E+04	5.87E+04	3.69E+04	3.06E+04	2.37E+03
9% NaCl	2.84E+06	7.37E+04	7.01E+04	4.84E+04	2.01E+04	1.31E+04	1.66E+04	1.19E+03
15% NaCl	3.57E+06	6.85E+04	4.75E+04	3.08E+04	1.15E+04	8.18E+03	1.00E+04	9.00E+02

	Average Polarization Resistance (Run 4), ohm/cm^2						
	316(16)	316(16)	3Cr12	3Cr12	Stelax	Stelax-A	Stelax-D
3% NaCl	1.54E+06	2.61E+06	3.75E+04	4.57E+04	2.40E+04	4.45E+04	2.94E+04
9% NaCl	2.02E+06	1.52E+06	2.78E+04	2.52E+04	1.05E+04	1.76E+04	7.18E+03
15% NaCl	1.65E+06	2.22E+06	1.19E+04	1.31E+04	9.76E+03	1.81E+04	4.71E+03

	Average Polarization Resistance (Run 5), ohm/cm^2							
	316(16)	3Cr12	Stelax	Stelax-A	Stelax-D	SMI	SMI-A	SMI-D
3% NaCl	1.50E+06	3.59E+04	9.51E+04	5.72E+04	2.58E+04	3.06E+05	2.91E+05	1.65E+05
9% NaCl	2.24E+06	2.95E+04	5.46E+04	5.80E+04	1.26E+04	3.03E+05	3.38E+05	1.32E+04
15% NaCl	6.88E+05	1.83E+04	5.74E+04	3.63E+04	1.16E+04	1.78E+05	1.77E+05	1.23E+04

	Average Polarization Resistance (Run 6), ohm/cm^2					
	SMI	SMI-A	SMI-D	SMI	SMI-A	SMI-D
3% NaCl	6.09E+05	4.59E+05	7.45E+04	7.83E+05	3.59E+05	8.49E+04
9% NaCl	4.58E+05	4.09E+05	2.26E+04	5.63E+05	4.52E+05	1.37E+04
15% NaCl	2.87E+05	4.14E+05	1.45E+04	1.59E+05	6.72E+05	1.26E+04

Table 4.2. Polarization resistance for each alloy averaged over the six individual AST-1 runs.

	Average Polarization Resistance (all runs), ohm/cm^2							
	316(18)	316(16)	2205	2201	2201P	MMFX	MMFX-A	MMFX-D
3% NaCl	3.E+06	2.E+06	7.E+04	6.E+04	7.E+04	6.E+04	5.E+04	4.E+04
9% NaCl	3.E+06	2.E+06	7.E+04	6.E+04	5.E+04	2.E+04	2.E+04	2.E+04
15% NaCl	4.E+06	2.E+06	7.E+04	4.E+04	7.E+04	1.E+04	1.E+04	2.E+04
	3Cr12	BB	Stelax	Stelax-A	Stelax-D	SMI	SMI-A	SMI-D
3% NaCl	4.E+04	2.E+03	5.E+04	5.E+04	2.E+04	6.E+05	4.E+05	1.E+05
9% NaCl	3.E+04	1.E+03	3.E+04	3.E+04	1.E+04	4.E+05	4.E+05	2.E+04
15% NaCl	1.E+04	9.E+02	4.E+04	2.E+04	7.E+03	2.E+05	4.E+05	1.E+04

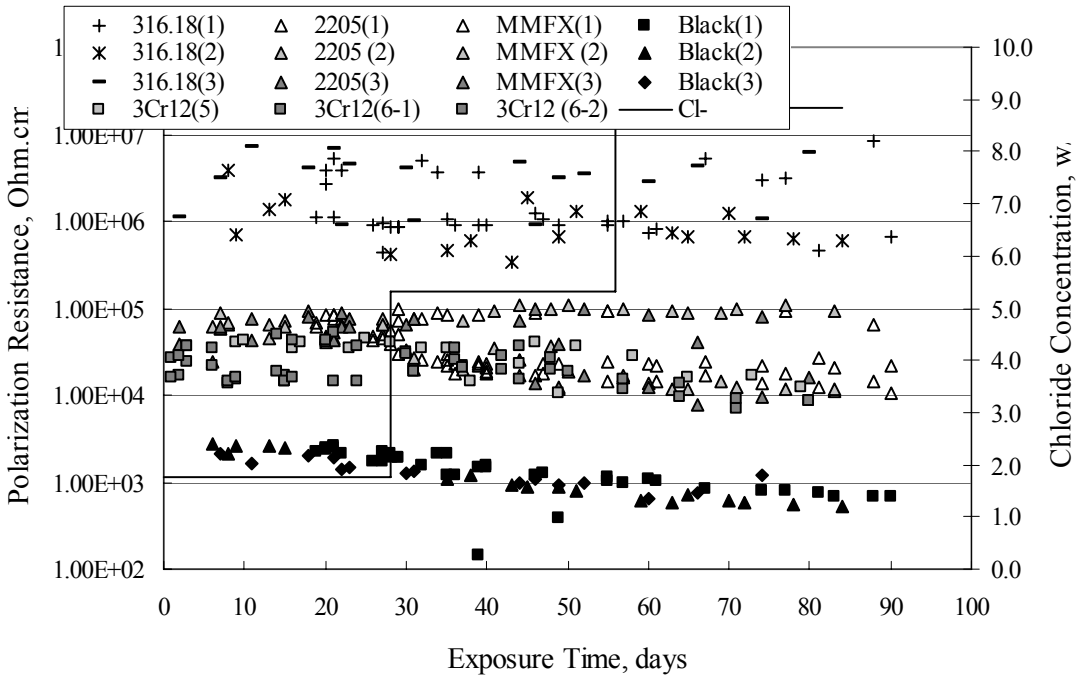

Figure 4.2. Graph. Plot of polarization resistance versus exposure time for representative alloys during different AST-1 runs (numbers in parentheses).

Figure 4.3 reproduces the 2205, MMFX-II™, 3Cr12, and black bar data from figure 4.2 but with results for 2201 added. The more expanded PR scale allows these results to be viewed in greater detail. This shows that PR for 2205, 2201, MMFX-II™, and 3Cr12 were in the range 10^4 to 10^5 Ω·cm^2, with 2205 occupying the upper bound, MMFX-II™ ad 3Cr12 the lower, and 2201 intermediate. The black bar data, on the other hand, are in the range 10^3 to 10^4 Ω·cm^2. As noted above, PR for MMFX-II™, 3Cr12, and black bar decreased with exposure time, whereas values for 2205 tended to remain constant. The 2201 data are intermediate in that these exhibit a slight downward trend during the third phase of the exposure. The data in each case are from

three different runs; and it was concluded from the reproducibility between these for the different rebar types that any run-to-run variations were within the range of inherent data scatter.

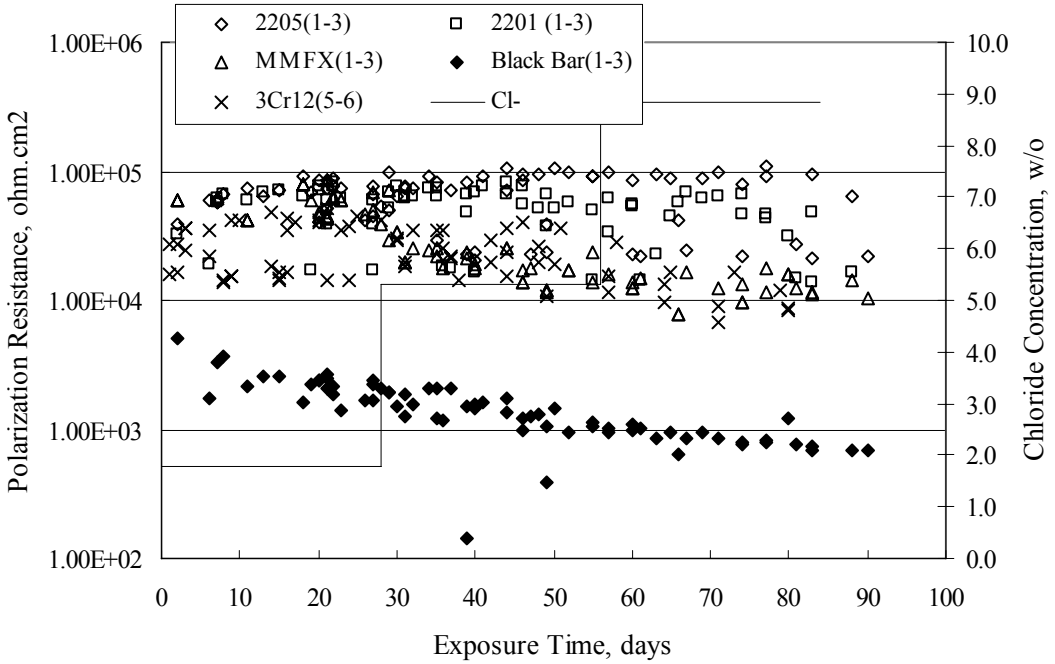

Figure 4.3. Graph. Plot of polarization resistance versus exposure time for intermediate performing alloys and black bars during different AST-1 (number in parentheses after each alloy designation indicates different AST-1 runs.

Figure 4.4 plots PR versus exposure time for 2201 stainless steel specimens with different surface preparations, including as-received (see table 3.1), steel shot (Fe) blasted, stainless steel (SS) shot blasted, and silica sand blasted. The data referenced as "Jensen Beach" pertain to 2201 reinforcement that was acquired from a bridge construction site in Jensen Beach, FL, and was from the same heat as the other 2201 specimens; but the Jensen Beach bars had been silica sand surface blasted. These bars experienced about 6 weeks of uncovered atmospheric exposure approximately 1 km inland prior to being acquired. The sand blasted specimens exhibit PR values that approach being an order of magnitude greater than the as-received and metal blasted ones but with a trend where the former merged with the latter as the 84-day exposure progressed.

Figure 4.5 plots PR versus exposure time for the two 316 stainless steel clad bars (Stelax and SMI), in comparison to data for solid 316 stainless steel bars. The results show that PR for the SMI bars averaged about one order of magnitude below that for the solid SS bars but with some data overlap. Data for the Stelax are about two orders of magnitude below those for the solid bars. Differences in surface condition are thought to be responsible for these variations. Likewise, figure 4.6 shows this same clad bar data along with results for the abraded (A) and damaged (D) surface conditions. Little difference is apparent between intact and abraded bars; but the damaged clad resulted in the lowest PR values, which were generally the same for both clad bar types.

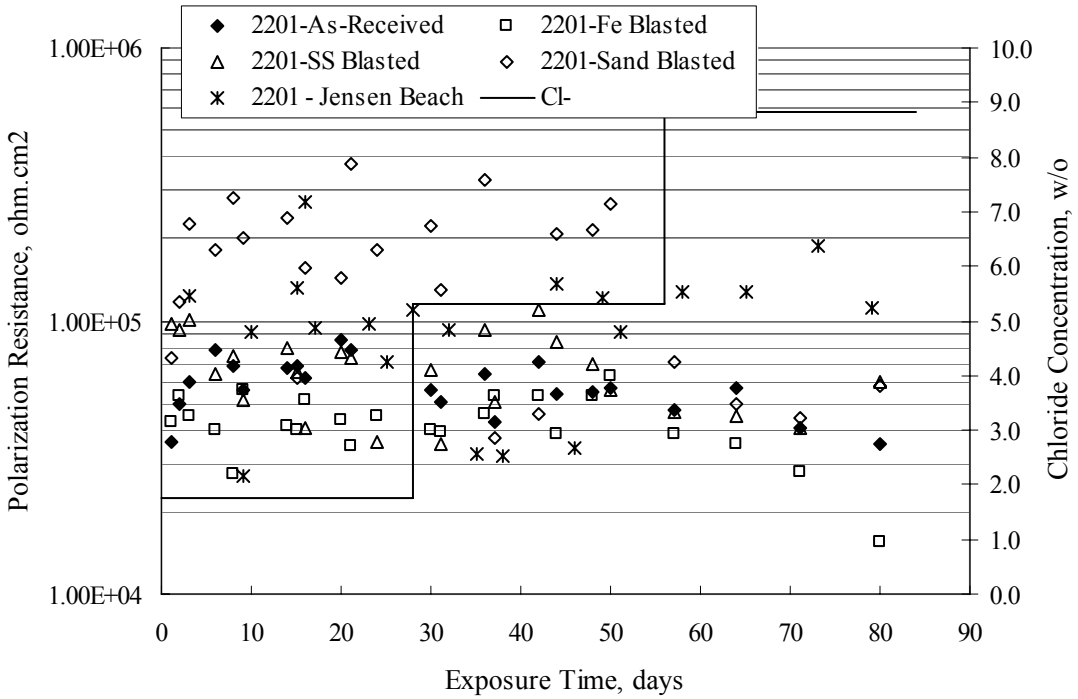

Figure 4.4. Graph. Plot of polarization resistance versus exposure time for 2201 stainless steel AST-1 specimens with different surface preparation conditions.

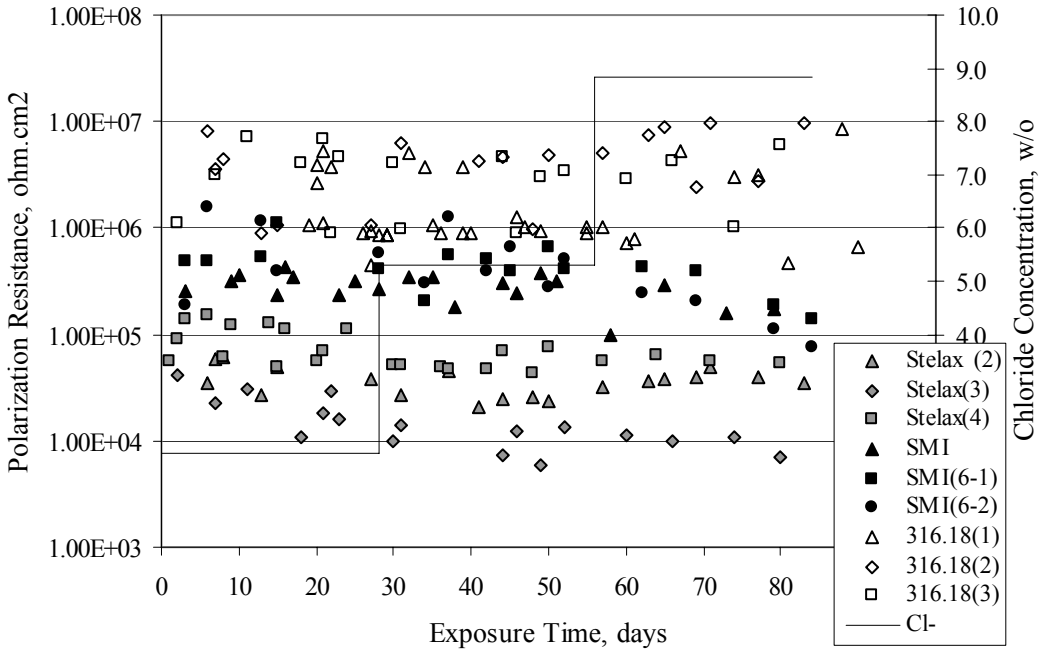

Figure 4.5. Graph. Plot of polarization resistance versus exposure time for clad stainless steel AST-1 specimens.

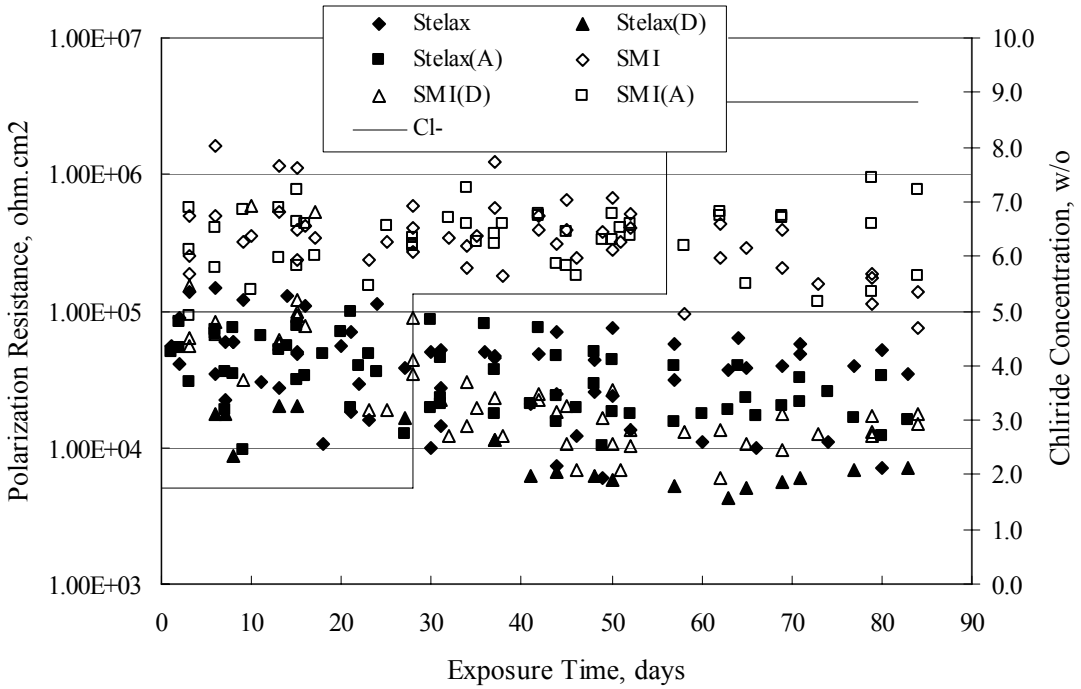

Figure 4.6. Graph. Plot of polarization resistance versus exposure time for clad stainless steel AST-1 specimens in the intact, abraded (A), and damaged (D) conditions.

Figure 4.7 plots PR for straight versus bent solid bars. If both specimen types had the same corrosion rate, then PR for each should be the same and the data lay along the 1:1 line. In general, such a correlation is apparent but with some displacement to higher PR (lower corrosion rate) for the bent bars. The reason for this is unclear. Likewise, figure 4.8 shows a similar plot for the two types of clad bars. Here also, the data track has a 1:1 correlation but with more scatter than for the solid bars. Consistent with figure 4.6, the undamaged SMI bars exhibit PRs about an order of magnitude greater than for the Stelax ones. Also, damage apparently had only a modest effect on PR of Stelax bars but reduced PR for SMI bars to the same range as for the damaged Stelax.

Table 4.3 lists the average corrosion rate for runs 1 through 4 (weight loss determinations were not made for runs 5 and 6) calculated from weight loss for specimens of each alloy (equation 3.3) at the end of the indicated 28-day period. Likewise, table 4.4 shows the average corrosion rate for each alloy averaged over the different runs in cases where the same alloy was used in different runs. Figure 4.9 shows a comparison between these corrosion rates as calculated from weight loss and from PR (equation 3.2). Data for the intermediate performers (3Cr12, MMFX-II™, 2201, and 2205) generally track the 1:1 trend; however, the PR based corrosion rate for black bars exceeds that from weight loss with the opposite trend being apparent for 316, both by almost an order of magnitude. The B value for 316 would have to increase to 0.40 V and the black bar decrease to 0.008 V, both of which seem unrealistic, to bring these two data sets to the 1:1 line. A possible explanation for data displacement from the 1:1 line is that PR in the present experiments reflects corrosion rate during the submerged portion of the wet-dry cycle, whereas weight loss averaged attack during both periods. Reconciling the two sets of data on this

basis requires then that corrosion rate of the 316 was greater during the nonsubmerged phase and black bar greater during the submerged phase.

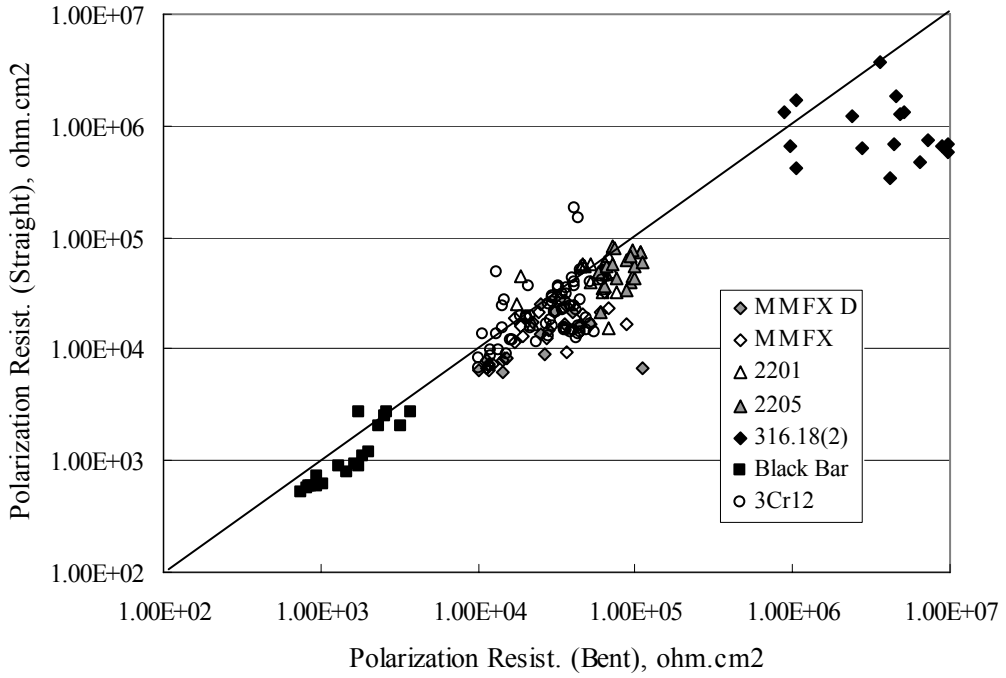

Figure 4.7. Graph. Plot of polarization resistance for straight versus bent solid bars.

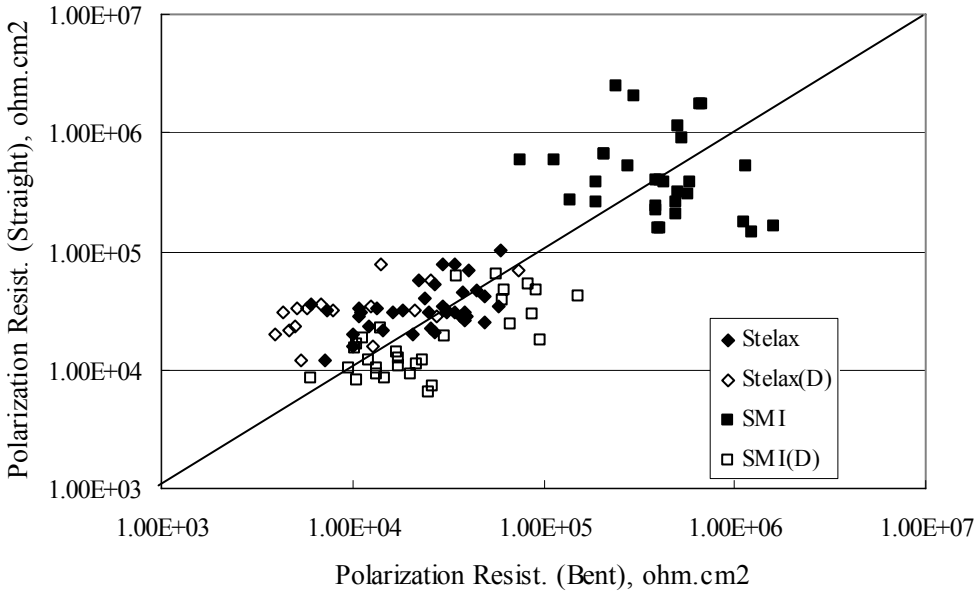

Figure 4.8. Graph. Plot of polarization resistance for straight versus bent clad bars.

Table 4.3. Corrosion rate calculated from weight loss of individual specimens of each alloy at the end of the indicated NaCl exposure for the indicated run.

	Corrosion Rate (Run 1), mmpy						
	316(18)	2201	2201P	MMFX	MMFX-A	MMFX-D	BB
3% NaCl	0.004	0.005	0.006	0.013	0.009	0.009	0.070
9% NaCl	0.001	0.007	0.008	0.015	0.010	0.016	0.063
15% NaCl	0.001	0.004	0.003	0.017	0.007	0.012	0.058

	Corrosion Rate (Run 2), mmpy						
	316(18)	2205	2201	2201P	MMFX	MMFX-A	MMFX-D
3% NaCl	0.005	0.013	0.020	0.008	0.013	0.008	0.001
9% NaCl	0.002	0.007	0.010	0.005	0.011	0.007	0.009
15% NaCl	0.001	0.004	0.008	0.004	0.015	0.012	0.012

	Corrosion Rate (Run 3), mmpy							
	316(18)	2205	2201	2201P	MMFX	MMFX-A	MMFX-D	BB
3% NaCl	0.003	0.006	0.003	0.012	0.008	0.016	0.009	0.057
9% NaCl	0.001	0.005	0.007	0.006	0.011	0.017	0.013	0.052
15% NaCl	0.001	0.004	0.005	0.004	0.013	0.014	0.013	0.040

	Corrosion Rate (Run 4), mmpy			
	316(16)	316(16)	3Cr12	3Cr12
3% NaCl	0.001	0.001	0.026	0.025
9% NaCl	0.002	0.001	0.020	0.018
15% NaCl	0.001	0.001	0.024	0.019

Table 4.4. Average corrosion rate calculated from weight loss for each alloy during four individual AST-1 runs.

	Corrosion Rate, mmpy				
	316(18)	316(16)	2205	2201	2201P
3% NaCl	0.004	0.001	0.008	0.009	0.009
9% NaCl	0.001	0.001	0.005	0.008	0.006
15% NaCl	0.001	0.001	0.004	0.005	0.004
	MMFX	MMFX-A	MMFX-D	3Cr12	BB
3% NaCl	0.011	0.011	0.006	0.025	0.070
9% NaCl	0.012	0.011	0.013	0.019	0.057
15% NaCl	0.015	0.011	0.012	0.021	0.048

1 mA/m^2 = 0.1 $\mu A/cm^2$ = 0.0011 mm/year = 1.15 μm/year = 0.043 mils/year.

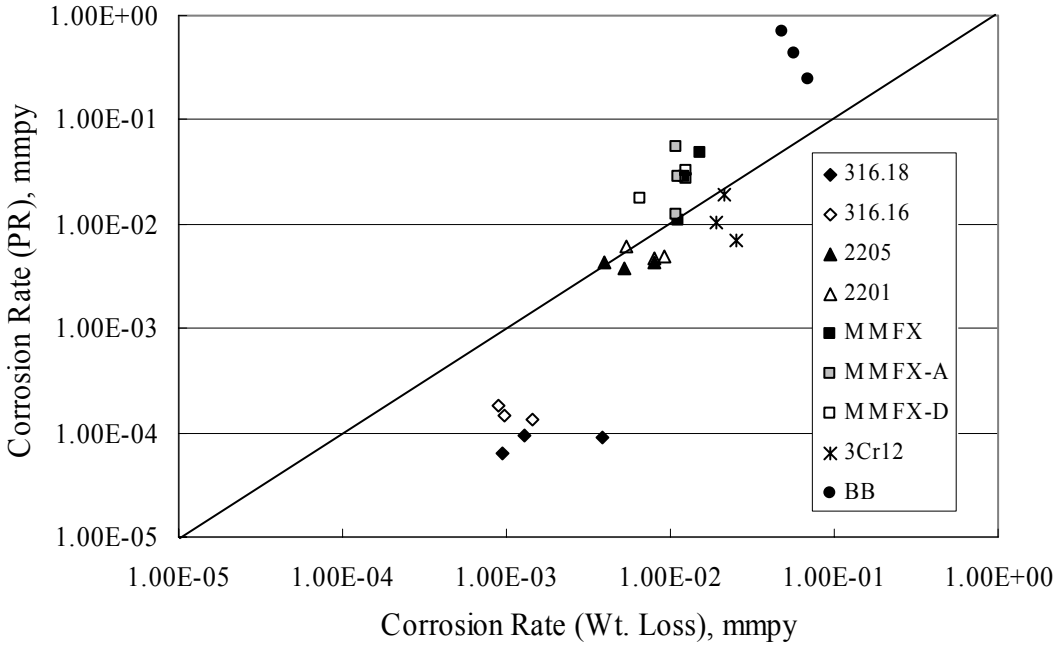

Figure 4.9. Graph. Comparison of corrosion rate measured by weight loss and calculated from polarization resistance for different solid bars.

Figures 4.10 through 4.16 show photographs of representative specimens subsequent to testing. In each case, testing of the uppermost specimen in the photographs was terminated after 28 days, the middle one after 56 days, and the one at the bottom after 84 days or slightly later. With the exception of the 316 reinforcement, all three specimens of which appear pristine, there was a general trend whereby specimens appeared more corroded with successive 28-day exposures. The visual appearances generally conform to the PR and weight loss results in that bars with more corrosion products typically exhibited lower PR and higher weight loss.

---

1 mA/m^2 = 0.1 $\mu A/cm^2$ = 0.0011 mm/year = 1.15 μm/year = 0.043 mils/year.

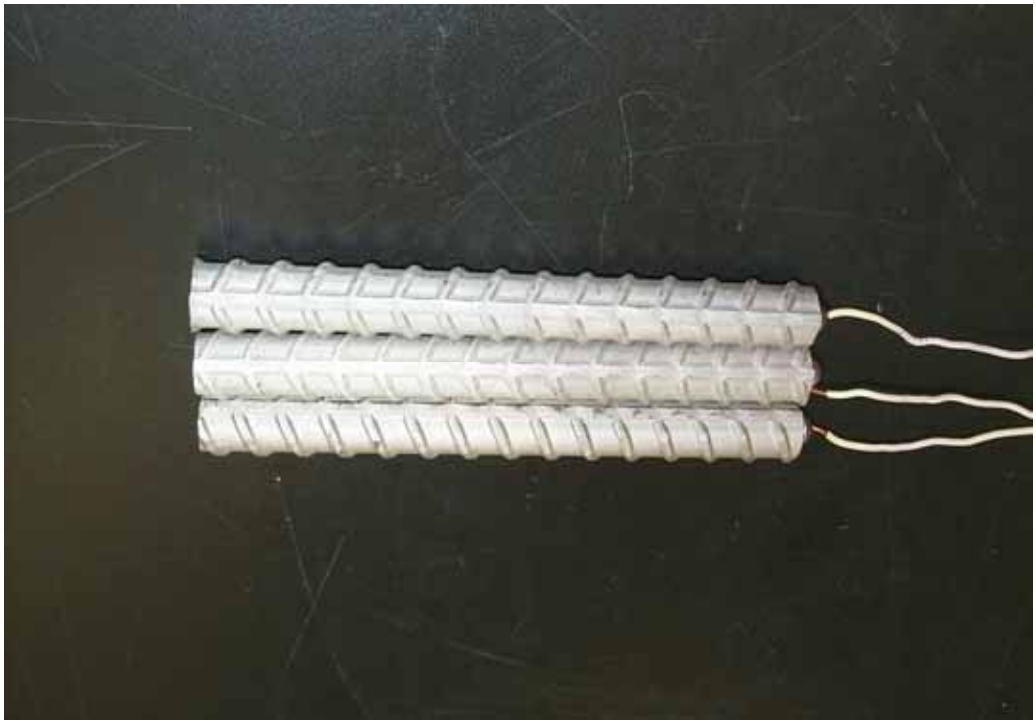

Figure 4.10. Photo. Type 316 SS specimens subsequent to AST-1 testing.

Figure 4.11. Photo. Type 2205 SS specimens subsequent to AST-1 testing.

Figure 4.12. Photo. Type 2201 SS specimens subsequent to AST-1 testing.

Figure 4.13. Photo. MMFX-II™ specimens subsequent to AST-1 testing.

Figure 4.14. Photo. MMFX-II™ abraded specimens subsequent to AST-1 testing.

Figure 4.15. Photo. MMFX-II™ damaged specimens subsequent to AST-1 testing.

Figure 4.16. Photo. Black bar specimens subsequent to AST-1 testing.

AST-2A

Figure 4.17 plots current density to maintain a potential of +100 mV_{SCE} versus $[Cl^-]$ for an initial experiment (run number 1, table 3.4) that involved one specimen of each alloy except MMFX-II™ with various surface conditions included where applicable. Only the initial time scale is shown here so that activation time of bars with relatively poor and intermediate corrosion resistance could be more accurately discerned. Initially, current density was several μA or less for all bar types. Corrosion was defined as having initiated when current density reached 10 $\mu A/cm^2$, and the $[Cl^-]$ at which this occurred is indicated from the right Y axis. This reveals that the black bar specimen activated in response to the initial Cl^- increment (0.30 w/o), followed by the 3Cr12 at 0.60 w/o Cl^-, various MMFX-II™ specimens in the range 0.60-1.30 w/o Cl^-, and 2201 at 1.30 w/o Cl^-. The 2205 and 316 specimens exhibited current densities below the defined activation threshold (10 $\mu A/cm^2$) for all Cl^- increments shown here. Similarly, figure 4.18 plots data from this same experiment at longer times and higher $[Cl^-]$, where activation for some of the more corrosion resistant bars occurred. While some data are obscured, it can be seen that the single damaged Stelax bar activated at 2.12 w/o Cl^- and the damaged SMI at 6.37 w/o Cl^-.

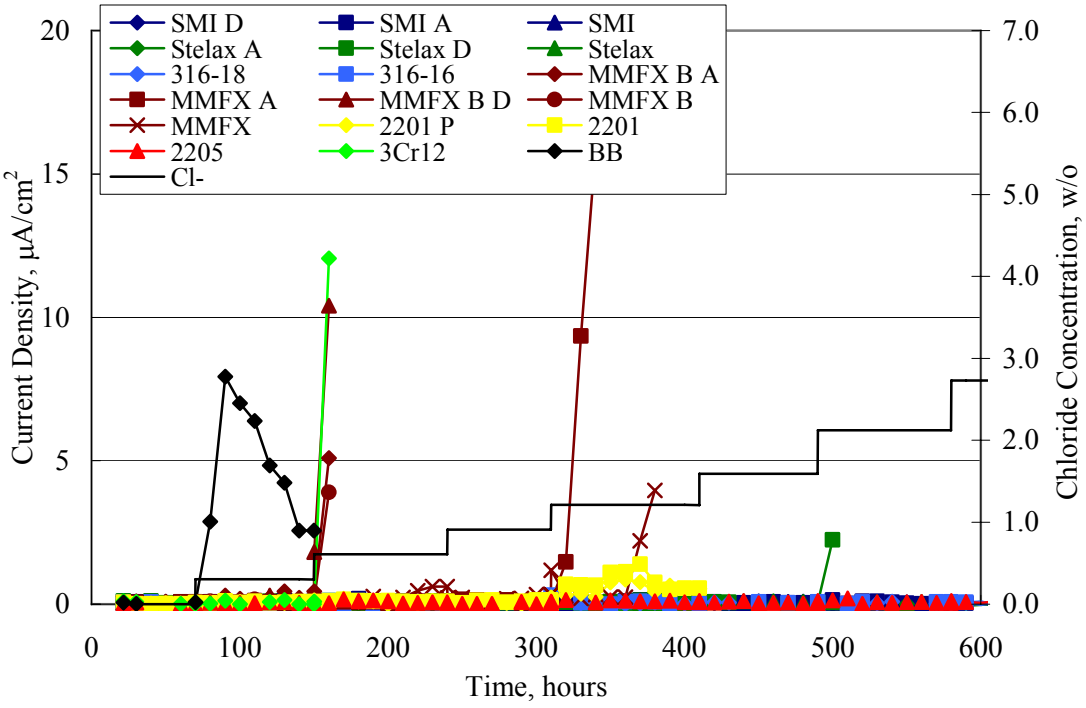

Figure 4.17. Graph. Plot of current density versus [Cl⁻] such that $[Cl^-_{th}]$ for alloys with intermediate corrosion resistance is revealed (specimens with B in the designation were bent).

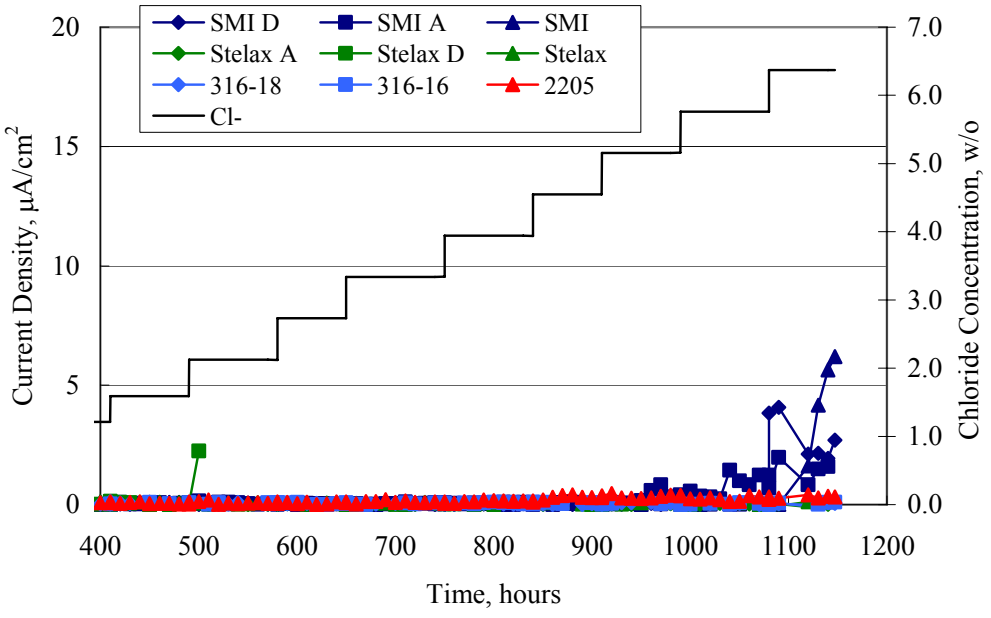

Figure 4.18. Graph. Plot of current density versus [Cl⁻] such that $[Cl^-_{th}]$ for alloys with relatively high corrosion resistance is revealed.

Performance was mixed for the other clad bar specimens with an abraded and an undamaged SMI specimen activating at 5.16 and 6.37 w/o Cl^-, respectively. Post exposure observations indicated that in the former case the abrasion penetrated the cladding; and in the latter, attack initiated underneath the end sealing epoxy. Corrosion also occurred underneath the epoxy for the bar designated as Stelax B (bent), which also activated at 6.37 w/o Cl^-, and at cladding breaks caused by bending. Figure 4.19 provides extends the scale from figure 4.18 to longer times so that data for the best performers can be viewed in greater detail. Thus, maximum current density for the two 316, Stelax, and SMI bars was less than one $\mu A/cm^2$ except in cases where there was intentional damage (D) or where the end sealing of the clad bars failed. Data for the 2205 bar beyond about 850 hours was cyclic with a maximum current density of about five $\mu A/cm^2$. As such, performance of the latter alloy in AST-2A was considerably better than in AST-1. Thresholds for the more corrosion resistant bars may have been higher if pH had been maintained constant (see figure 4.1). The experiment was terminated after approximately 1,150 hours because of a power shutdown mandated in September 2004 by Hurricane Frances.

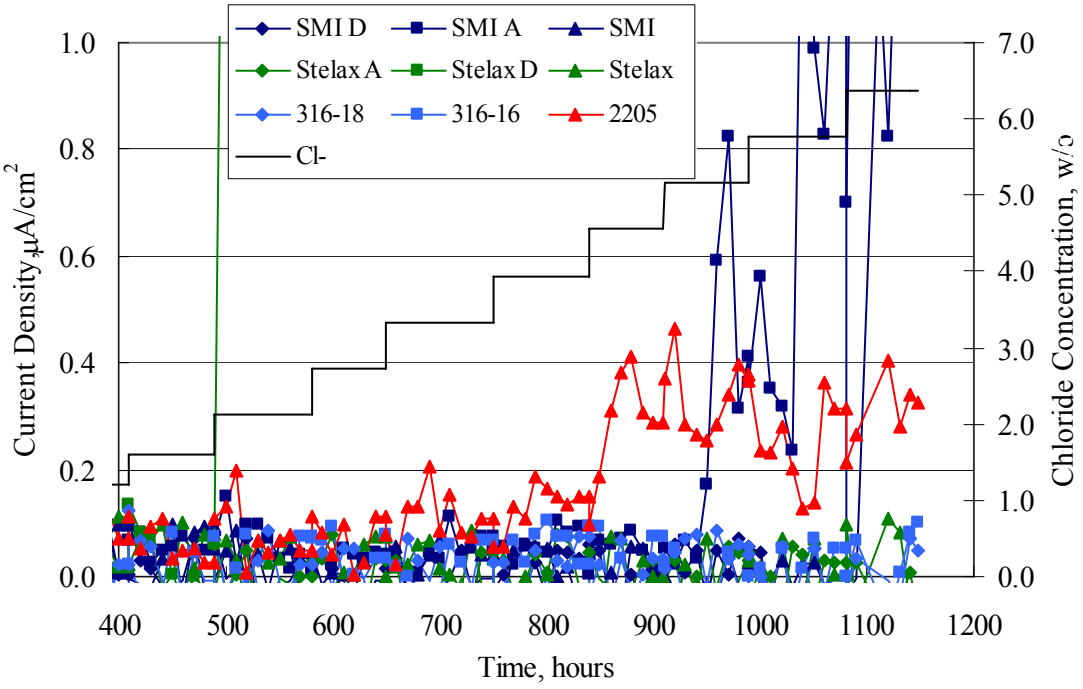

Figure 4.19. Graph. Expanded scale plot of current density versus [Cl^-] for alloys with relatively high corrosion resistance is revealed.

Second and third AST-2A experiments were performed for the purpose of better defining $[Cl^-_{th}]$ for black bar, 3Cr12, MMFX-II™ and 2201. This involved concurrently testing 10 bars of the individual alloys and using smaller Cl^- increments than for the initial run. Specimens were preconditioned in the simulated pore water at +100 mV_{SCE} for 5 days before the first Cl^- addition. Testing of individual specimens was in some cases terminated once current density exceeded 10 $\mu A/cm^2$. Figures 4.20 and 4.21 show plots of current density versus exposure time for black and 3Cr12 specimens, the latter with a more expanded vertical axis for better resolution. Likewise, figure 4.22 presents results for MMFX-II™ and 2201. Because of data clutter and the fact that

$\left[Cl^-_{th}\right]$ was reached earlier for MMFX-II™ specimens, figure 4.23 shows data for the latter specimens only. The above plots exhibit noise as a consequent of repetitive passive film breakdown and repair. Also, apparent is the arbitrariness of the 10 μA/cm^2 criterion. Irrespective of this, figure 4.24 presents a cumulative distribution plot of $\left[Cl^-_{th}\right]$ for each of the four alloys.

AST-2B

Open Circuit Potential

In general, free corrosion potential for specimens in these tests decreased during the initial 400 seconds of exposure by on average about 100 mV and decayed more gradually or remained constant thereafter. No definitive relationship between this potential and [Cl^-] was apparent; however, the decay at a given [Cl^-] was generally reproducible.

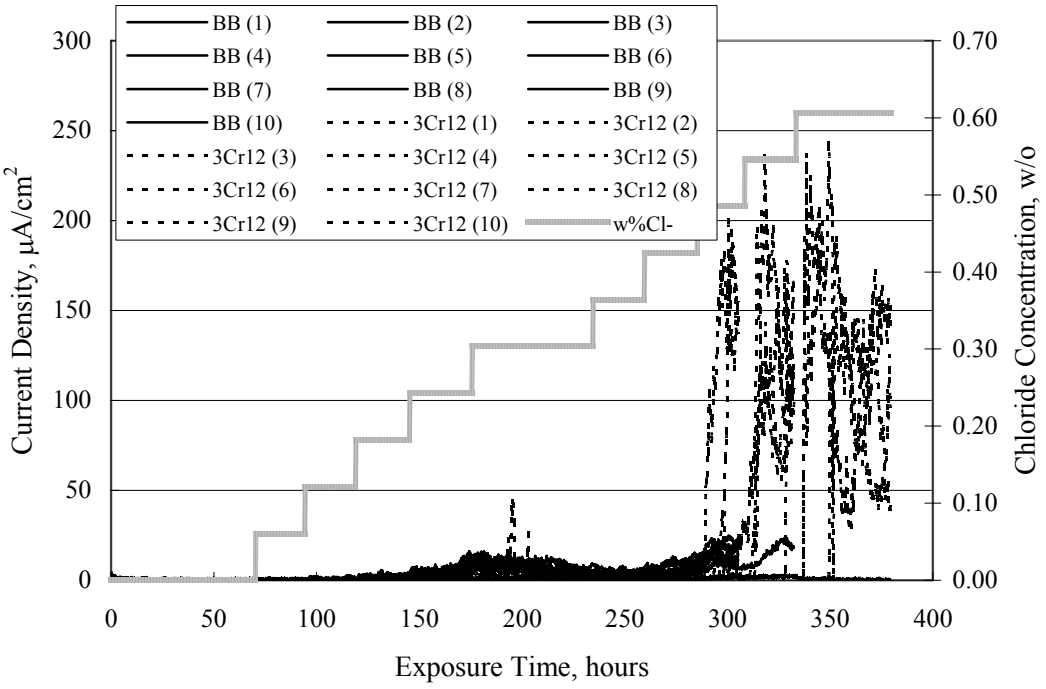

Figure 4.20. Graph. Plot of current density versus exposure time for 10 specimens each of black bar and 3Cr12. Incremental Cl^- additions are also shown.

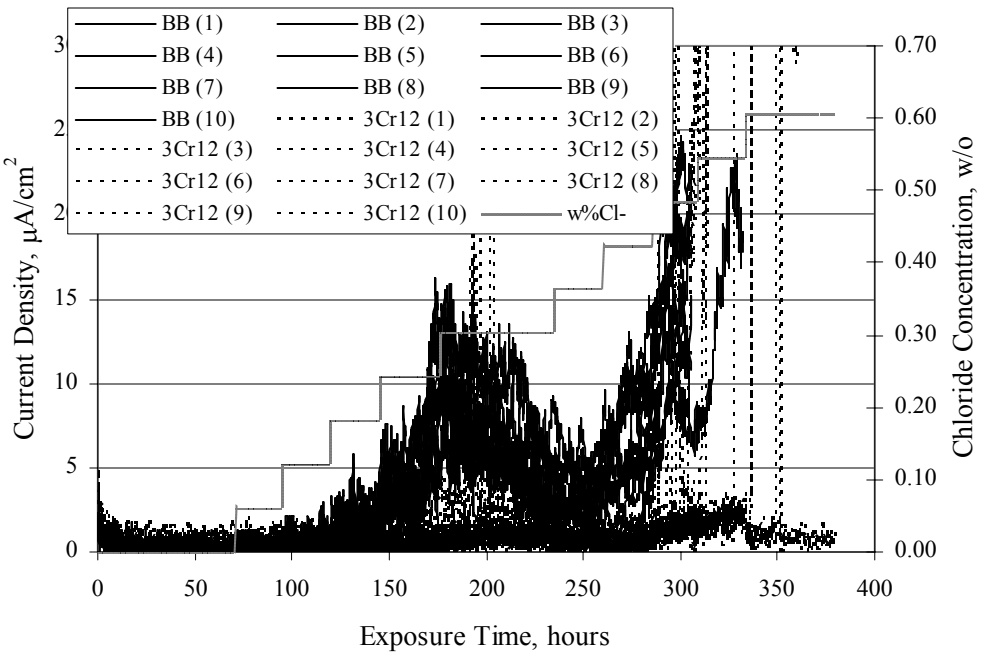

Figure 4.21. Graph. Expanded scale view of the current density versus exposure time data from figure 4.20.

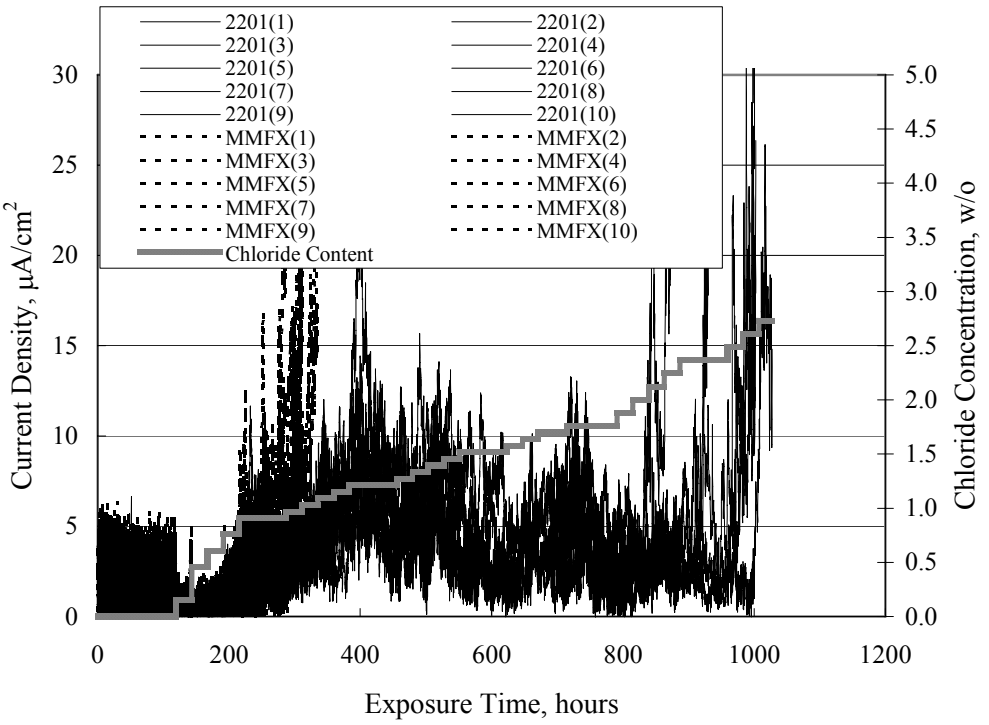

Figure 4.22. Graph. Plot of current density versus time for a series of 10 MMFX and 2201 specimens polarized to +100 mV_{SCE}. Incremental Cl^- additions are also shown.

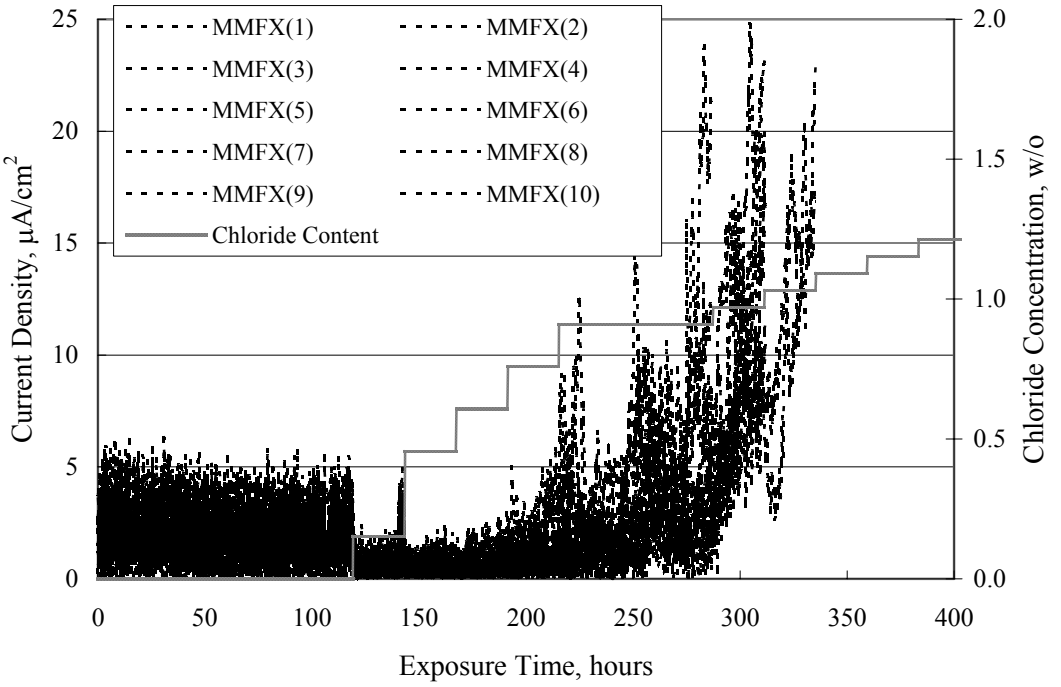

Figure 4.23. Graph. Plot of current density versus time for replicate MMFX-II™ specimens.

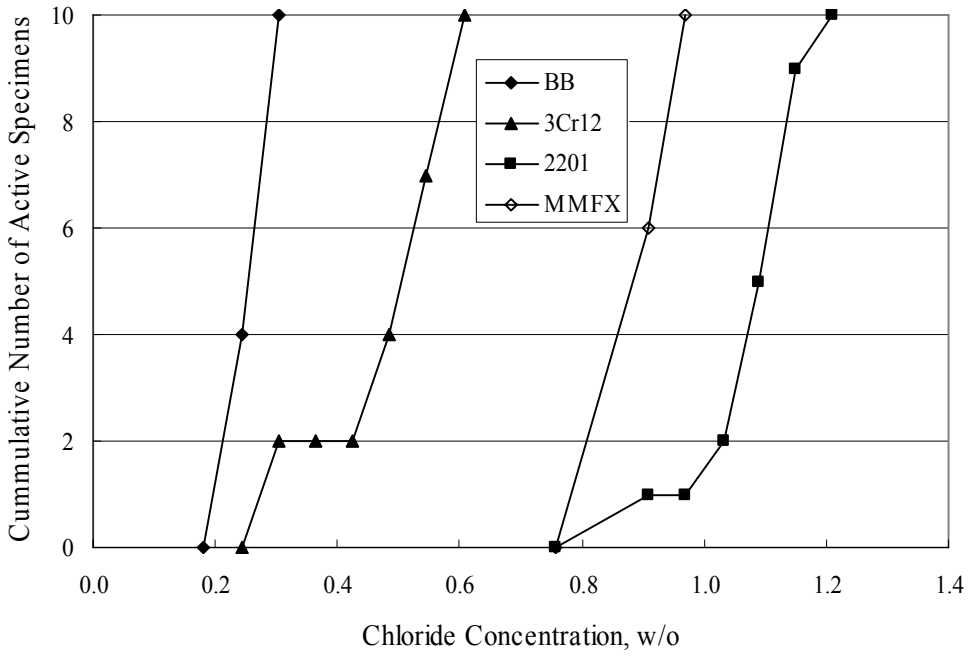

Figure 4.24. Graph. Distribution of $\left[Cl^-_{th}\right]$ for four alloys based upon the 10 μA/cm^2 current density criterion.

Scan Rate

Figure 4.25 presents cyclic potentiodynamic polarization (CPP) scans for cross section polished MMFX-II™ specimens in saturated $Ca(OH)_2$ without Cl^- showing that current density at a given potential increased with increasing scan rate. Similar to the potentiostatic procedure (AST-2A), the critical pitting potential, E_{pit}, was defined as the potential corresponding to a current density of 10 $\mu A/cm^2$. The scans illustrate the arbitrariness of this definition, however, in that a small change in this criterion could alter E_{pit} by as much as several hundred millivolts.

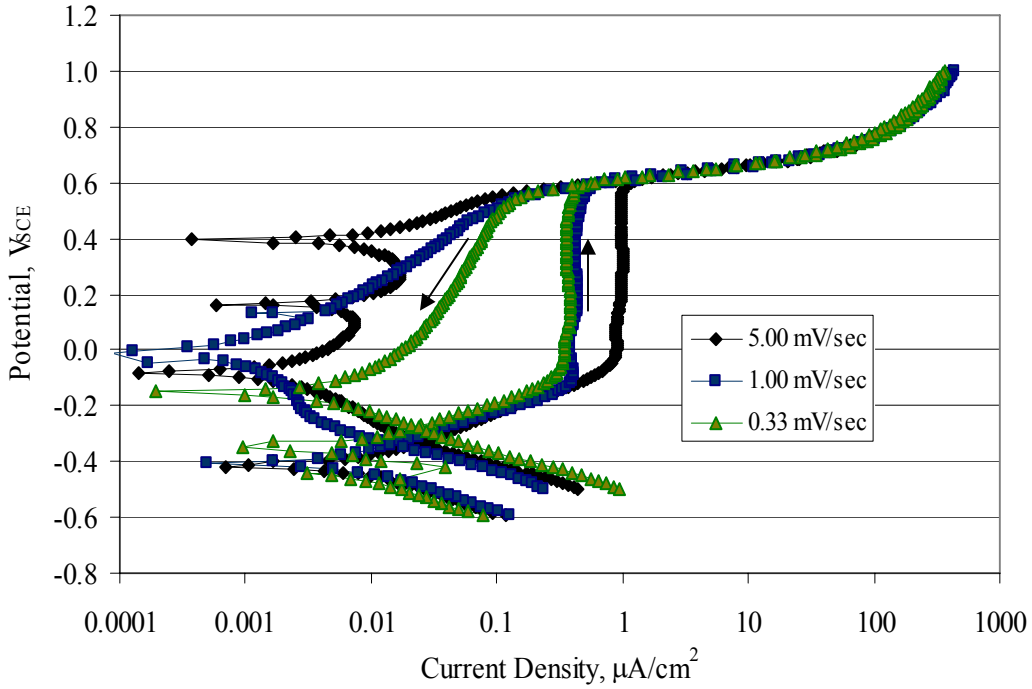

Figure 4.25. Graph. Anodic CPP scans for as-received MMFX-II™ specimens in saturated $Ca(OH)_2$ without Cl^- at scan rates of 0.33, 1.00, and 5.00 mV/s. Arrows indicate direction of forward and reverse scans.

Surface Condition

Figure 4.26 presents CPP scans for MMFX-II™ specimens in saturated $Ca(OH)_2$ with 0.50 w/o Cl^- and shows that E_{pit} for the specimen with the as-received surface finish was more negative than for the 600 grit polished ones by about 200 mV or more based on the 10 $\mu A/cm^2$ criterion. A similar trend was disclosed for 2201. Surface effects were not studied in the case of the other bars. This result by itself indicates that bars with as-rolled mill scale have inferior pitting resistance to ones where this is removed, as is generally known; however, surface cleaning methods such as pickling and blasting negatively affect cost and from this standpoint render corrosion resistant reinforcement less competitive.

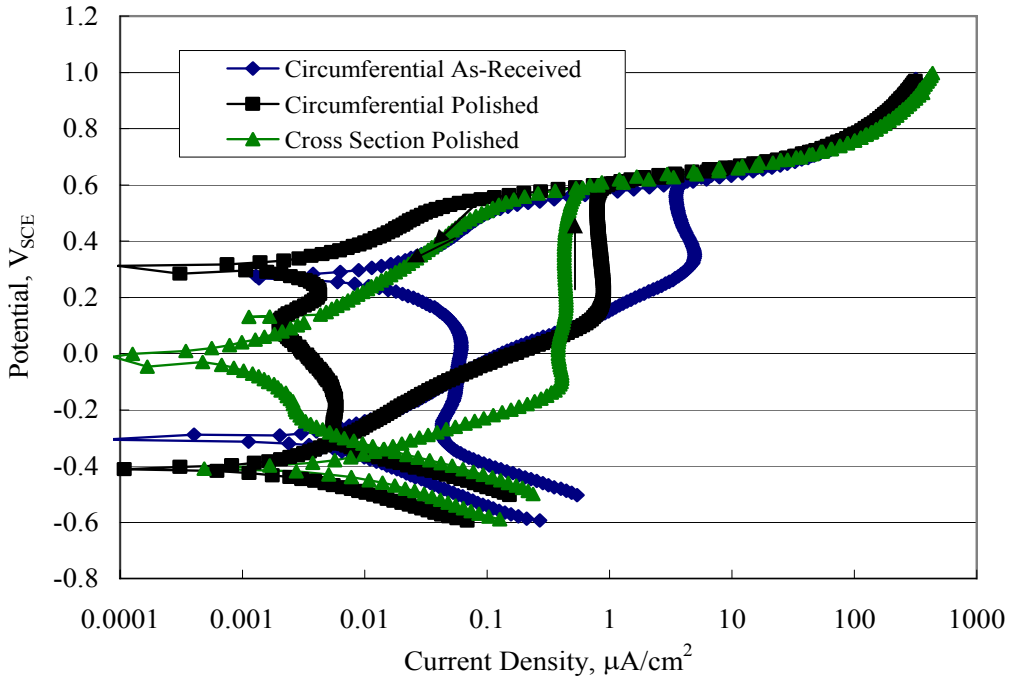

Figure 4.26. Graph. Anodic CPP scans on as-received MMFX-II™ specimens with three surface conditions in saturated $Ca(OH)_2$ without Cl^- at 1.00 mV/s. Arrows indicate direction of forward and reverse scans.

Critical Pitting Potential

From CPP scans performed on 3Cr12, MMFX-II™, 2201, and 316.16, E_{pit} was determined as a function of [Cl^-] with results being as shown in figure 4.27. This reveals that, for the bar types represented here, E_{pit} for 3Cr12 is the most active and for 316.16 the most noble with the average for MMFX-II™ and 2201 being essentially the same. That this latter finding does not agree with results from AST-2A (figure 4.24) may have resulted because of the sensitive dependence of E_{pit} on [Cl^-] in the 0-1.0 w/o Cl^- range in saturated $Ca(OH)_2$ (pH ~ 12.45) and the fact that the potentiostatic tests were in synthetic pore solution (pH ~ 13.2).

CORRELATIONS BETWEEN DIFFERENT SHORT-TERM TEST RESULTS

The Pitting Resistance Equivalent Number, PREN (alternatively, PRE), as defined by the expression,

$$PREN = w/oCr + 3.3 \cdot w/oMo + x \cdot w/oN \quad (4.1)$$

(w/o is weight percent of the indicated element and x is commonly chosen as 16), is widely employed for selection of stainless steels in applications where corrosion by pitting is a concern. PREN values for the reinforcements employed in the present study are listed in table 3.1. Polarization resistance (PR), on the other hand, is an electrochemical parameter that is inversely

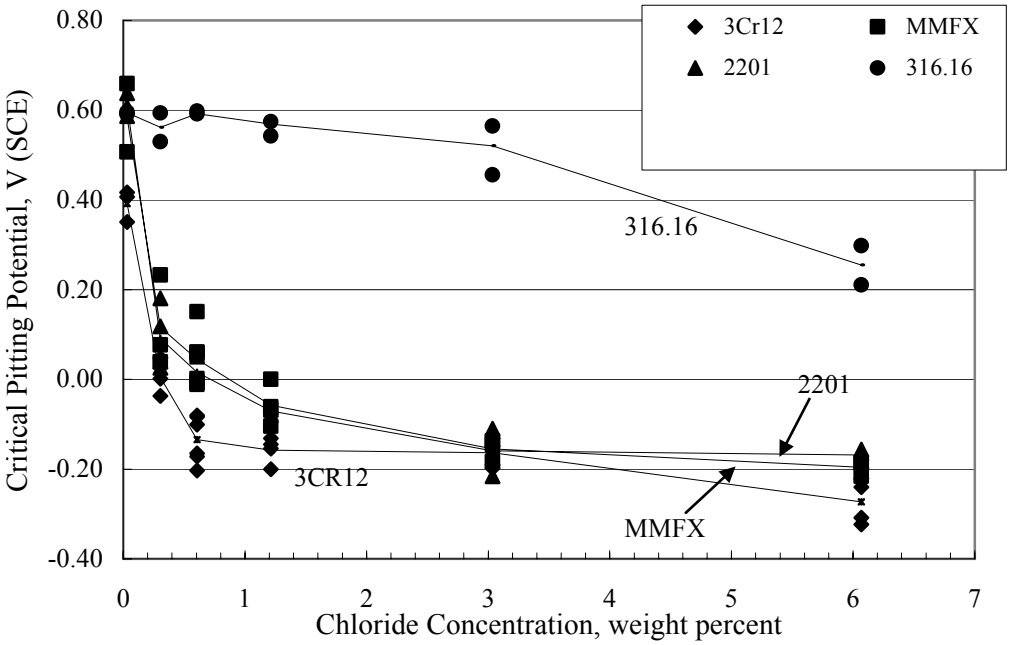

Figure 4.27. Graph. Critical pitting potential as a function of [Cl^-] for four bar types.

proportional to uniform corrosion rate. An attempt was made to correlate the AST-1 PR results with the respective PREN for the different alloys. To this end, figure 4.28 plots PR versus PREN for the relevant alloys. The results reveal almost two orders of magnitude difference in PR between 2201 and 316.18 despite the fact that the PREN for each is about the same. Also, 2205 has the highest PREN, but its PR is comparable to that for 2201 and is also well below that of 316.18. These differences may be a consequence of the 316.18 having been pickled, whereas 2201 and 2205 were tested in the as-rolled condition (MMFX-II™ and black bar also were tested as-rolled). On the other hand, PR of 2201 specimens with various surface treatments (AST-1 tests) did not vary greatly from that of the as-received material (figure 4.4). Also, corrosion of the 2201 and 2205 specimens appeared to be uniform in the AST-1 exposures rather than by pitting (see figures 4.11 and 4.12); and this being the case, a pitting index (PREN) may not apply. An added contributing factor to the lack of correlation may be that the PREN parameter is empirical and was established based upon exposure in acidic and marine environments rather than alkaline ones. Nonetheless, a trend of increasing PR with increasing PREN is apparent if the 316.18 datum is ignored.

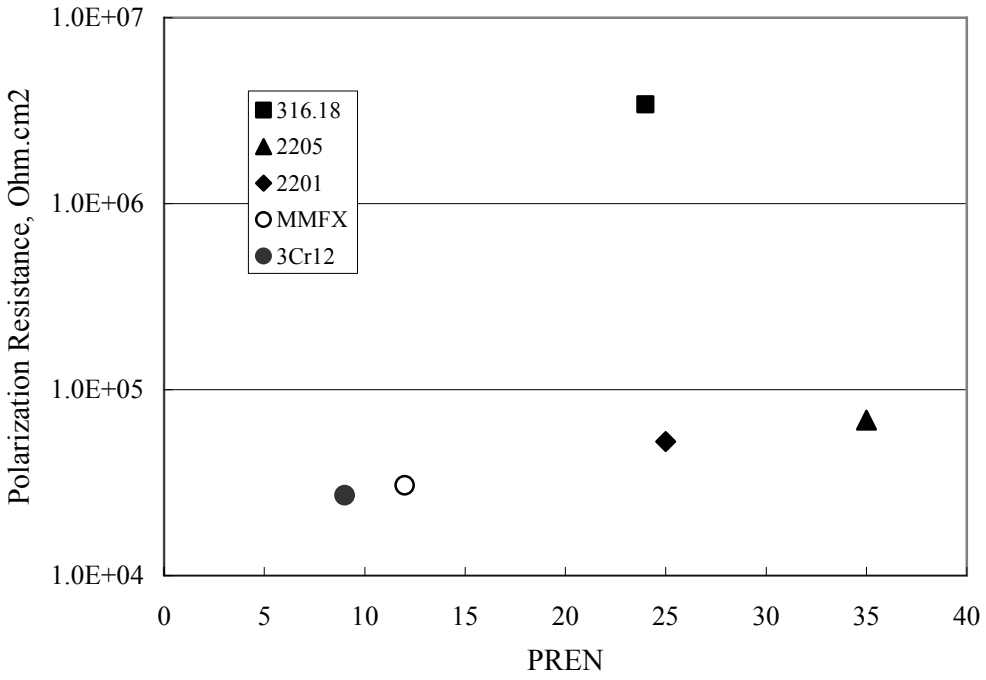

Figure 4.28. Graph. Plot of polarization resistance (AST-1) versus PREN for the test reinforcements.

Figure 4.29 shows a plot of average PR (AST-1) versus $\left[Cl^-_{th}\right]$ (AST-2A) for solid bars and reveals a trend of increasing threshold with increasing PR for alloys of low and intermediate corrosion resistance with an apparent relatively abrupt transition in $\left[Cl^-_{th}\right]$ from relatively low to high at a PR near $6 \cdot 10^4$ $\Omega \cdot cm^2$. Again, the distinction in performance of 2205 in these two tests is apparent in that this alloy exhibited a relatively high $\left[Cl^-_{th}\right]$; but PR was intermediate and in the same range as the 2201 and MMFX-II™ reinforcements. This may reflect the fact that these two parameters (PR and $\left[Cl^-_{th}\right]$) were measured under different exposure conditions and that they represent different aspects of bar response (uniform corrosion rate for the former and the threshold condition for passive film breakdown for the latter). It can be reasoned also that pH of the residual, high $[Cl^-]$ moisture on AST-1 bars during the periods of atmospheric exposure was reduced and that this affected behavior during the submerged periods. If this was the case, then PR values for the bar types other than 316 are indicative of postactivation corrosion, whereas for 316 $\left[Cl^-_{th}\right]$ reflects a criterion for active corrosion initiation.

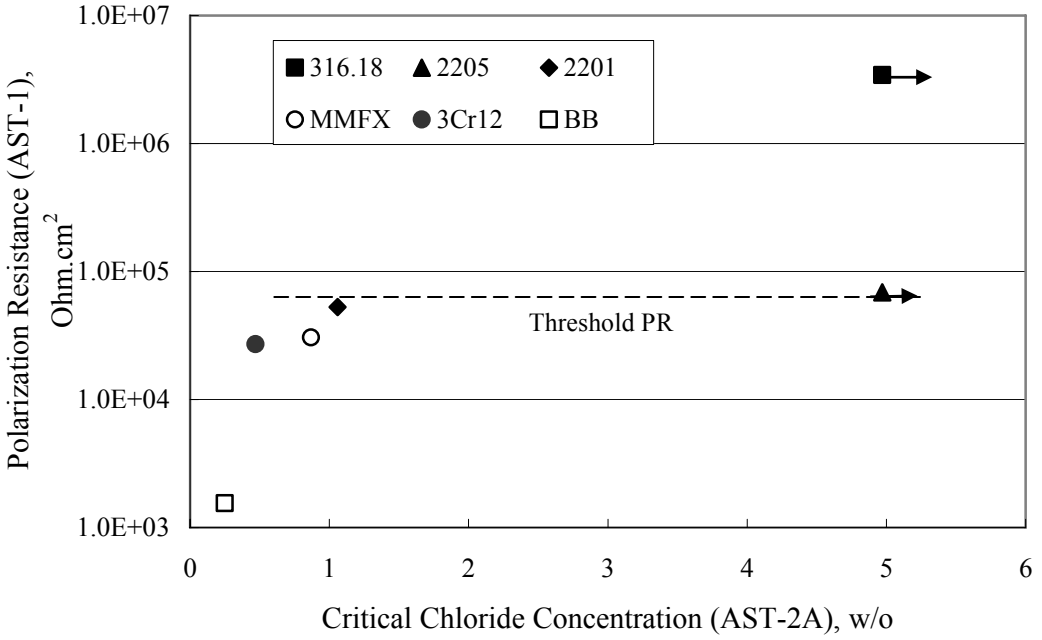

Figure 4.29. Graph. Plot of polarization resistance (AST-1) versus $\left[Cl^-_{th}\right]$ (AST-2A).

Figure 4.30 plots $\left[Cl^-_{th}\right]$ (AST-2A) versus PREN and again shows lack of a consistent trend by the better performers to the extent that data are available. While the results indicate a transition of $\left[Cl^-_{th}\right]$ from low to high at about PREN 25, additional tests on other alloys are required to confirm that this constitutes a true performance demarcation.

The $[Cl^-]$ corresponding to an E_{pit} of +100 mV_{SCE} from AST-2B experiments was compared with the $\left[Cl^-_{th}\right]$ determinations for the AST-2A ones. Thus, $\left[Cl^-_{th}\right]$ at this potential for 3Cr12 in AST-1 was estimated from figure 4.27 as 0.25 w/o for MMFX-II™ and 0.30 w/o for 2201. These values are less than those from AST-2A (0.9 w/o for MMFX-II™ and 2.0 w/o for 2201, see above); however, this is not unexpected given that pH of the electrolyte was lower in AST-2B than AST-2A (saturated $Ca(OH)_2$ compared to synthetic pore solution). Also, the E_{pit} data are based on relatively few data points; and these fall in a range where E_{pit} was relatively sensitive to $[Cl^-]$.

RELATING $\left[Cl^-_{th}\right]$ (AST-2A) TO CHLORIDE THRESHOLD CONCENTRATIONS IN CONCRETE

Relating the presently determined $\left[Cl^-_{th}\right]$ values from the AST-2A experiments to Cl^- thresholds in actual concrete, C_T, is difficult since, first, the free Cl^- concentration in the cement pore water, $[Cl^-]_f$, is not a simple function of C_T and, second, C_T depends upon numerous factors including water/cement ratio, cement content and composition, exposure conditions, and others. Nonetheless, Li and Sagüés[18] summarized $[Cl^-]_f$ data for black bar from the literature, most of which were determined by pore water expression (PWE) using water saturated cement pastes, mortars, and concretes, and correlated these with the corresponding C_T values that were reported.

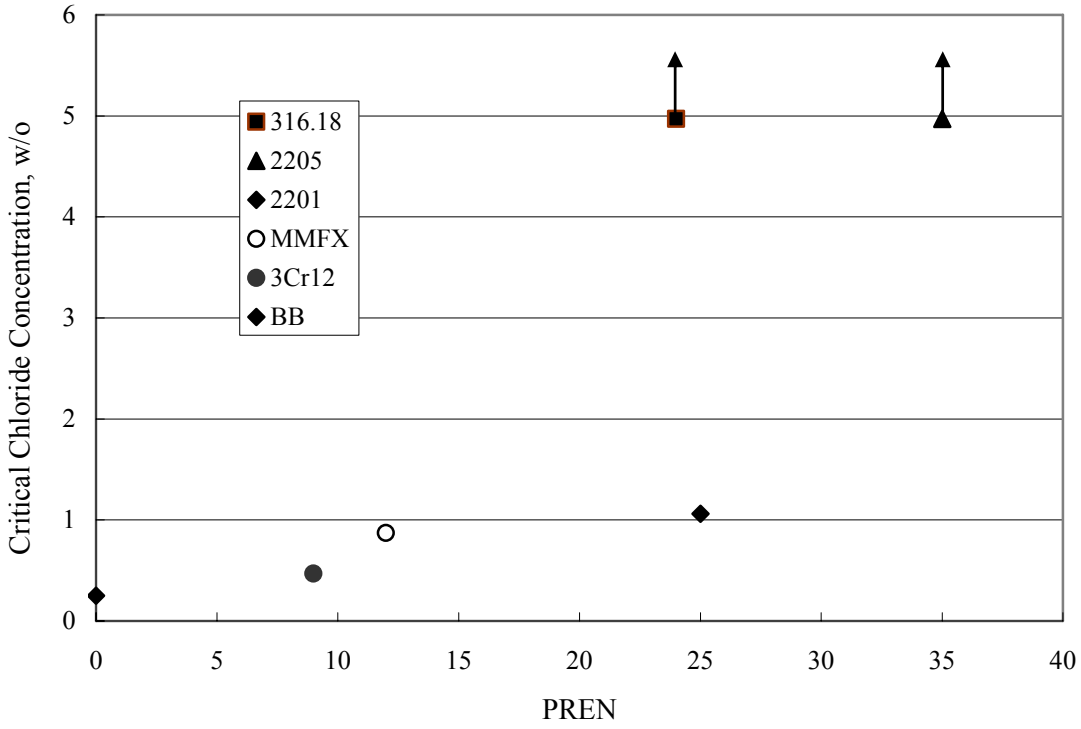

Figure 4.30. Graph. Plot of $\left[Cl^-_{th}\right]$ (AST-2A) versus PREN.

In the present analysis, it was assumed that the $\left[Cl^-_{th}\right]$ values determined from the AST-2A experiments are comparable with the $[Cl^-]_f$ values summarized by Li and Sagüés. On this basis, figure 4.31 shows a plot of $\left[Cl^-_{th}\right]$ (AST-2A) versus the corresponding threshold projected for concrete. Here, the two curves are the upper and lower limits of the literature $[Cl^-]_f - C_T$ data, and the $\left[Cl^-_{th}\right]$ are plotted as the midpoints of the C_T extremes. Also, is reported as molarity, M, since the PWE data employed this unit of measure. Table 4.5 lists the values for $\left[Cl^-_{th}\right]$ and C_T that are plotted in figure 4.31. Such an analysis does not, of course, constitute an explicit $\left[Cl^-_{th}\right] - C_T$ correlation since the values for the latter parameter are inferred based upon a trend of historically reported results.

Table 4.5. Listing of projected C_T values for the corresponding $\left[Cl^-_{th}\right]$ from AST-2A.

Reinforcement	$\left[Cl^-_{th}\right]$, M	Average C_T from Literature, weight percent cement
BB	0.08	0.54
3Cr12	0.15	0.80
MMFX-II™	0.27	1.10
2201	0.35	1.30

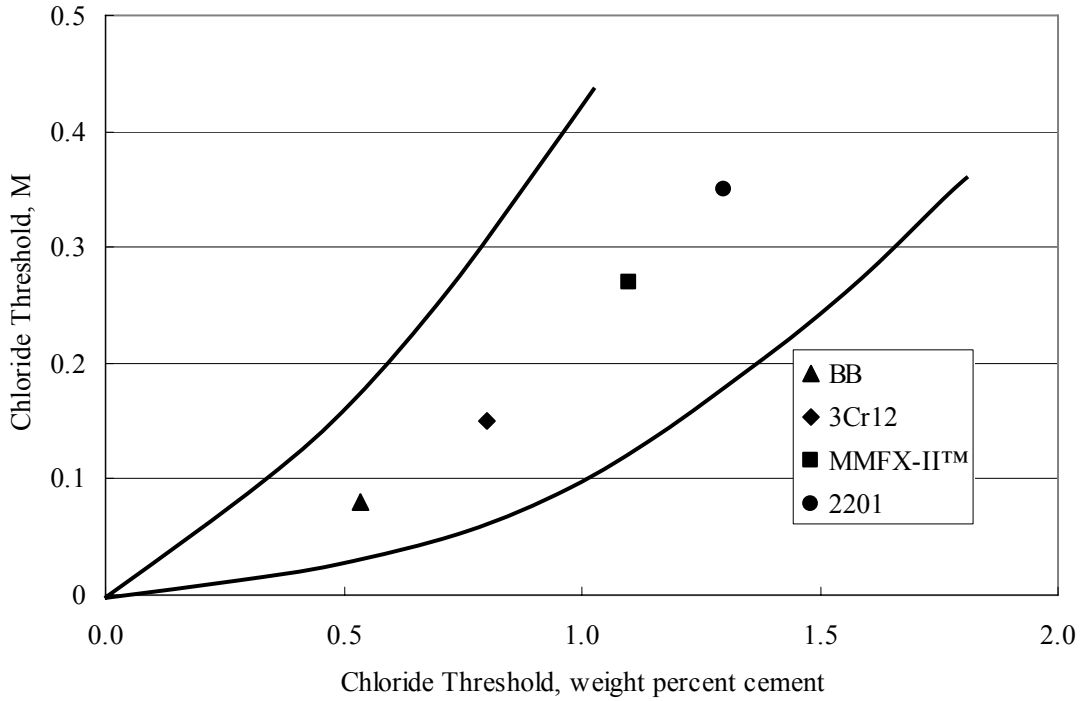

Figure 4.31. Graph. Plot of $\left[Cl^-_{th}\right]$ (AST-2A) versus the corresponding threshold projected from literature data for pastes, mortars, and concrete.

CONCRETE SPECIMENS

General

Data from potential measurements and, for some specimen types, macro-cell current density (calculated from voltage drop across a 10 Ω resistor between the two rebar mats) were evaluated as a function of exposure time as indicators of, first, the onset of corrosion and, second, corrosion rate subsequent to activation. Not all corrosion resistant reinforcement types have yet been investigated because of acquisition problems during the initial two project years and resultant delays in specimen fabrication and curing. Findings for each of the specimen types for which data are available are presented and discussed below.

Simulated Deck Slab (SDS) Specimens

General

The data for this specimen type must be qualified because no isolation of the reinforcement where it exited the concrete, other than the epoxy coating on the side concrete surfaces, was provided. In many cases, corrosion was apparent at the steel-concrete exterior interface; and this could have affected both potential and macro-cell current. Besides the three specimen sets mentioned earlier, a fourth set has been prepared with heat shrink tubing around the bars where

these emerge from the concrete to determine the extent to which this lack of isolation affected performance.

Black Bar Slabs

Figures 4.32 and 4.33 show plots of potential and macro-cell current density as a function of exposure time for the standard (no simulated crack) black bar slabs. Figure 4.32 indicates that, according to the −280 mV_{SCE} criterion, the STD1 bars (w/c 0.50) became active within weeks of initiating the Cl^- exposure. Also, corrosion has activated on bars in two of the three STD2 (w/c 0.41) slabs; however, the timing of this is not definitive in that, while potential for the former two specimens tended to more negative values between 100 and 150 days, this subsequently moderated with potential varying in the -200 to -300 mV_{SCE} range to about 450 days. Subsequently, a more negative trend with time reoccurred. The macrocell current density data (Figure 4.32) correlate with the potential data in that high current density corresponds to relatively negative potential.

Figures 4.34 and 4.35 show potential and macro-cell current density data for black bar specimens with and without a simulated crack. The data indicate that potential was more negative and current density higher initially for the cracked specimens compared to the uncracked ones but with the data merging at longer times, which is consistent with chlorides having immediate access, or nearly so, to steel in the cracked concrete case. However, as chlorides migrated into the uncracked concrete specimens by diffusion and became more concentrated at the steel depth, distinctions between the two data sets moderated.

Typically, potential tended to be more negative and macro-cell current density greater when

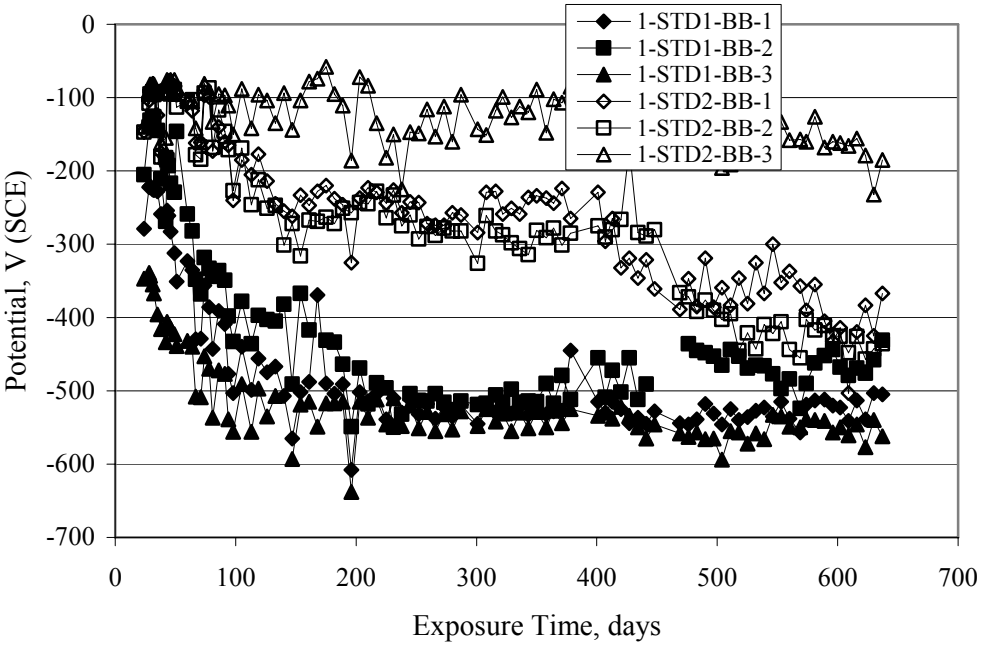

Figure 4.32. Graph. Plot of potential versus exposure time for STD1 and STD2 concrete specimens with black bar reinforcement.

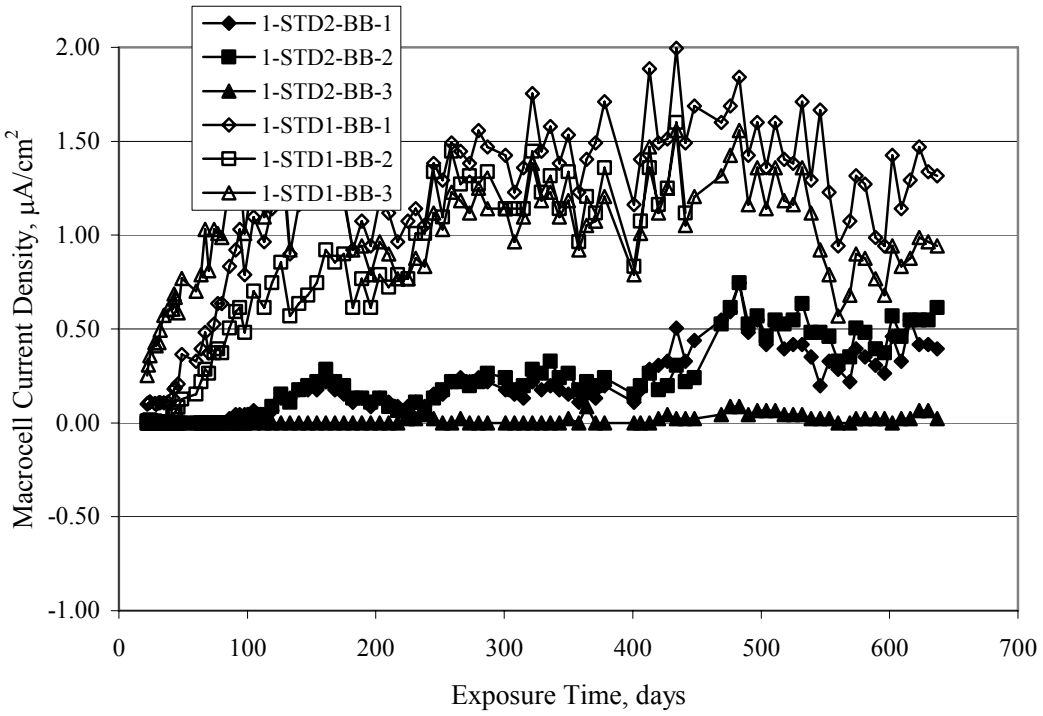

Figure 4.33. Graph. Plot of macro-cell current density versus exposure time for STD1 and STD2 concrete specimens with black bar reinforcement.

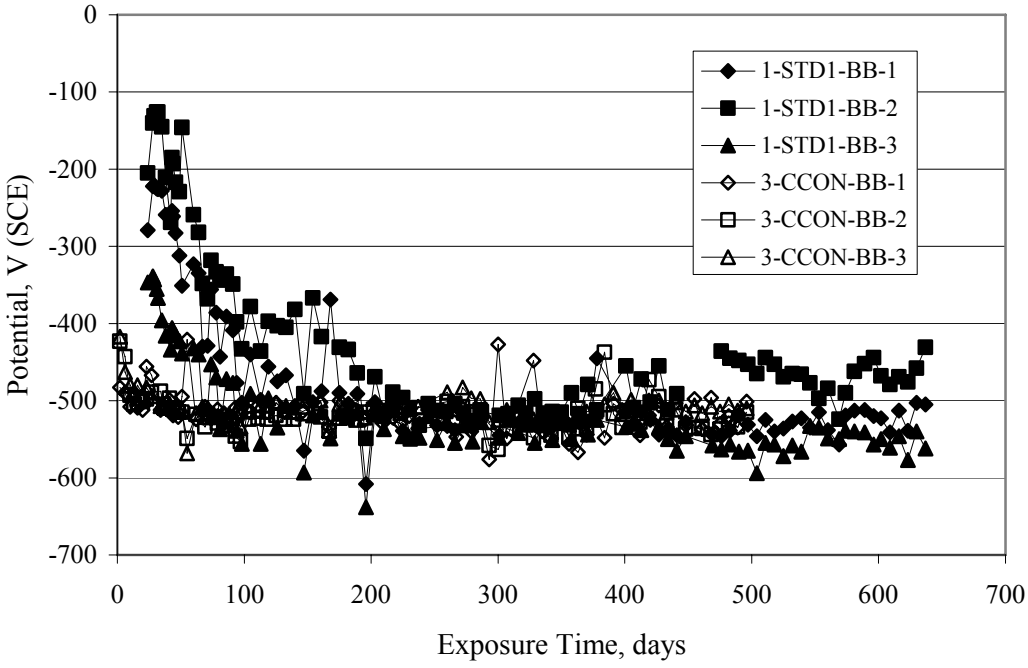

Figure 4.34. Graph. Plot of potential versus exposure time for black bar STD1 concrete specimens with and without a simulated crack.

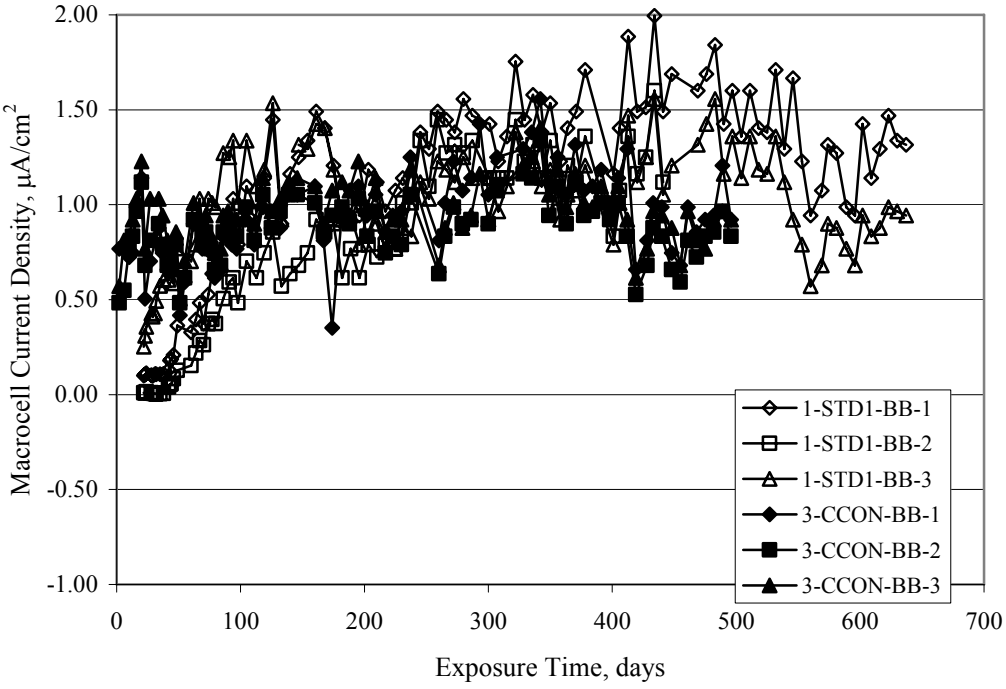

Figure 4.35. Graph. Plot of macro-cell current density versus exposure time for black bar STD1 concrete specimens with and without a simulated crack.

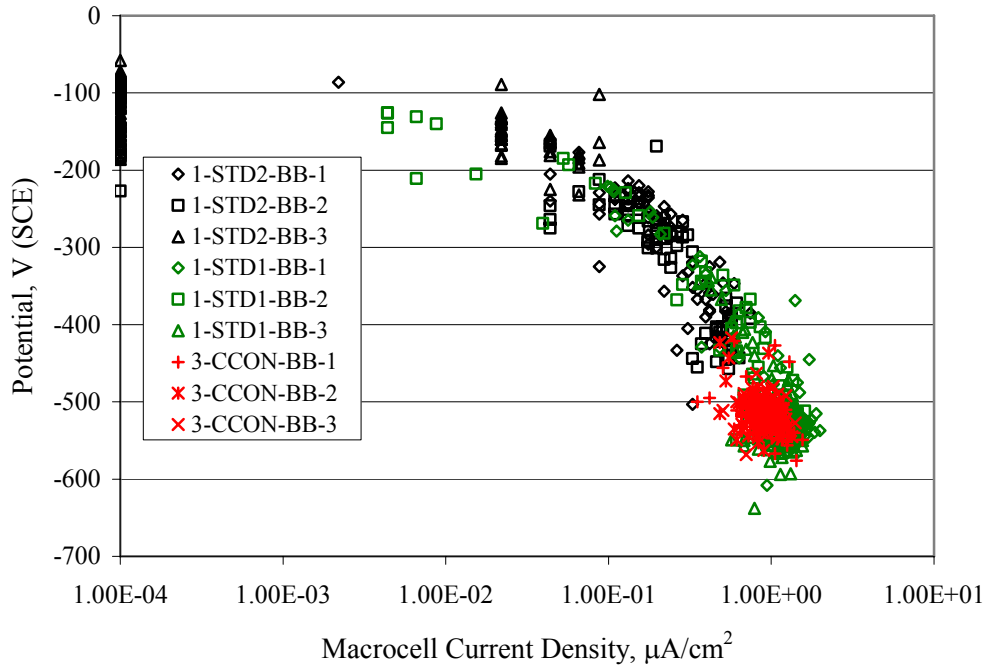

Figure 4.36. Graph. Plot of potential versus macro-cell current density for black bar reinforced concrete specimens.

measurements were made during the wet portion of the ponding cycle compared to the dry, both for black bar and the other reinforcement types discussed below. This accounts for the saw-tooth pattern that is apparent in much of the data. The effect is more apparent in the case of cracked concrete specimens than for the uncracked.

Figure 4.36 plots potential versus macro-cell current density for the black bar specimens. Since potential became more negative and macro-cell current density increased with exposure (figures 4.32 through 4.35), increasing time is from upper left to lower right. The data generally conform to a common band irrespective of w/c or presence of a simulated crack and differences between individual specimens, as viewed in the potential and macro-cell versus time formats (figures 4.32 through 4.35). However, results for the STD2 specimens do not extend as far down the trend band as do the other two specimen sets, consistent with these having maintained more positive potentials and developed less macro-cell current than the STD1 mix specimens. Also, the cracked concrete specimen data occupy only the relatively negative potential—high current density regime, consistent with a relatively high current density having occurred soon after exposure. Such a representation (potential versus current density) facilitates comparison of performance of the different specimen and bar types, as discussed subsequently.

Figure 4.37 shows a typical example of the black bar slabs after 377 days of exposure, in this case for a CCON type specimen. This shows rust surface staining emanating from the simulated crack and occurrence of an actual crack above one of the bars (circled). Several black bar slabs were subsequently autopsied by partially saw cutting and then splitting the concrete along the plane of the upper three bars. Figure 4.38 is a photograph of the trace of the upper side of the top rebars on the sectioned concrete face of specimen number 3-CCON-BB-1 after 566 days of exposure. Likewise, figure 4.39 shows the appearance of the upper bar traces for specimen number 1-STD-BB-3 after 707 days. Prior to sectioning, this specimen had been cored for Cl^-

Figure 4.37. Photo. Exposed surface of specimen number 3-CCON-BB-2 after 377 days.

Figure 4.38. Photo. Traces of the upper three rebars and heavy corrosion products (specimen number 3-CCON-BB-1).

Figure 4.39. Photo. Trace of the upper rebars and heavy corrosion products on specimen number 1-STD1-BB-3.

analyses, as evidenced by the two core holes that are seen in the figure. In both cases, considerable corrosion product buildup is apparent.

Slabs Reinforced With MMFX-II™ Bars

Figures 4.40 and 4.41 show potential and macro-cell current density results, respectively, for the STD1 MMFX-II™ bar slabs in comparison to the black bar slabs (figures 4.32 and 4.33). The initial potential decrease was similar for both bar types; however, this does not necessarily mean that time-to-corrosion was the same since different reinforcement types may have different potential criterion for activation. Current density, once corrosion initiated, was less for the MMFX-II™ reinforcement compared to black bar by about a factor of five (figure 4.41). This is consistent with potential of the MMFX-II™ bars having remained more positive that the black bars thereby resulting is reduced driving force for current flow. Likewise, figures 4.42 and 4.43 show similar plots for MMFX-II™ reinforced STD2 concrete specimens in comparison to the STD1 ones. These reveal more positive potentials and lower current densities for the lower w/c concrete (STD2) compared to the higher (STD1). Figures 4.44 through 4.55 show potential and macro-cell current density plots for specimens with, respectively, black bar cathode (BCAT), wire brushed bars (WB), top bar crevice or splice (CREV), cracked concrete (CCON), cracked concrete and crevice (CCRV), and cracked concrete and black bar cathode (CCNB). The effect of each of these factors on corrosion initiation and propagation is summarized in figure 4.56 which plots potential versus macro-cell current density for a single specimen in each category. As noted above for the comparable black bar specimens (figure 4.36), the data conform to a common trend, albeit with scatter, with data for the cracked concrete specimens (CCON and CCNB) generally falling in the relatively negative potential—high current density regime (similar to the comparable black bar specimens). Macro-cell current density data for the wire brushed bar specimens are generally less than for the other MMFX-II™ specimen types (see also figure 4.45).

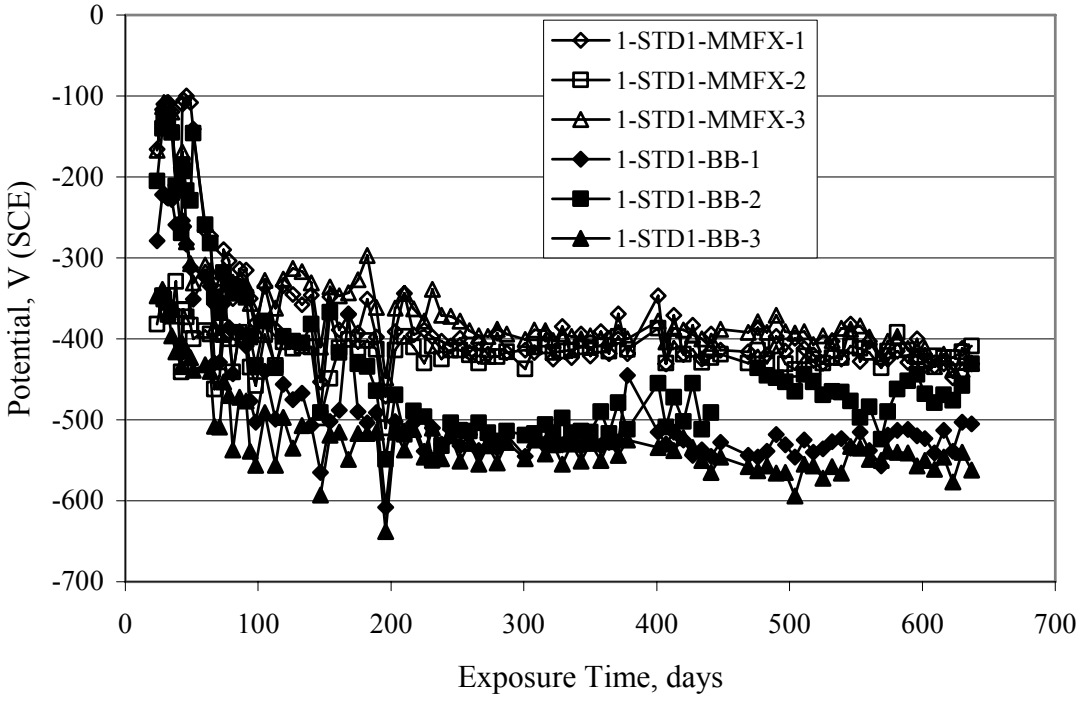

Figure 4.40. Graph. Plot of potential versus exposure time for STD1 concrete specimens with MMFX-II™ reinforcement in comparison to black bar results.

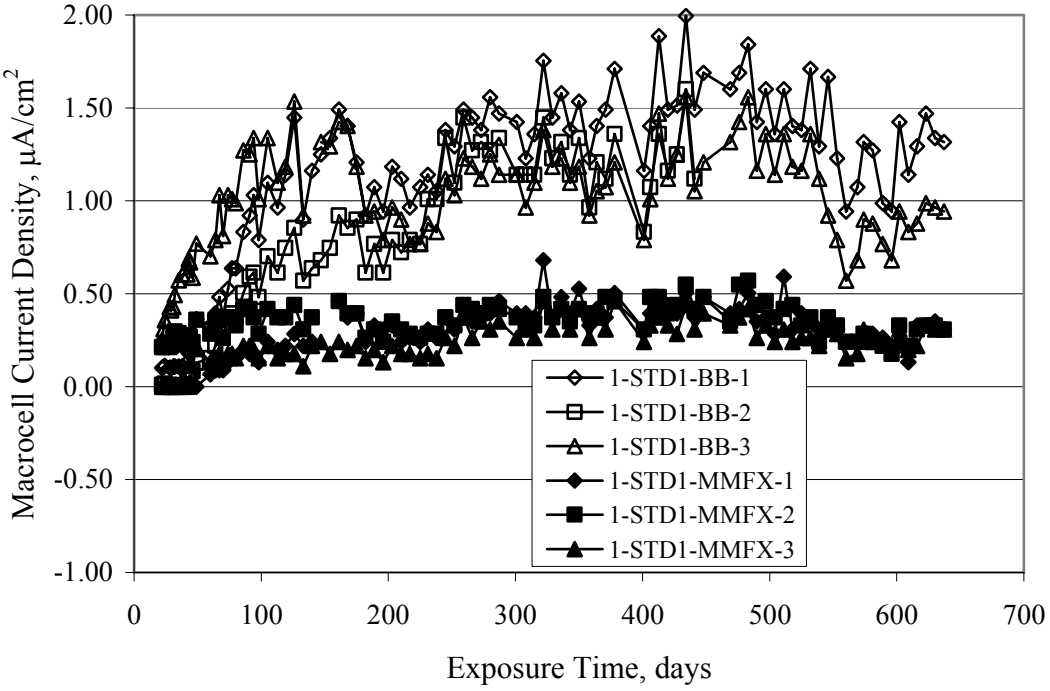

Figure 4.41. Graph. Plot of macro-cell current density versus exposure time for STD1 concrete specimens with MMFX-II™ reinforcement in comparison to black bar results.

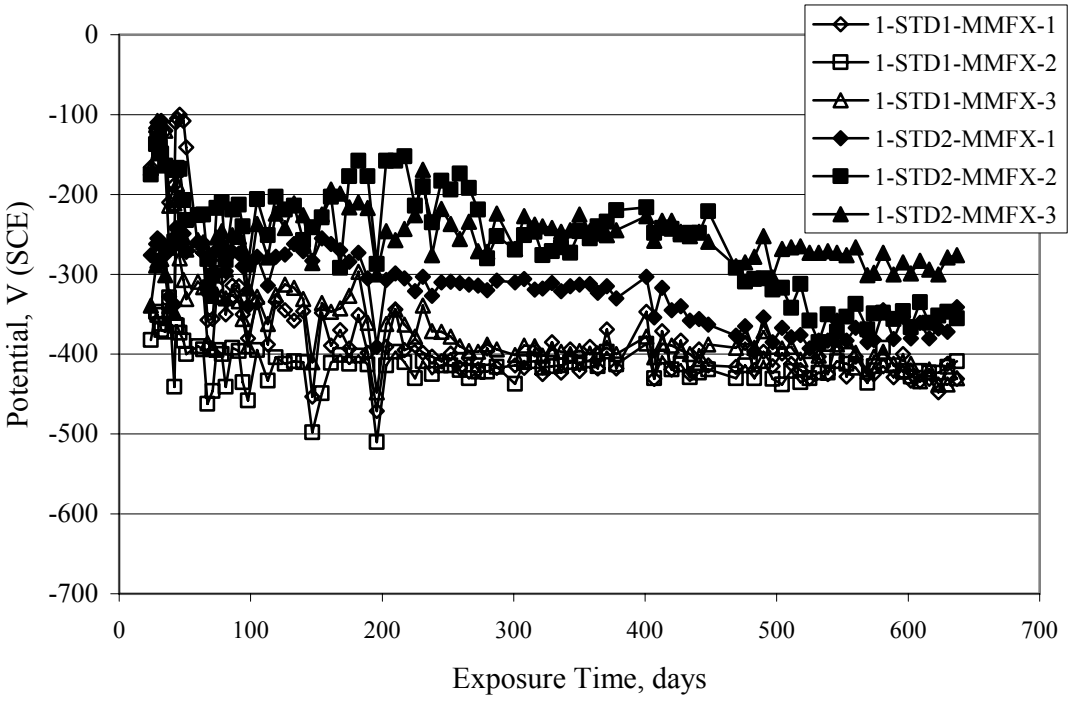

Figure 4.42. Graph. Plot of potential versus exposure time for STD1 and STD2 concrete specimens with MMFX-II™ reinforcement.

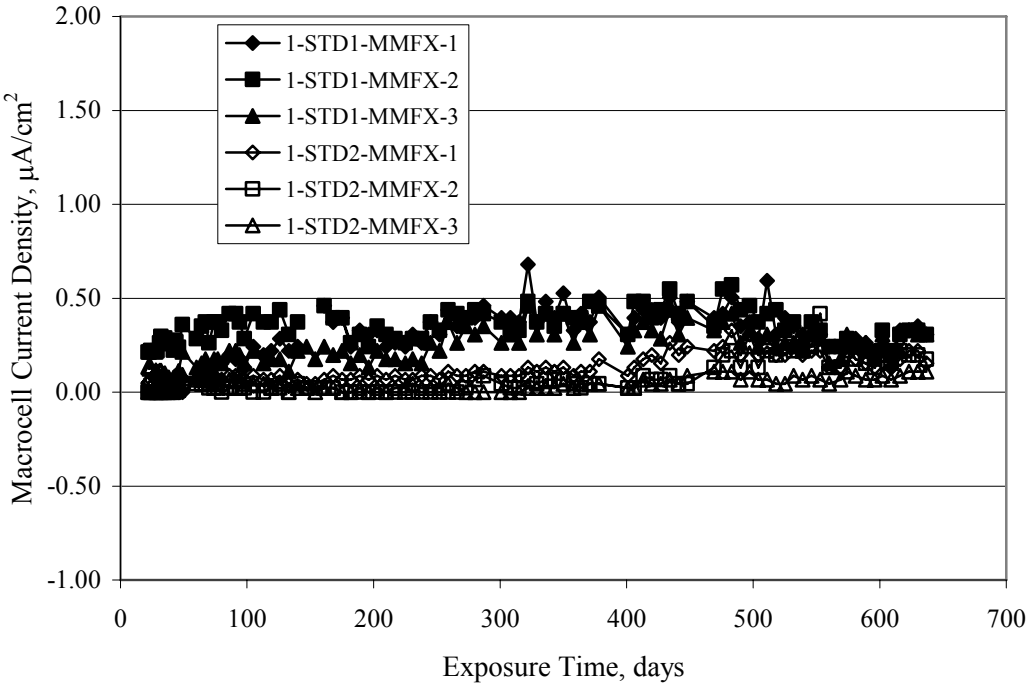

Figure 4.43. Graph. Plot of macro-cell current density versus exposure time for STD1 and STD2 concrete specimens with MMFX-II™ reinforcement.

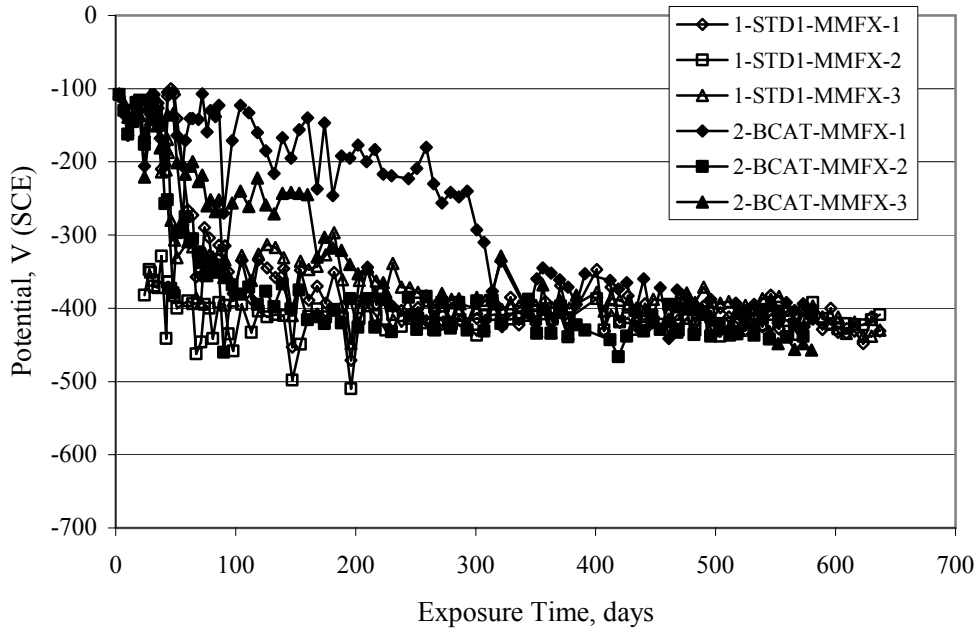

Figure 4.44. Graph. Plot of potential versus exposure time for STD1 concrete specimens with black bar bottom mat and top mat MMFX-II™ reinforcement compared to ones with all MMFX-II™ bars.

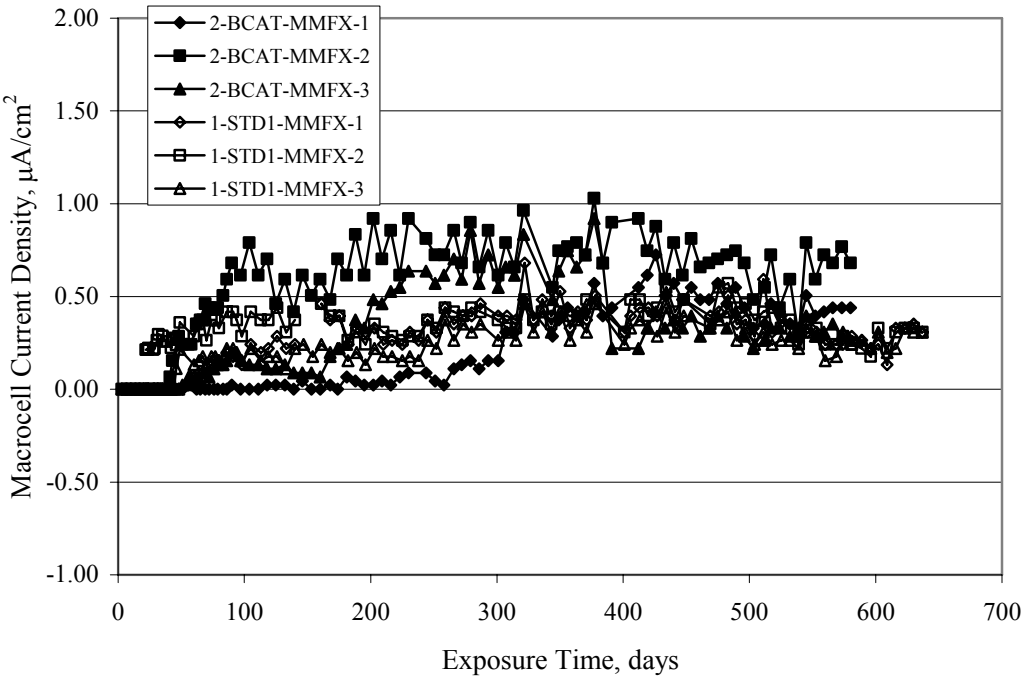

Figure 4.45. Graph. Plot of macro-cell current density versus exposure time for STD1 concrete specimens with black bar bottom mat and top mat MMFX-II™ reinforcement compared to ones with all MMFX-II™ bars.

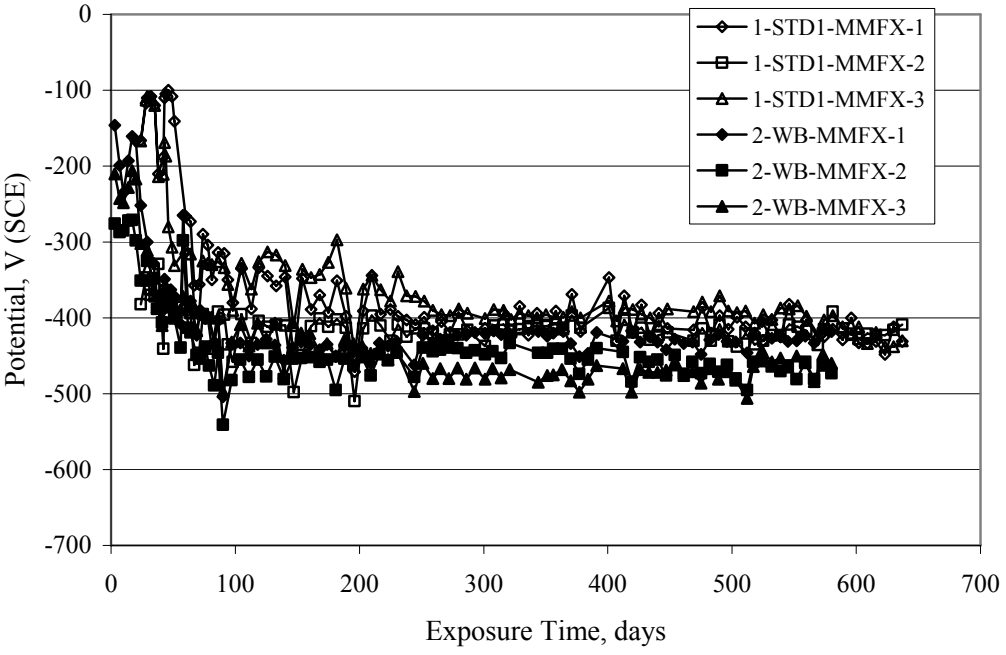

Figure 4.46. Graph. Plot of potential versus exposure time for STD1 concrete specimens with as-received and wire brushed (WB) MMFX-II™ reinforcement.

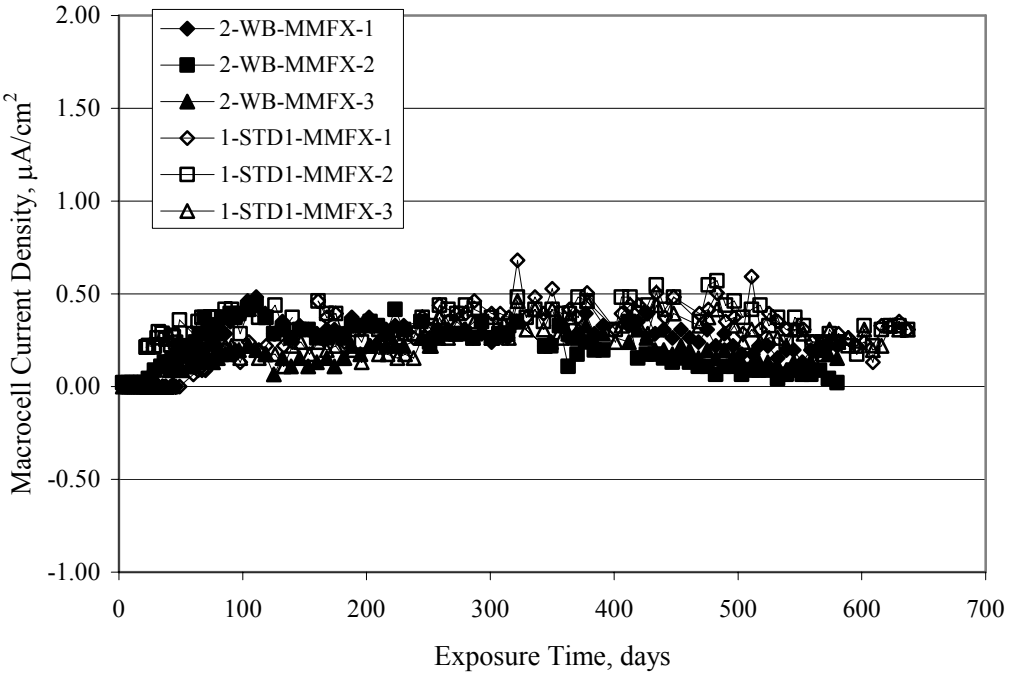

Figure 4.47. Graph. Plot of macro-cell current density versus exposure time for STD1 concrete specimens with as-received and wire brushed (WB) MMFX-II™ reinforcement.

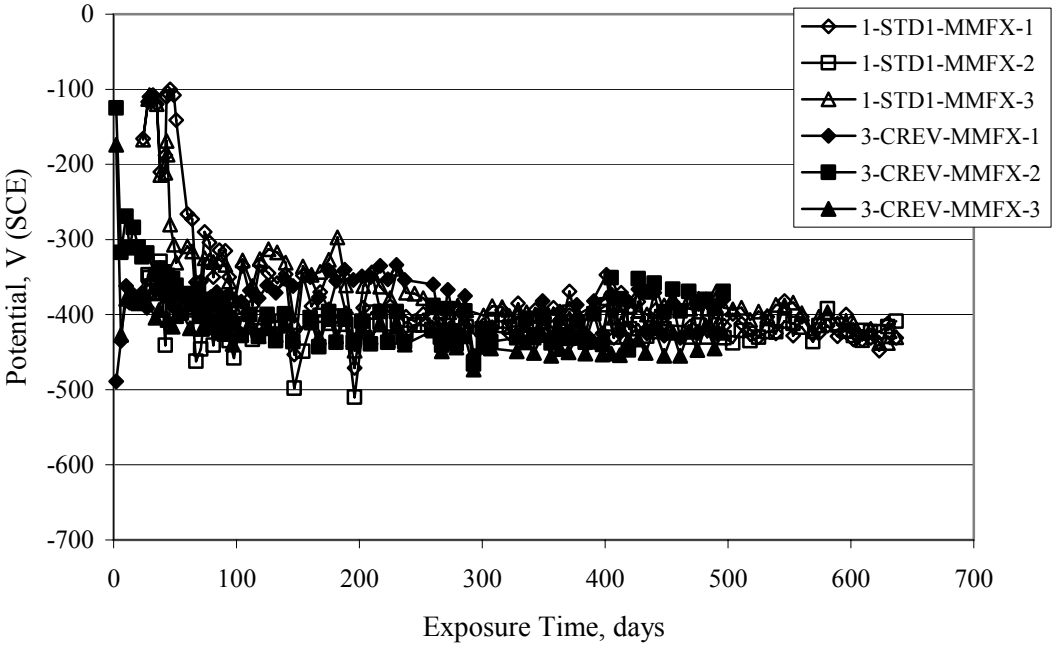

Figure 4.48. Graph. Plot of potential versus exposure time for STD1 concrete specimens with top mat crevice bars (splice) and MMFX-II™ reinforcement compared to ones with normal bar placement.

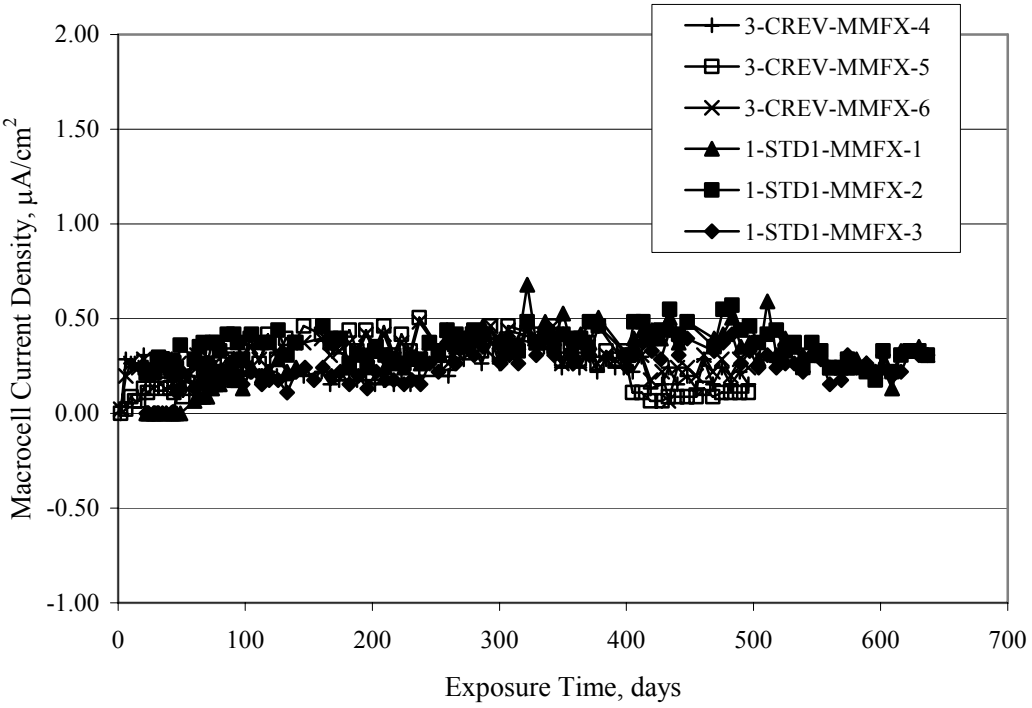

Figure 4.49. Graph. Plot of macro-cell current density versus exposure time for STD1 concrete specimens with top mat crevice bars (splice) and MMFX-II™ reinforcement.

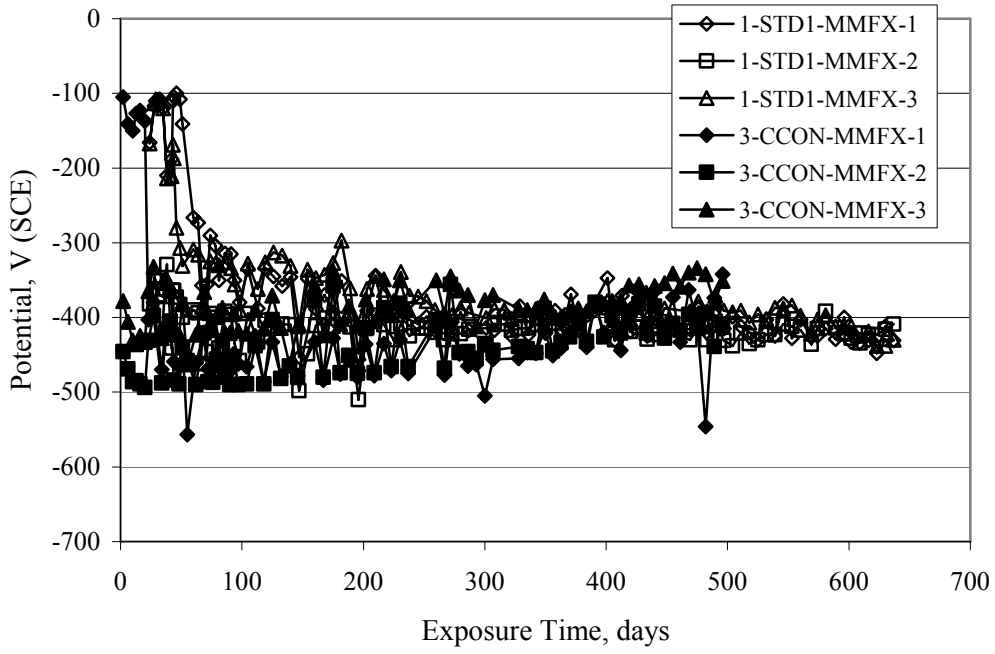

Figure 4.50. Graph. Plot of potential versus exposure time for STD1 concrete specimens with a simulated concrete crack and MMFX-II™ reinforcement compared to normal (uncracked) specimens.

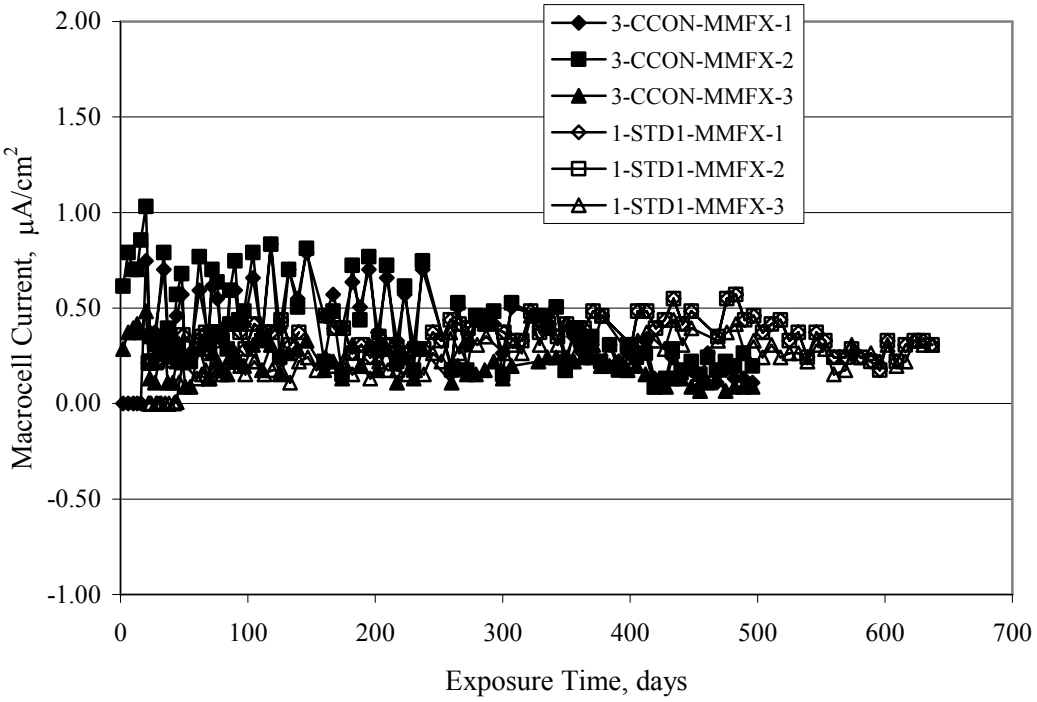

Figure 4.51. Graph. Plot of macro-cell current density versus exposure time for STD1 concrete specimens with a simulated concrete crack and MMFX-II™ reinforcement compared to normal (uncracked) specimens.

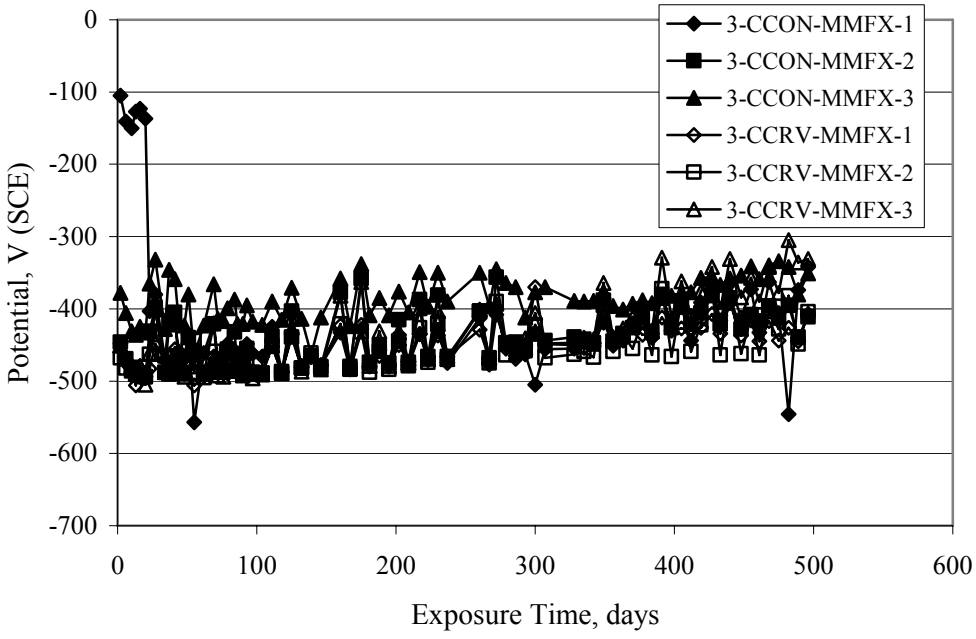

Figure 4.52. Graph. Plot of potential versus exposure time for STD1 concrete specimens with a simulated concrete crack and MMFX-II™ reinforcement compared to ones with a simulated crack and top bar crevice (splice).

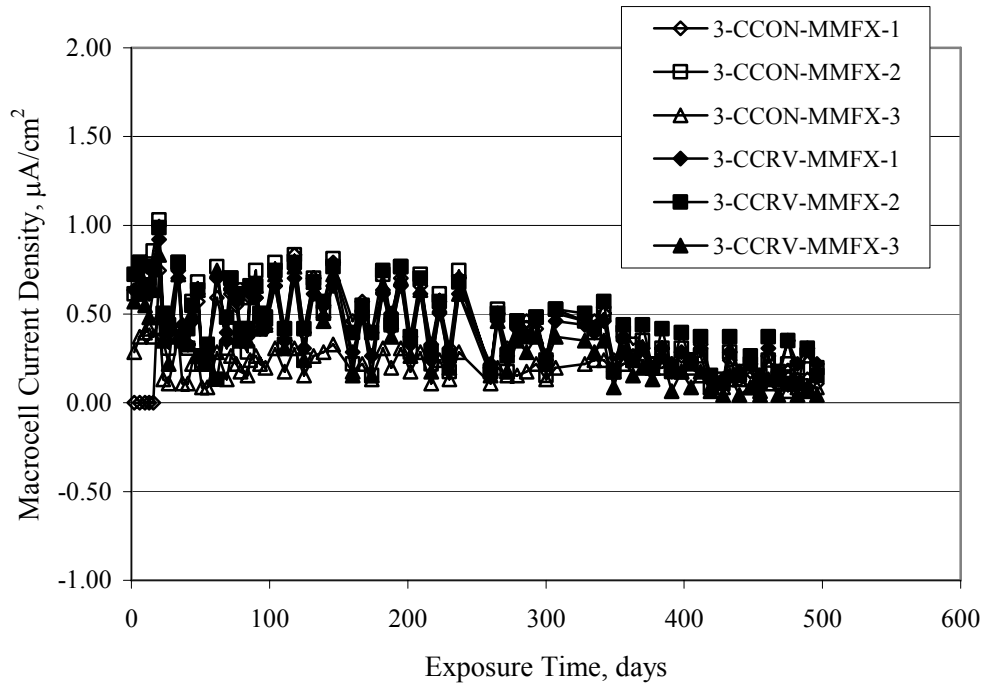

Figure 4.53. Graph. Plot of macro-cell current density versus exposure time for STD1 concrete specimens with a simulated concrete crack and MMFX-II™ reinforcement compared to ones with a simulated crack and top bar crevice (splice).

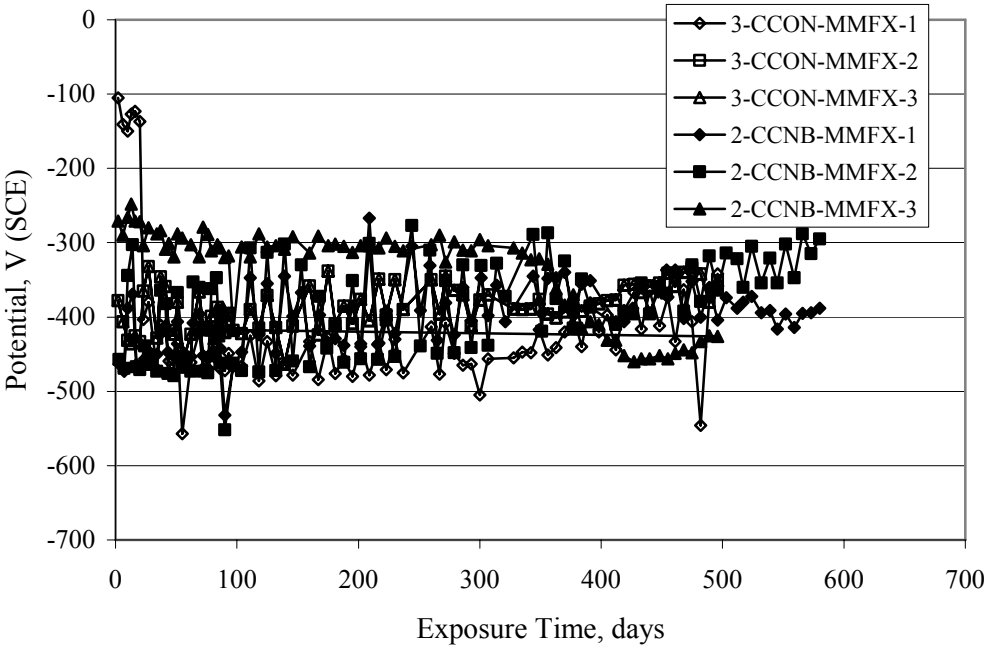

Figure 4.54. Graph. Plot of potential versus exposure time for STD1 concrete specimens with a simulated concrete crack and MMFX-II™ reinforcement compared to ones with a simulated crack and black bottom bars.

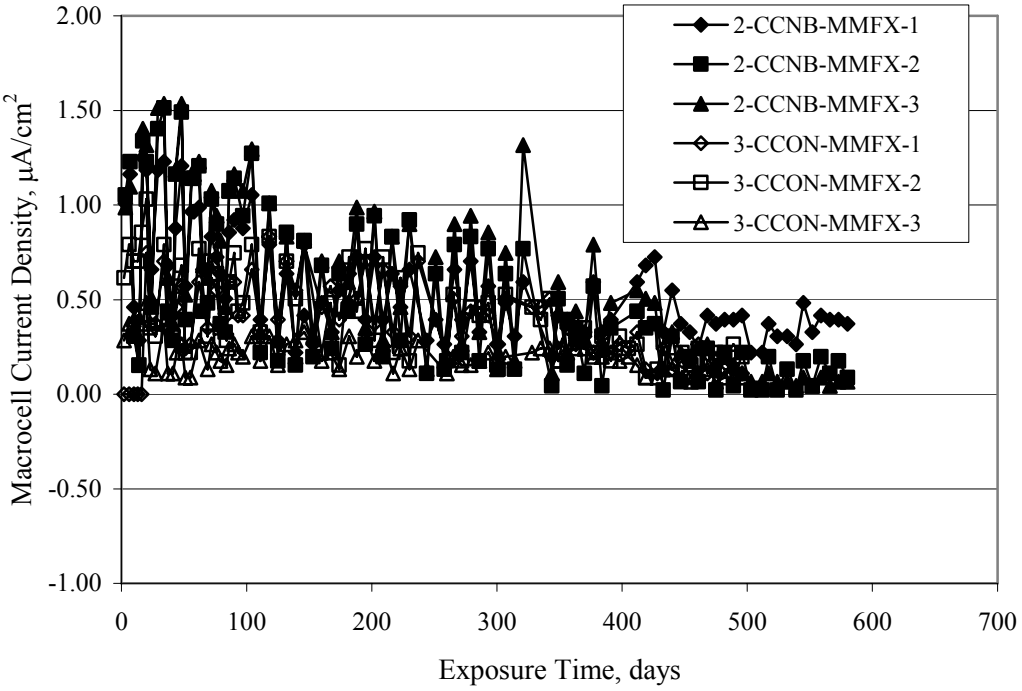

Figure 4.55. Graph. Plot of macro-cell current density versus exposure time for STD1 concrete specimens with a simulated concrete crack and MMFX-II™ reinforcement compared to ones with a simulated crack and black bar bottom mat.

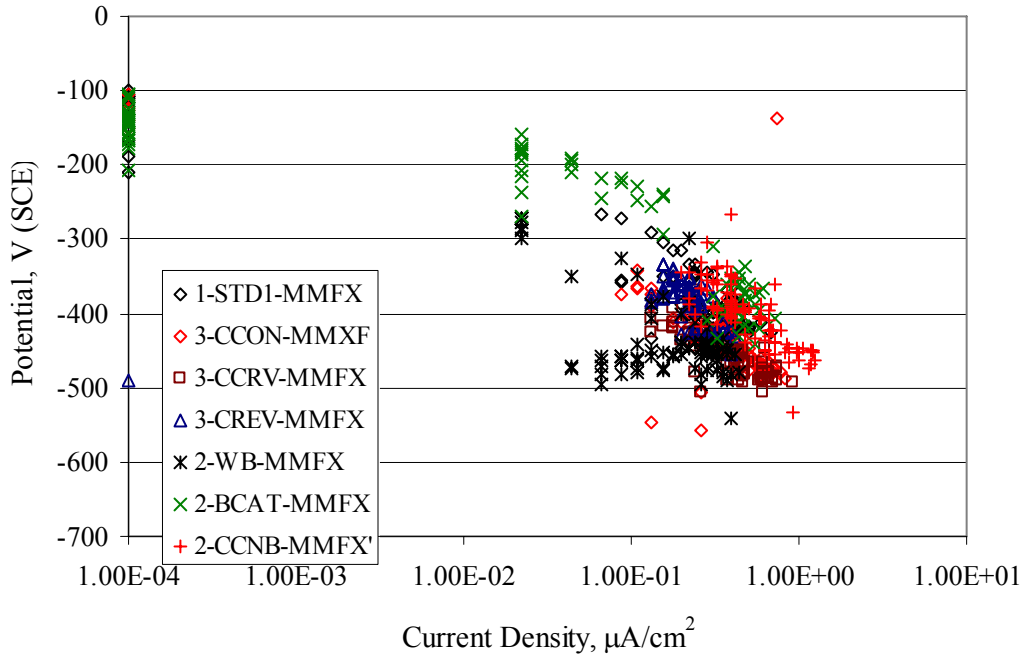

Figure 4.56. Graph. Plot of potential versus macro-cell current density for MMFX-II™ reinforced specimens.

Figure 4.57 shows a photograph that was taken of the exposed surface of a MMFX-II™ specimen (specimen number 2-BCAT-MMFX-3) during the dry phase of the ponding cycle after 461 days. The surface is rust stained, and the concrete has cracked above one of the three bars. Likewise, Figures 4.58 through 4.65 show the appearance of the upper bar traces for one specimen each of the STD1, STD2, WB, CREV, CCON, BCAT, CCNB, and CCRV configurations. Because specimens were exposed at three different times but autopsied at the same time, the exposure time varied (566 to 707 days). Irrespective of this, a visual comparison of the standard STD1 and CCON black bar (figures 4.39 and 4.38, respectively) and companion MMFX-II™ specimens (figures 4.62 and 4.58, respectively) reveals considerably less corrosion for the latter, consistent with the corresponding current density data as discussed above. The visual extent of the corrosion products (figures 4.58 through 4.65) is generally consistent with magnitude of the long-term current density (higher current density, more corrosion). Bar traces on the autopsied MMFX-II™ BCAT specimen exhibited the greatest amount of corrosion product and had the highest current density at long-term. With the exception of the BCAT specimens, current density of the three specimen set of each type exhibited relatively little scatter.

Figure 4.57. Photo. Top surface of specimen 2-BCAT-MMFX-3 after 461 days of exposure.

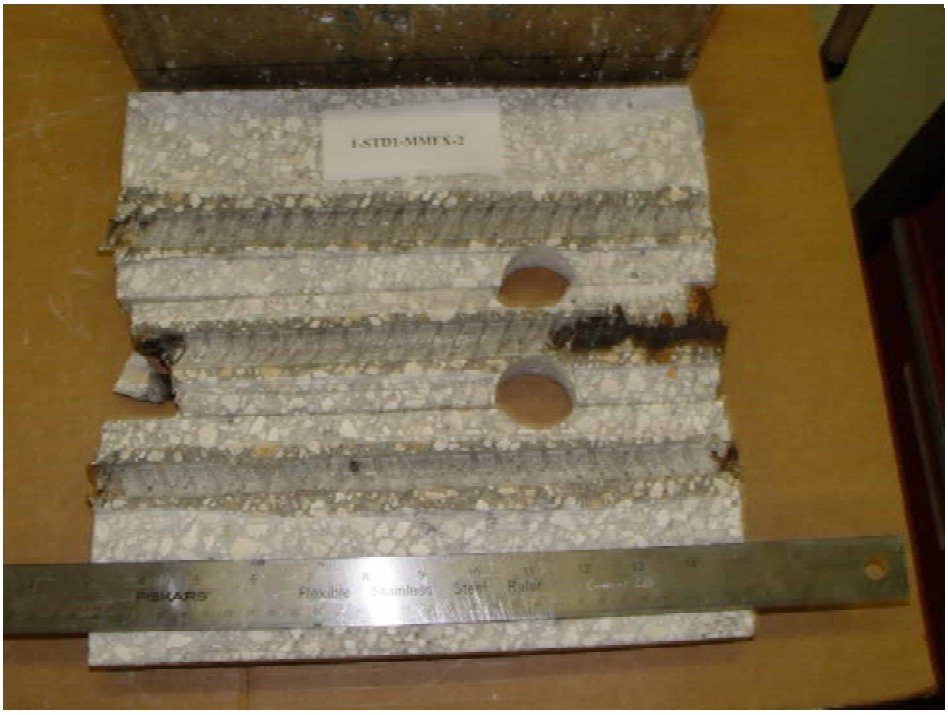

Figure 4.58. Photo. Trace of the upper rebars and corrosion products on specimen number 1-STD1-MMFX-2.

Figure 4.59. Photo. Trace of the upper rebars and corrosion products on specimen number 1-STD2-MMFX-2.

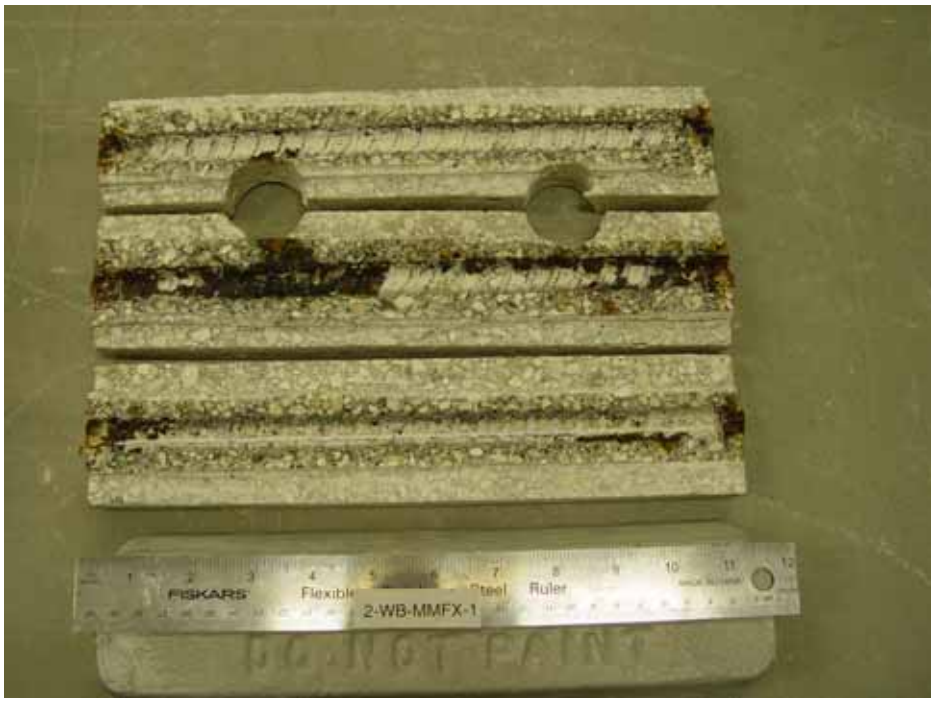

Figure 4.60. Photo. Trace of the upper rebars and corrosion products on specimen number 2-WB-MMFX-1.

Figure 4.61. Photo. Trace of the upper rebars and corrosion products on specimen number 3-CREV-MMFX-1.

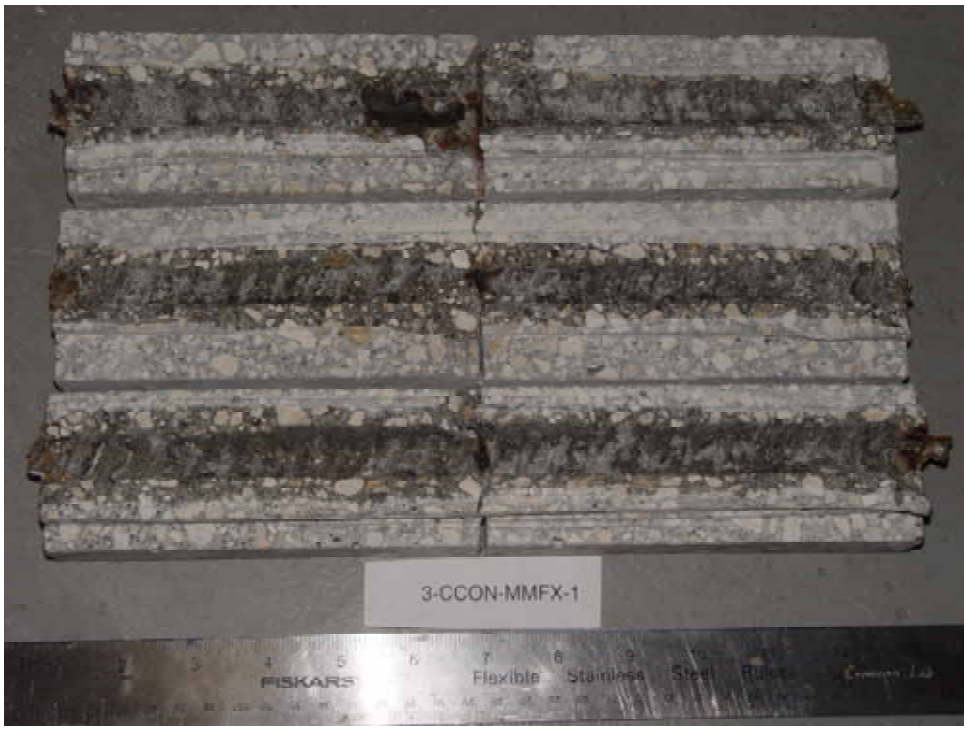

Figure 4.62. Photo. Trace of the upper rebars and corrosion products on specimen number 1-CCON-MMFX-1.

Figure 4.63. Photo. Trace of the upper rebars and corrosion products on specimen number 2-BCAT-MMFX-1.

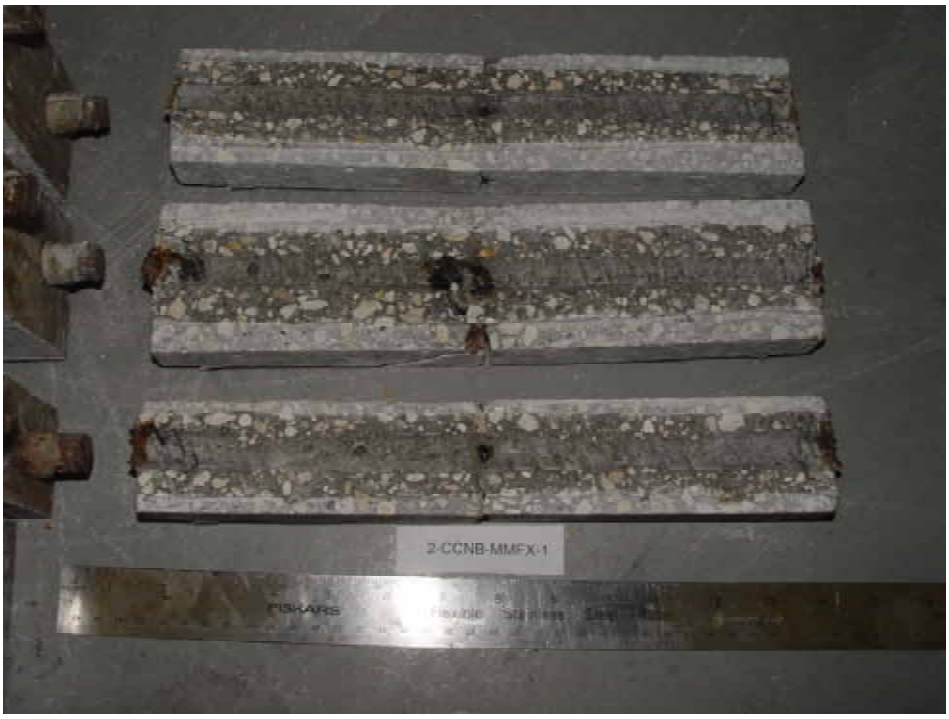

Figure 4.64. Photo. Trace of the upper rebars and corrosion products on specimen number 2-CCNB-MMFX-1.

Figure 4.65. Photo. Trace of the upper rebars and corrosion products on specimen number 3-CCRV-MMFX-1.

Slabs Reinforced With 3Cr12 Bars

Figures 4.66 through 4.79 present potential and macro-cell current density plots for specimens reinforced with 3Cr12.[2] For the standard STD1 specimens (figures 4.66 and 4.67), the corresponding black bar data are shown for comparison; and these reveal that, while the initial potential decay was approximately the same for the two reinforcements, macro-cell current density for the 3Cr12 reinforcement, once corrosion initiated, increased more gradually and to a steady-state value about three times lower than for the black bar specimens. Figure 4.80 shows a plot of potential versus macro-cell current density for specimens reinforced with 3Cr12 that includes representative data for each of the specimen types. As for the black bar and MMFX-II specimens, a common data band is apparent; however, in this case the band is more narrow and largely limited to a potential-current density regime rather than extending from upper left to lower right. The highest current densities occurred for specimens with concrete cracks (CCON and CCRV); however, this occurred also in the case for the black bar cathode (BCAT) specimens.

Photographs of the upper bar traces of autopsied specimens are shown in figures 4.81 through 4.87. These indicate that specimens STD1, STD2, CREV, and BCAT exhibited relatively heavy localized corrosion products on one bar compared to the WB, CCON, and CCRV specimens for which corrosion was relatively light. As for the MMFX-II™ specimens, the appearance of the corrosion products is in general agreement with the long-term current density data (higher current density greater corrosion products).

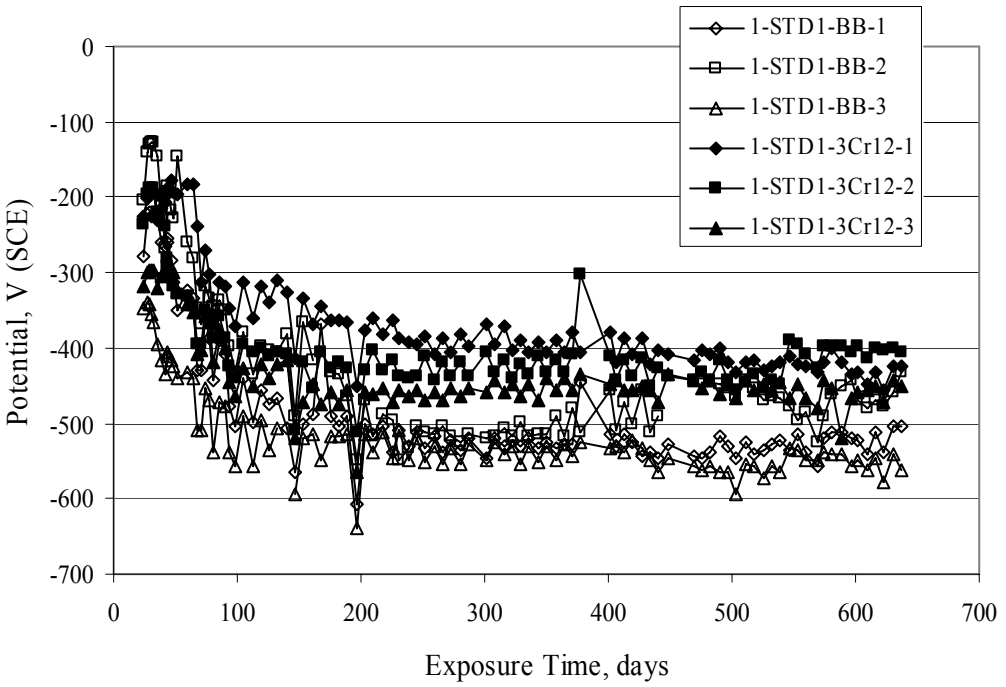

Figure 4.66. Graph. Plot of potential versus exposure time for STD1 concrete specimens with 3Cr12 reinforcement compared to that for black bar.

[2] Due to an error during specimen fabrication, six BCAT and no CCNB specimens with this reinforcement were prepared.

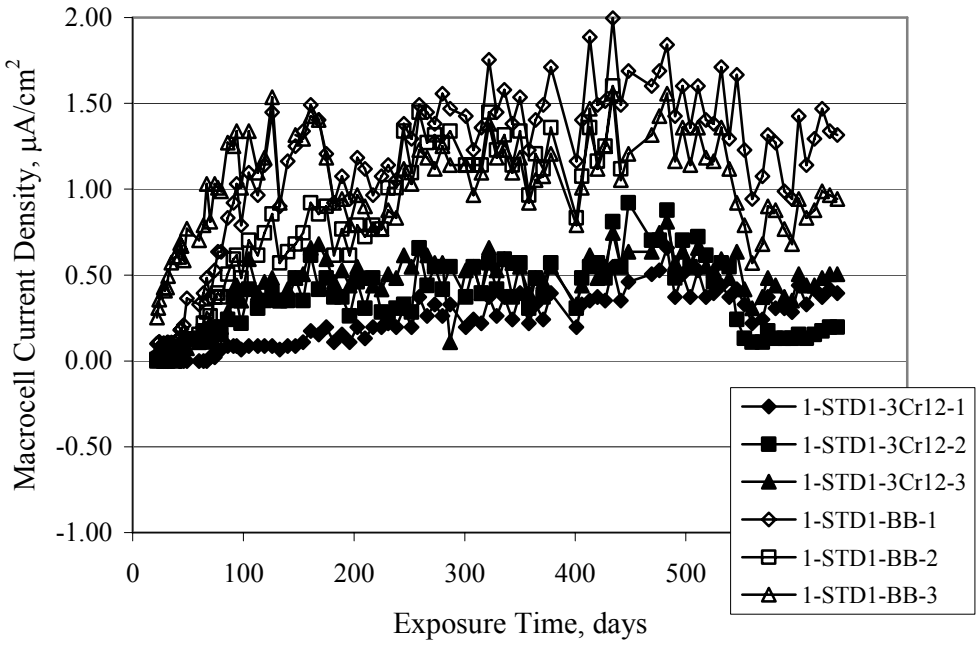

Figure 4.67. Graph. Plot of macro-cell current density versus exposure time for STD1 concrete specimens with 3Cr12 reinforcement compared to that for black bar.

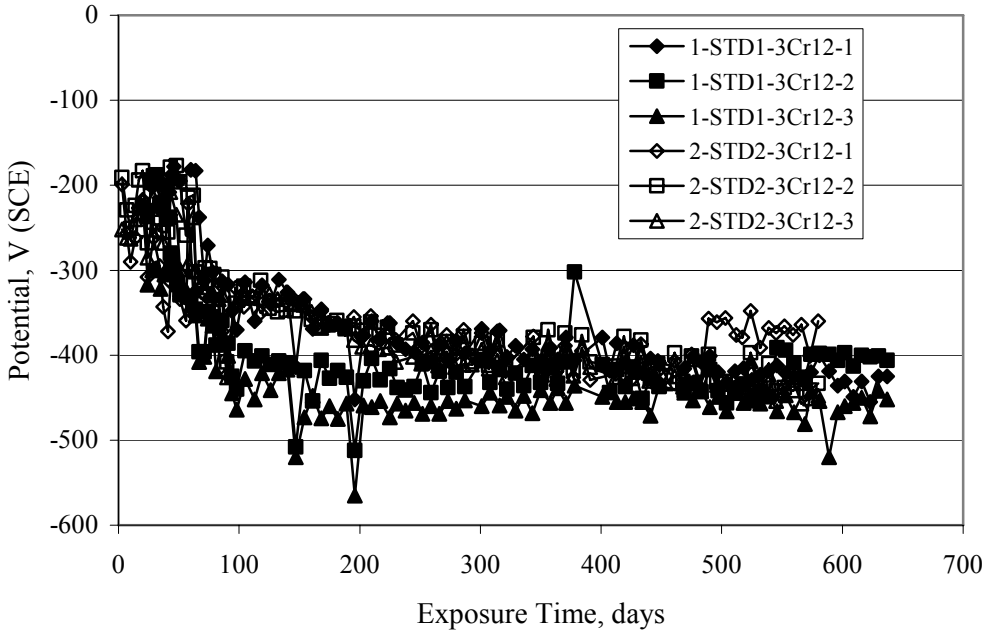

Figure 4.68. Graph. Plot of potential versus exposure time for STD1 and STD2 concrete specimens with 3Cr12 reinforcement.

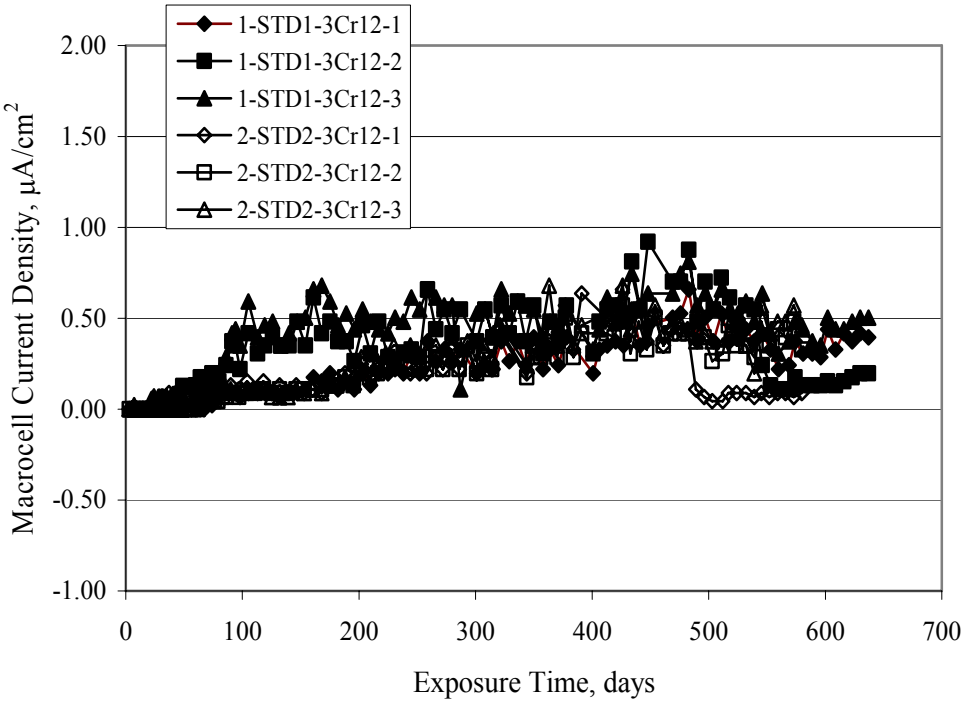

Figure 4.69. Graph. Plot of macro-cell current density versus exposure time for STD1 and STD2 concrete specimens with 3Cr12 reinforcement.

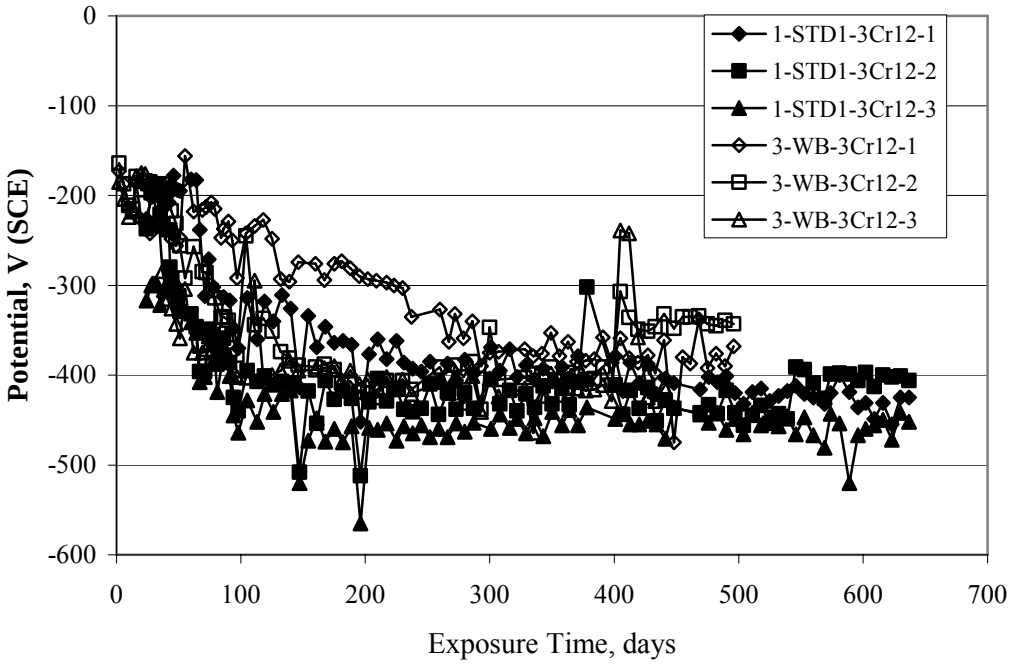

Figure 4.70. Graph. Plot of potential versus exposure time for STD1 concrete specimens with wire brushed compared to as-received 3Cr12 bars.

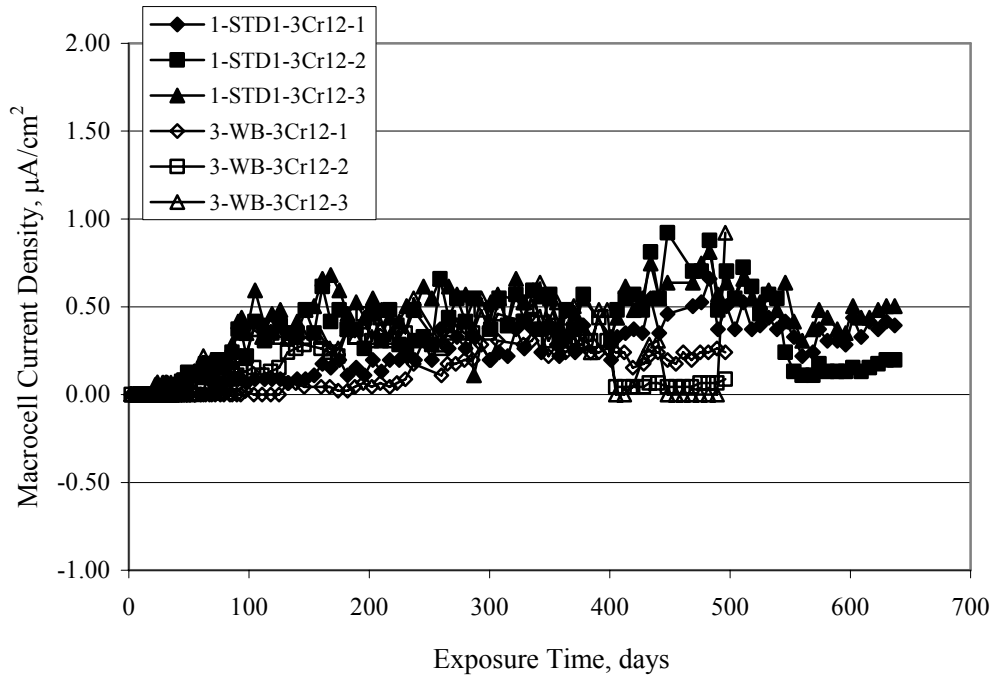

Figure 4.71. Graph. Plot of macro-cell current density versus exposure time for STD1 concrete specimens with wire brushed compared to as-received 3Cr12 bars.

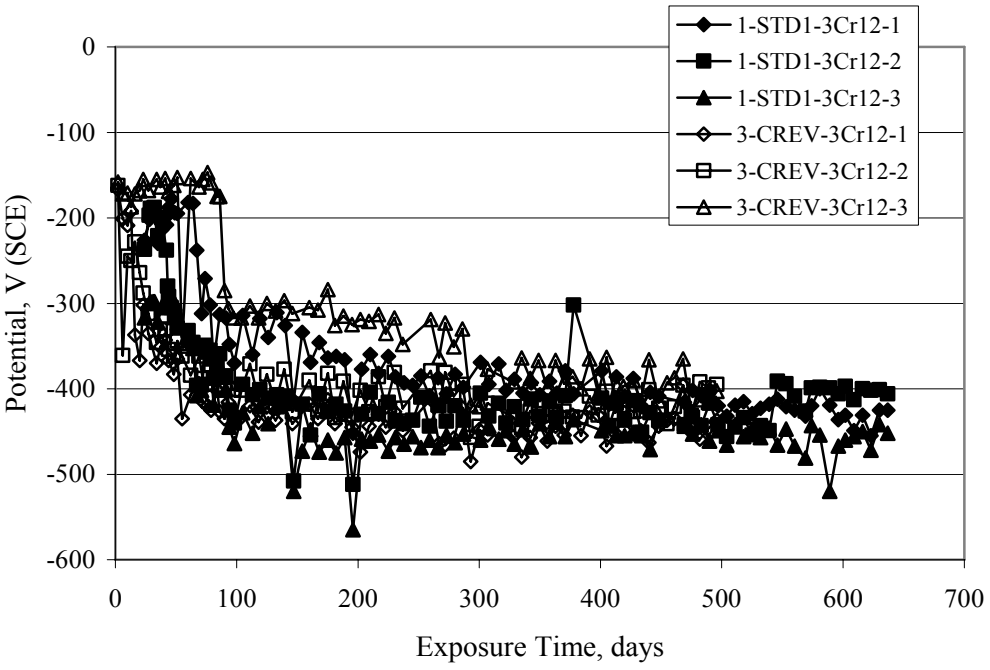

Figure 4.72. Graph. Plot of potential versus exposure time for STD1 concrete specimens with top mat bar crevice (splice) and 3Cr12 reinforcement compared to ones with normal bar placement.

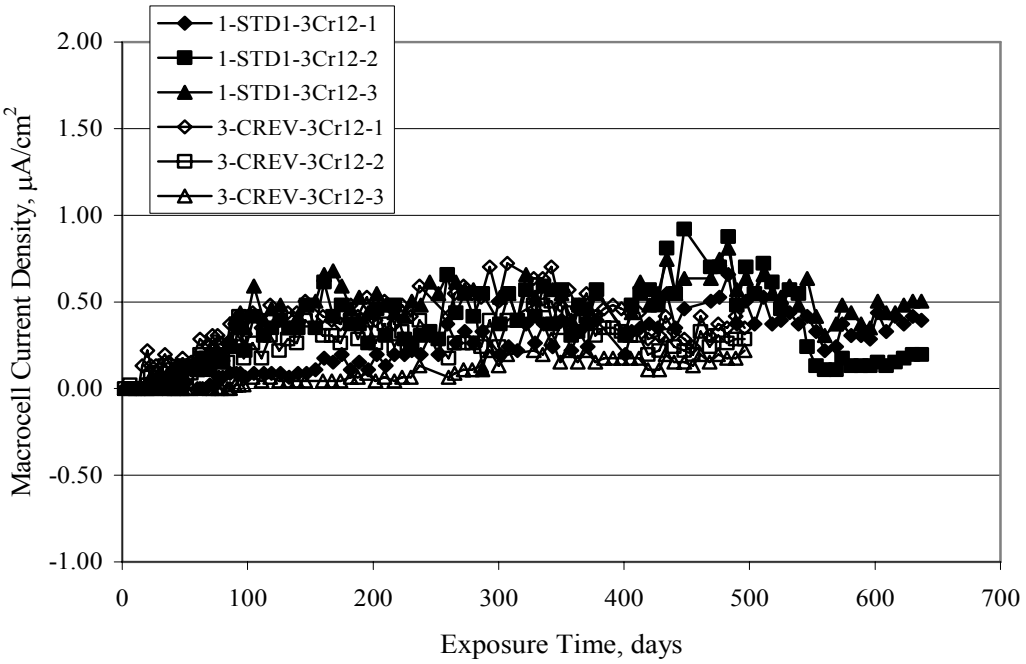

Figure 4.73. Graph. Plot of macro-cell current density versus exposure time for STD1 concrete specimens with top mat bar crevice (splice) and 3Cr12 reinforcement compared to ones with normal bar placement.

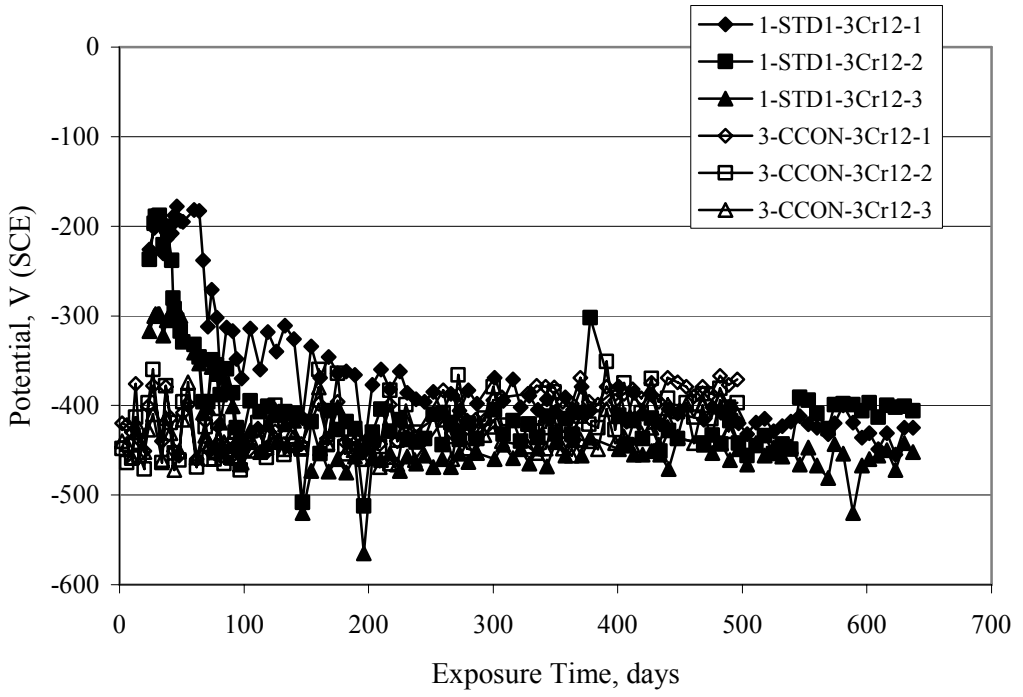

Figure 4.74. Graph. Plot of potential versus exposure time for STD1 concrete specimens with a simulated concrete crack and 3Cr12 reinforcement compared to uncracked ones.

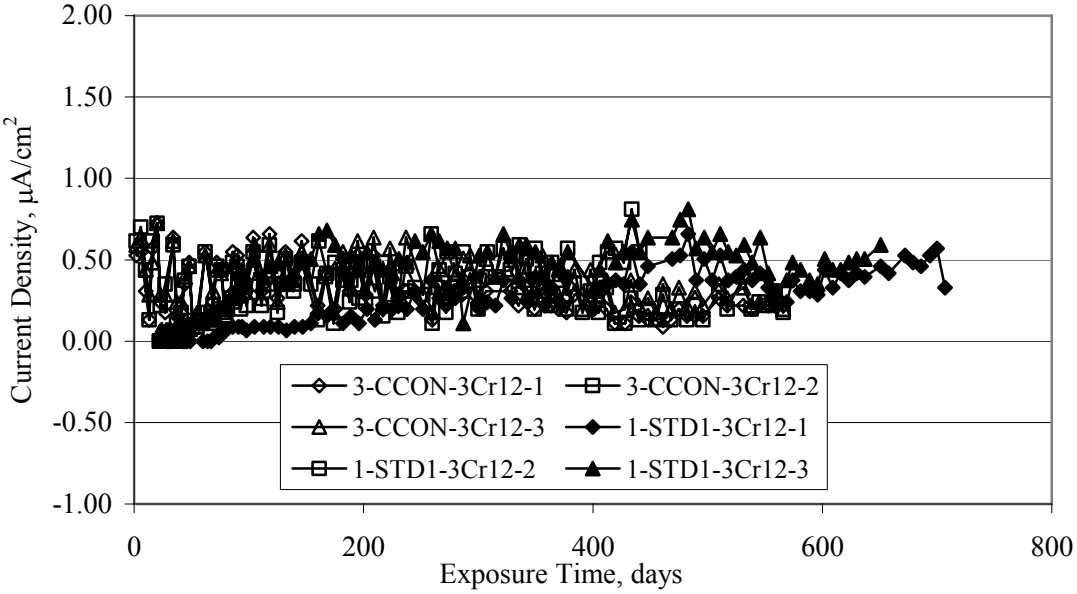

Figure 4.75. Graph. Plot of macro-cell current density versus exposure time for STD1 concrete specimens with a simulated concrete crack and 3Cr12 reinforcement compared to uncracked ones.

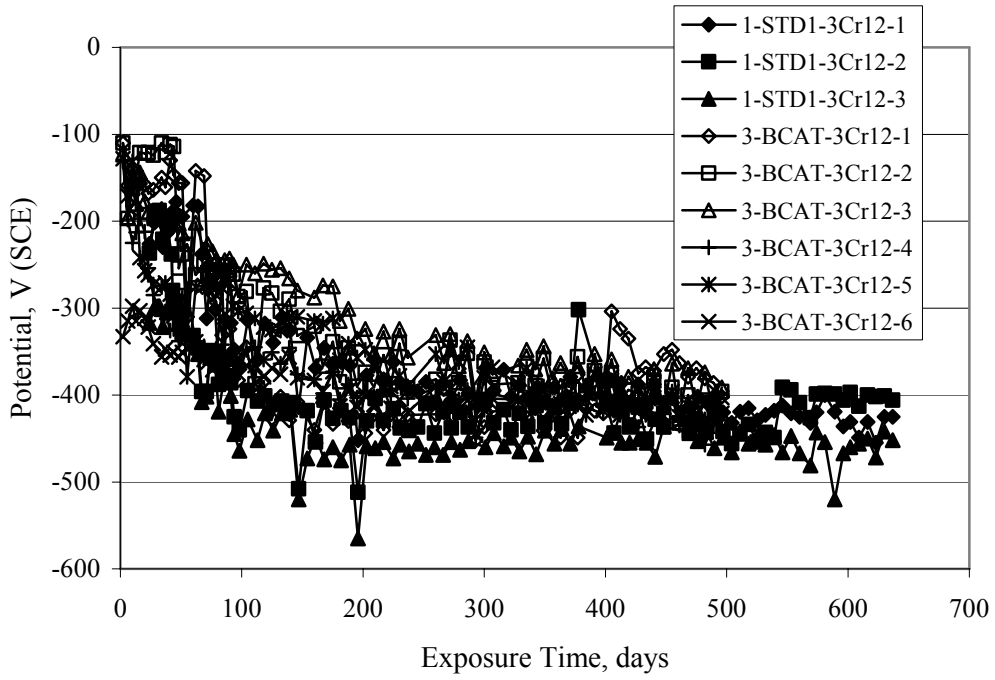

Figure 4.76. Graph. Plot of potential versus exposure time for STD1 concrete specimens with black bar bottom mat and top mat 3Cr12 reinforcement compared to ones with all 3Cr12 bars.

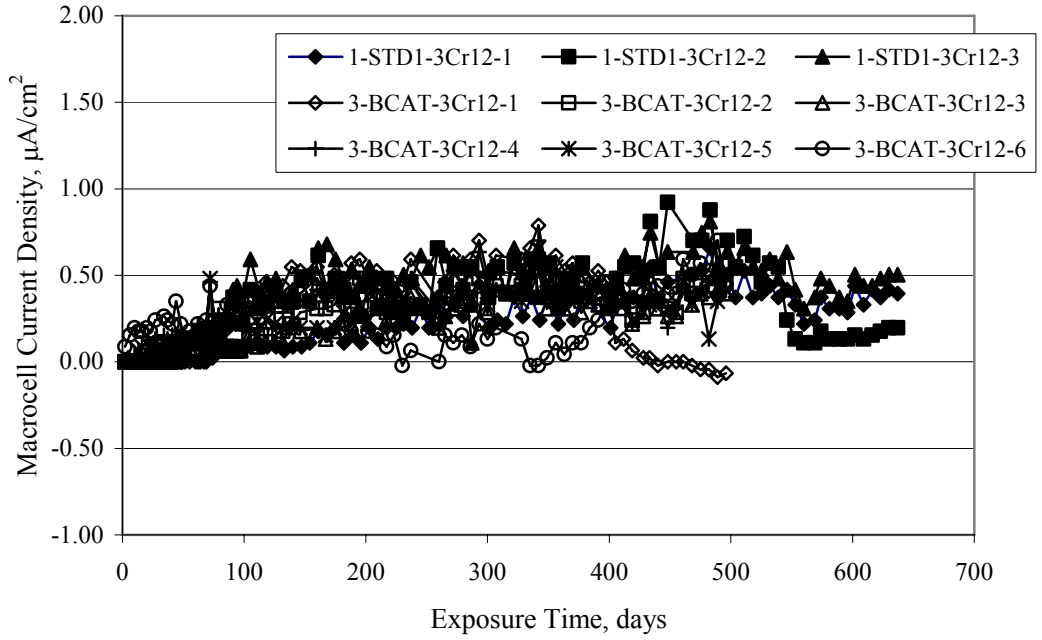

Figure 4.77. Graph. Plot of macro-cell current density versus exposure time for STD1 concrete specimens with black bar bottom mat and top mat 3Cr12 reinforcement compared to ones with all 3Cr12 bars.

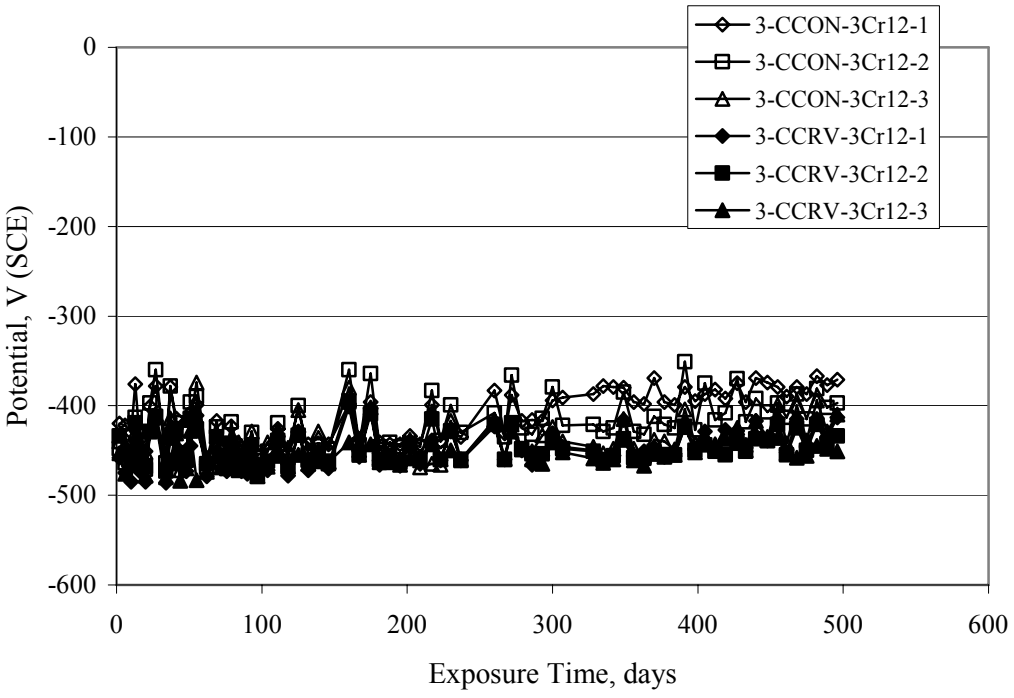

Figure 4.78. Graph. Plot of potential versus exposure time for STD1 concrete specimens with a simulated concrete crack and 3Cr12 reinforcement compared to cracked ones with a simulated crack and top bar crevice (splice).

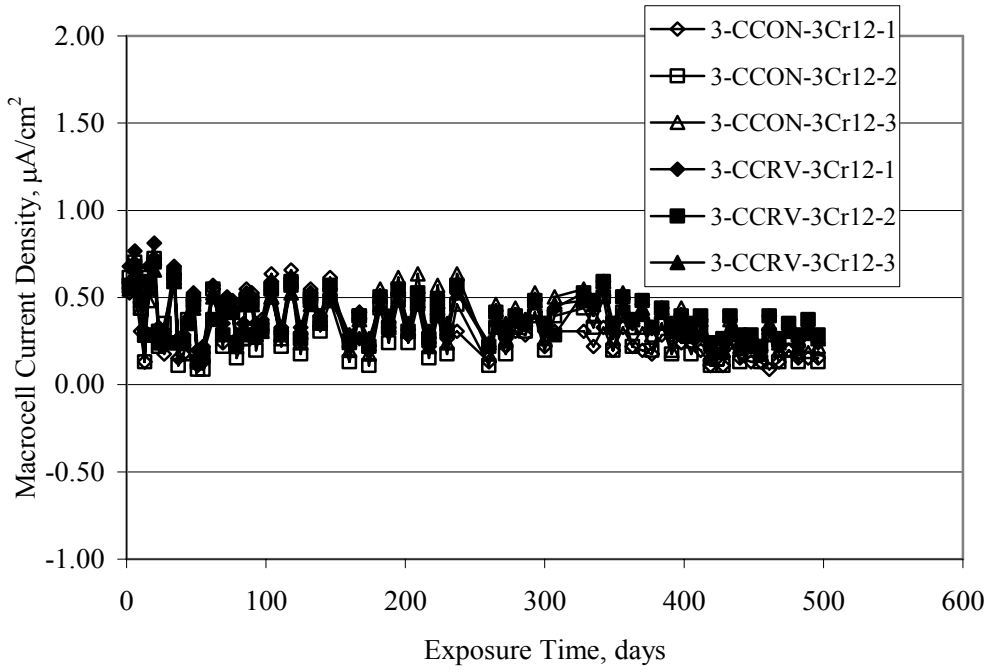

Figure 4.79. Graph. Plot of macro-cell current density versus exposure time for STD1 concrete specimens with a simulated concrete crack and 3Cr12 reinforcement compared to cracked ones with a simulated crack and top bar crevice (splice).

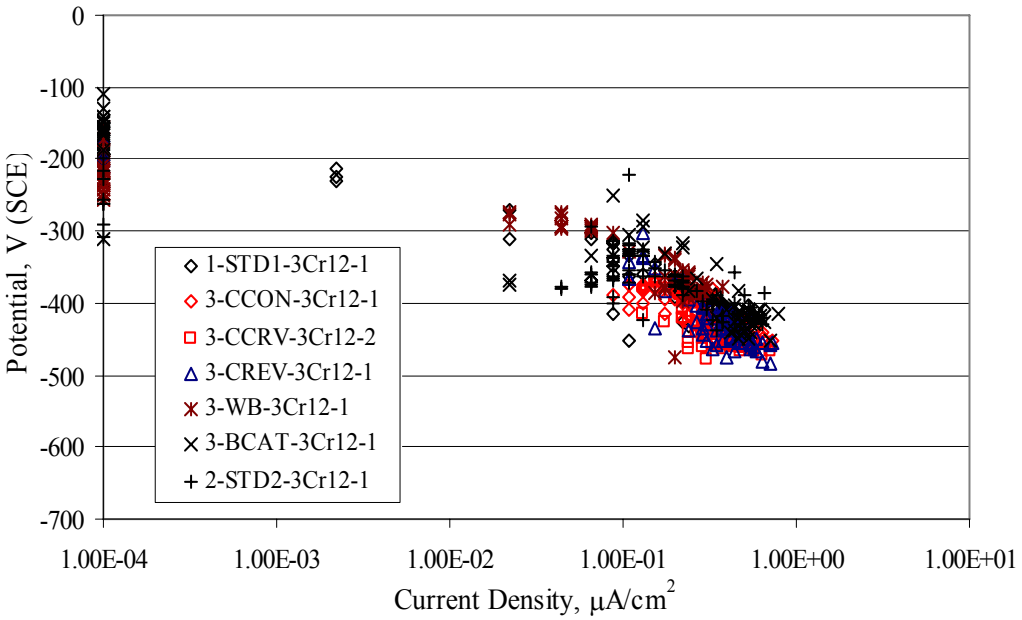

Figure 4.80. Graph. Plot of potential versus macro-cell current density for 3Cr12 reinforced specimens.

Figure 4.81. Photo. Trace of the upper rebars and corrosion products on specimen number 1-STD1-3Cr12-1.

Figure 4.82. Photo. Trace of the upper rebars and corrosion products on specimen number 1-STD2-3Cr12-1.

Figure 4.83. Photo. Trace of the upper rebars and corrosion products on specimen number 1-WB-3Cr12-1.

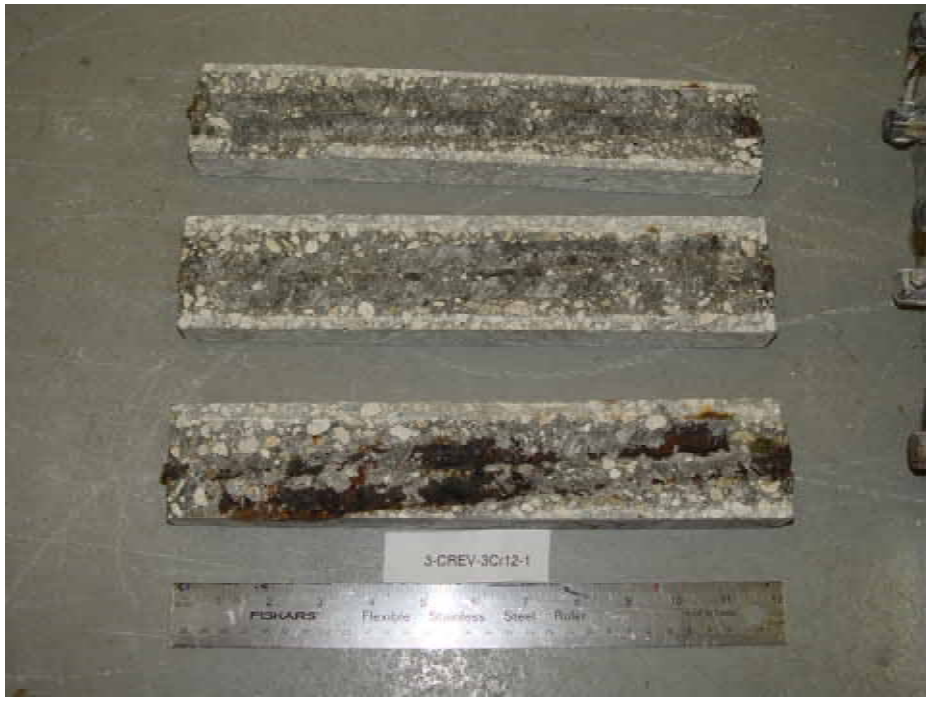

Figure 4.84. Photo. Trace of the upper rebars and corrosion products on specimen number 1-CREV-3Cr12-1.

Figure 4.85. Photo. Trace of the upper rebars and corrosion products on specimen number 1-CCON-3Cr12-1.

Figure 4.86. Photo. Trace of the upper rebars and corrosion products on specimen number 1-BCAT-3Cr12-1.

Figure 4.87. Photo. Trace of the upper rebars and corrosion products on specimen number 1-CCRV-3Cr12-1.

Slabs Reinforced With 2201 Bars

Figures 4.88 through 4.91 show potential and macro-cell current density plots for standard specimens reinforced with 2201. Here, the initial potential decay was more gradual than for the black bar specimens; and current density subsequent to initiation was less by a factor of 2 to 3. Figures 4.92 through 4.103 show plots for the other specimen variables. Figure 4.104 presents potential versus macro-cell current density data for specimens reinforced with 2201 that includes representative data for each of the specimen types. As for the other bar types, all data conform to a common trend but occupy different regimes therein. As such, the upper current densities of the trend band occurred for the crevice specimens (CCON and CCRV), whereas the wire brushed ones were at the lower bound. Some of the black cathode (BCAT) current densities occurred at values below the lower band bound. This apparently reflects the fact that potential remained relatively positive for one of the three specimens (see figure 4.98).

Figures 4.105 through 4.112 show photographs of the upper bar traces of autopsied specimens (one specimen from each group of three) for each of the specimen variables. These indicate that, more so than for the black bar, MMFX-II™, and 3Cr12, corrosion tended to initiate on the bars near the specimen side faces. Unlike the bar types evaluated above, corrosion products were more extensive on the STD2 than STD1 specimen (compare figures 4.105 and 4.106), which is inconsistent with the current density data (figure 4.91). The reason for this is unclear but may be related to the corrosion preferential attack at the bar ends. In addition to the STD2 specimen, products were extensive on at least one bar of the CREV, CCON, and BCAT specimens. Consequently, of the rebar types MMFX-II™, 3Cr12, and 2201, the autopsied CREV and BCAT specimens in each case exhibited heavy corrosion product accumulation on at least one of the three bars.

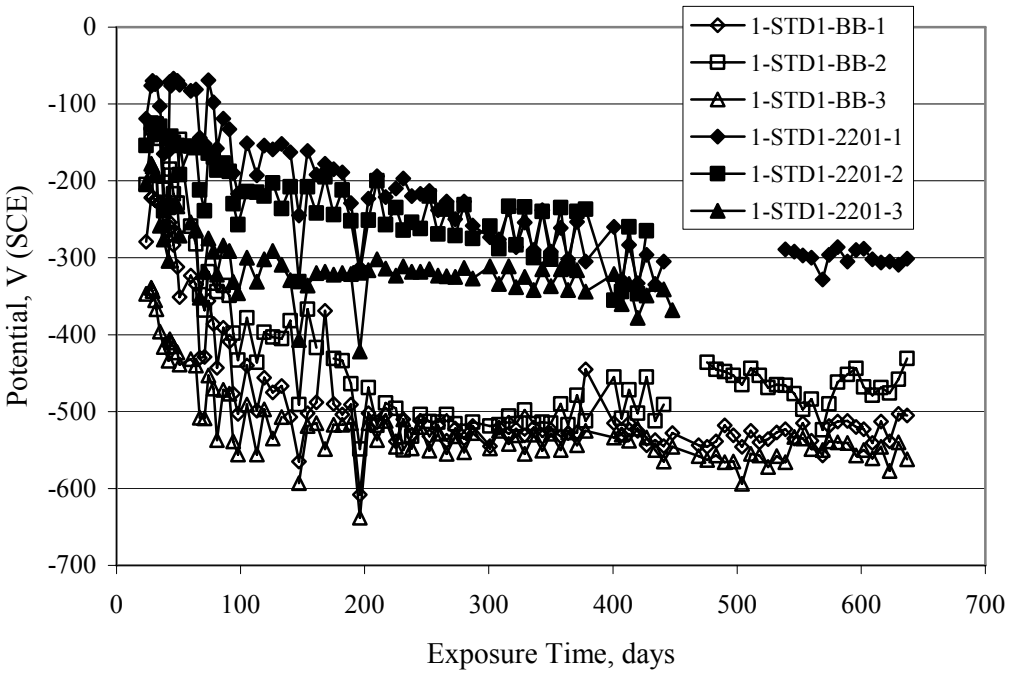

Figure 4.88. Graph. Plot of potential versus exposure time for STD1 concrete specimens with 2201 reinforcement compared to data for black bar.

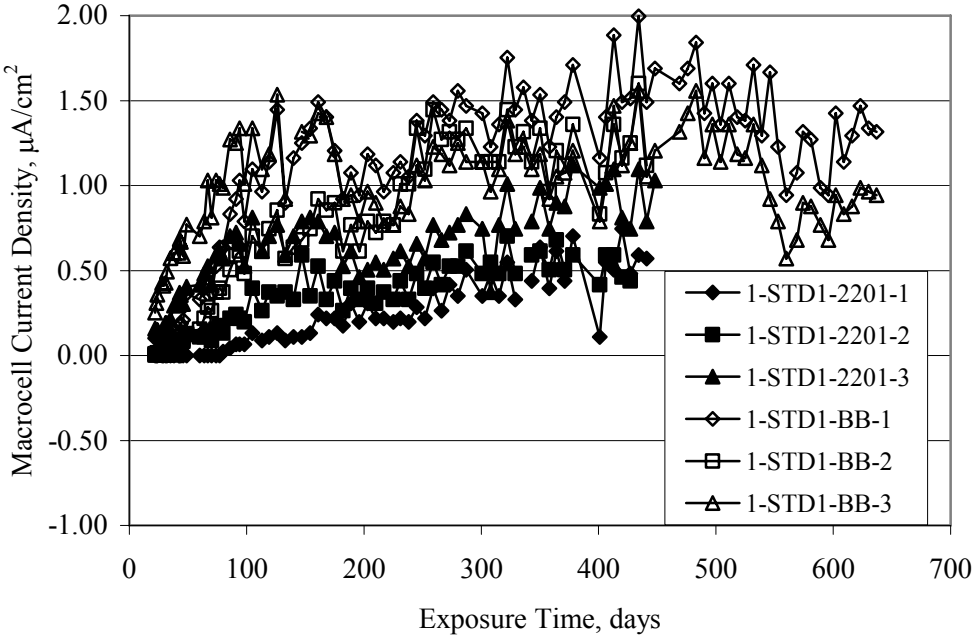

Figure 4.89. Graph. Plot of macro-cell current density versus exposure time for STD1 concrete specimens with 2201 reinforcement compared to data for black bar.

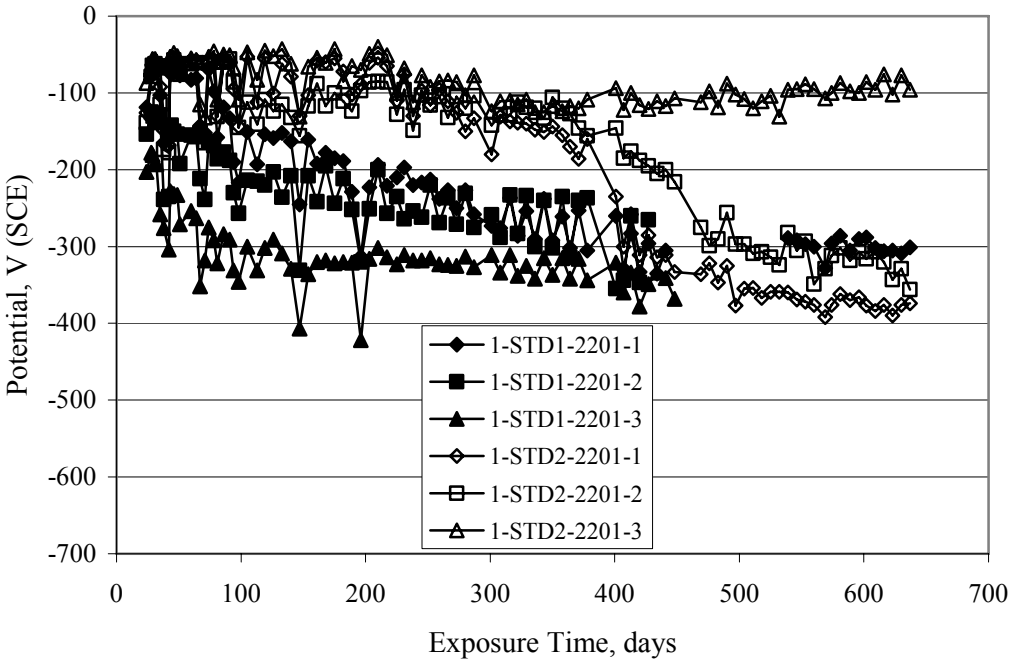

Figure 4.90. Graph. Plot of potential versus exposure time for STD1 and STD2 concrete specimens with 2201 reinforcement.

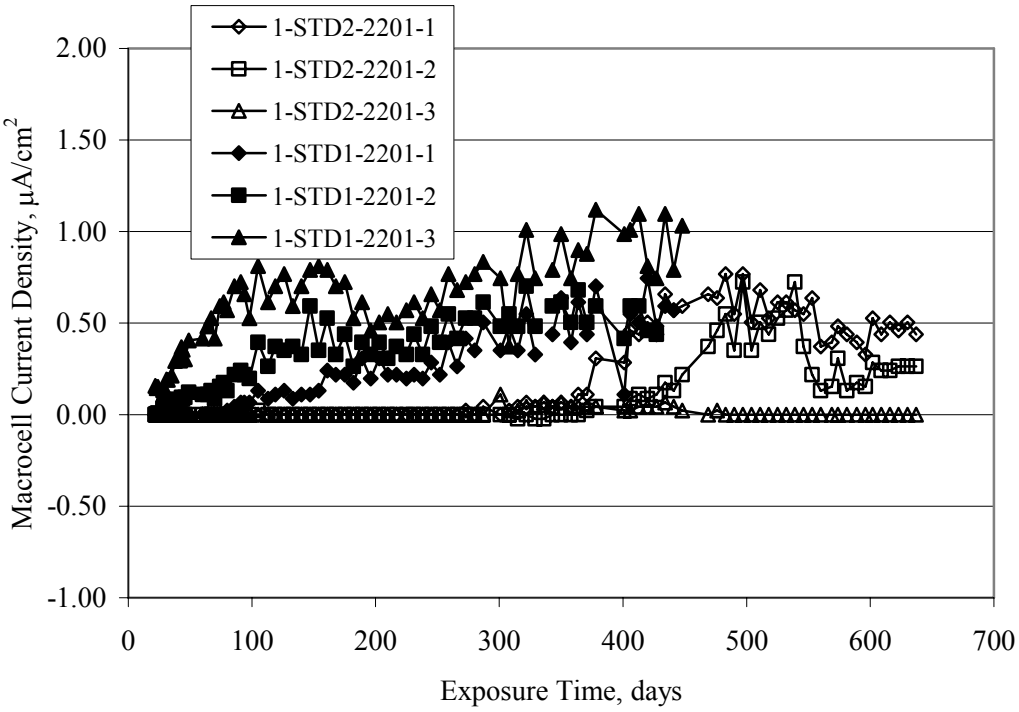

Figure 4.91. Graph. Plot of macro-cell current density versus exposure time for STD1 and STD2 concrete specimens with 2201 reinforcement.

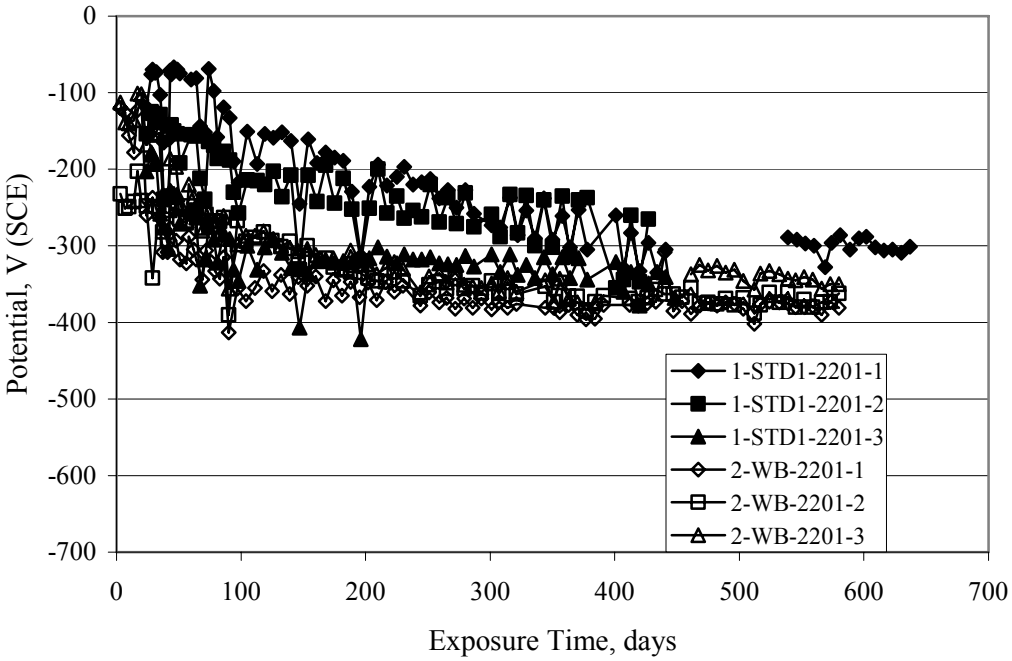

Figure 4.92. Graph. Plot of potential versus exposure time for STD1 concrete specimens with wire brushed (WB) 2201 bars compared to ones with as-received 2201 bars.

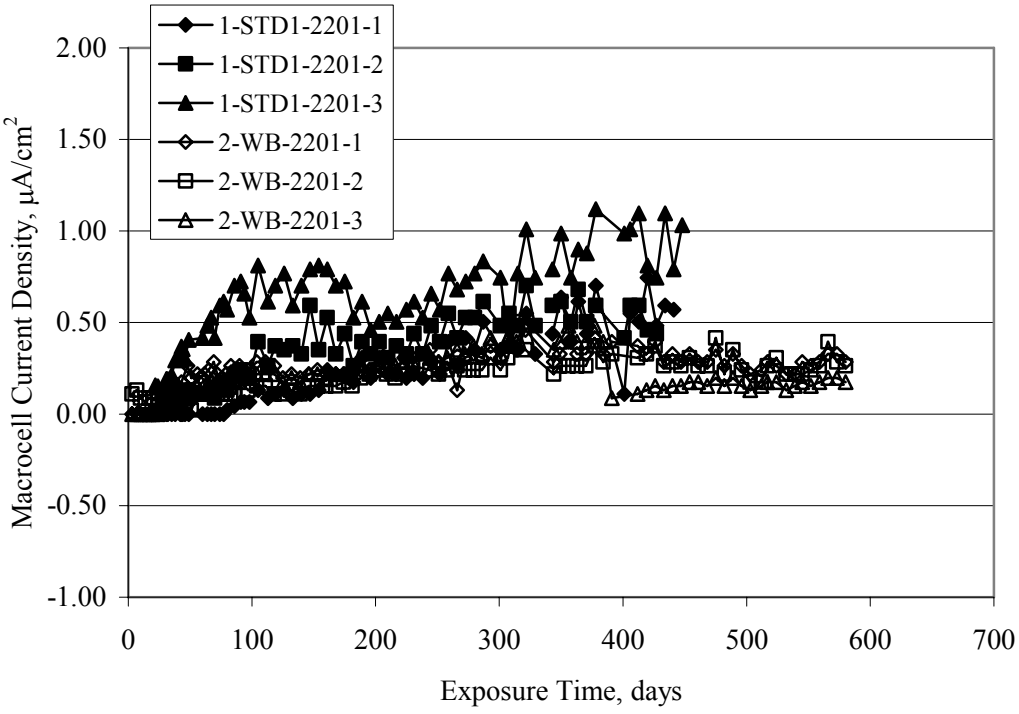

Figure 4.93. Graph. Plot of macro-cell current density versus exposure time for STD1 concrete specimens with wire brushed (WB) 2201 bars compared to ones with as-received 2201 bars.

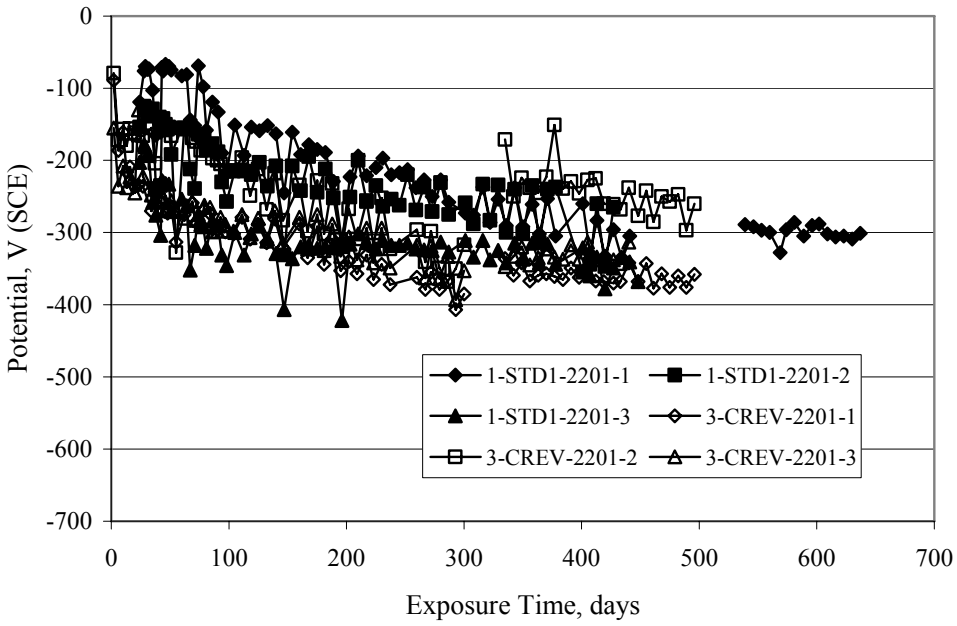

Figure 4.94. Graph. Plot of potential versus exposure time for STD1 concrete specimens with top mat crevice bars (splice) and 2201 reinforcement compared to ones with normal bar placement.

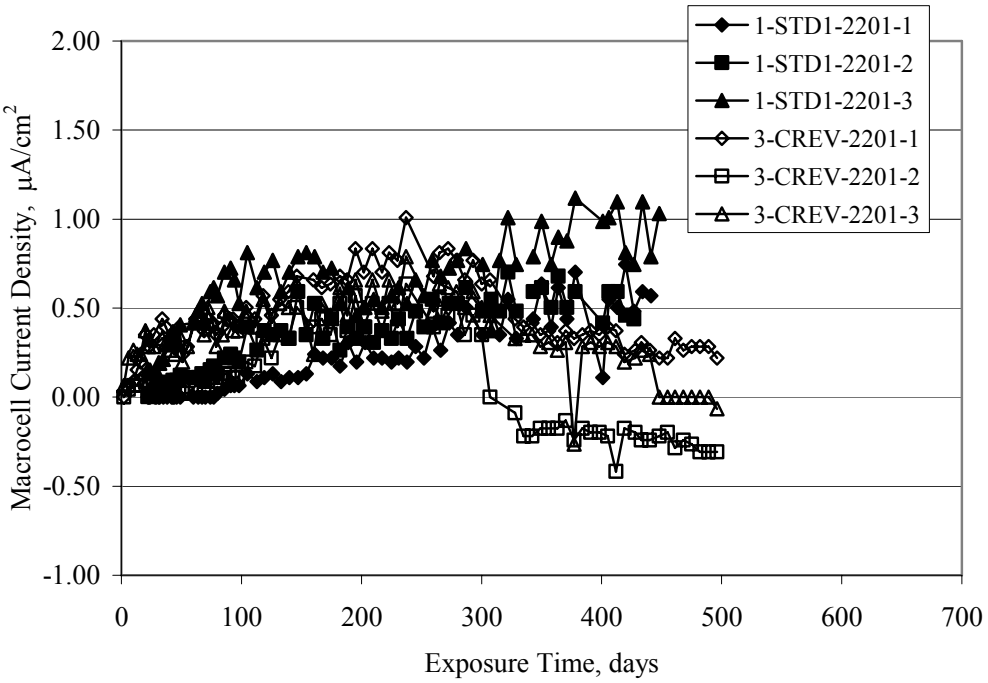

Figure 4.95. Graph. Plot of macro-cell current density versus exposure time for STD1 concrete specimens with top mat crevice bars (splice) and 2201 reinforcement compared to ones with normal bar placement.

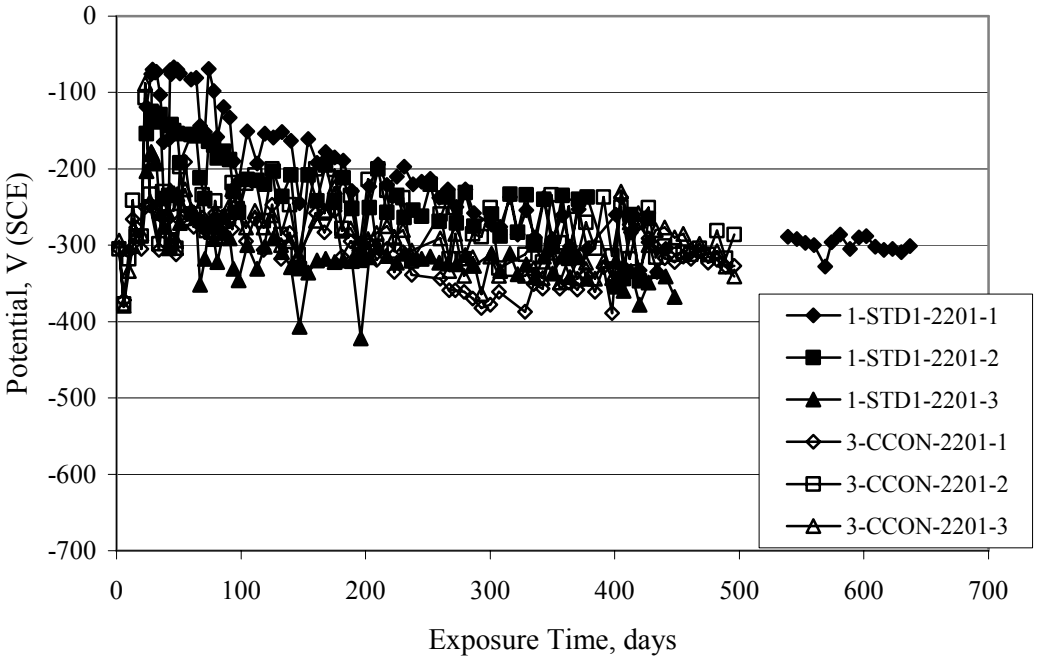

Figure 4.96. Graph. Plot of potential versus exposure time for STD1 concrete specimens with a simulated crack and 2201 reinforcement compared to uncracked ones.

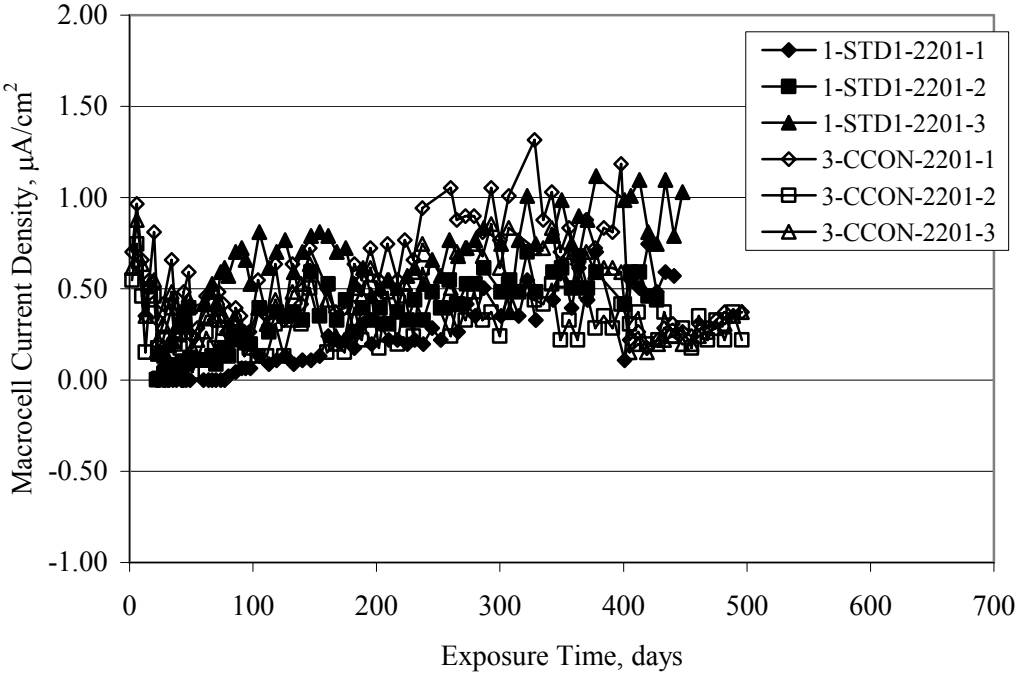

Figure 4.97. Graph. Plot of potential versus exposure time for STD1 concrete specimens with a simulated crack and 2201 reinforcement compared to uncracked ones.

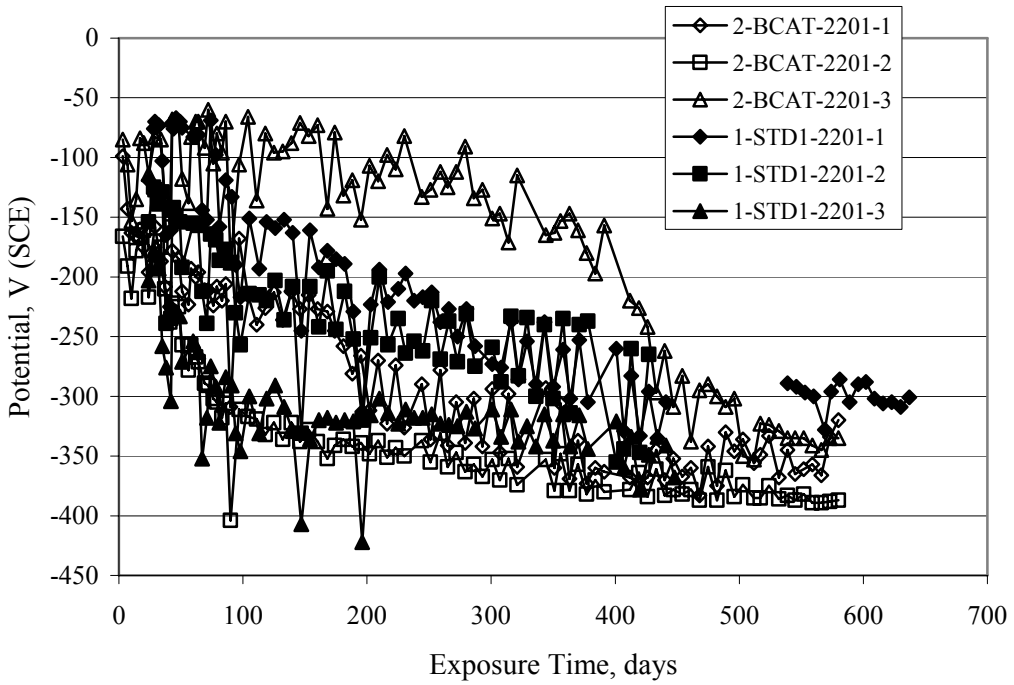

Figure 4.98. Graph. Plot of potential versus exposure time for STD1 concrete specimens with top mat 2201 bars and bottom mat black bar compared to ones with all 2201 bars.

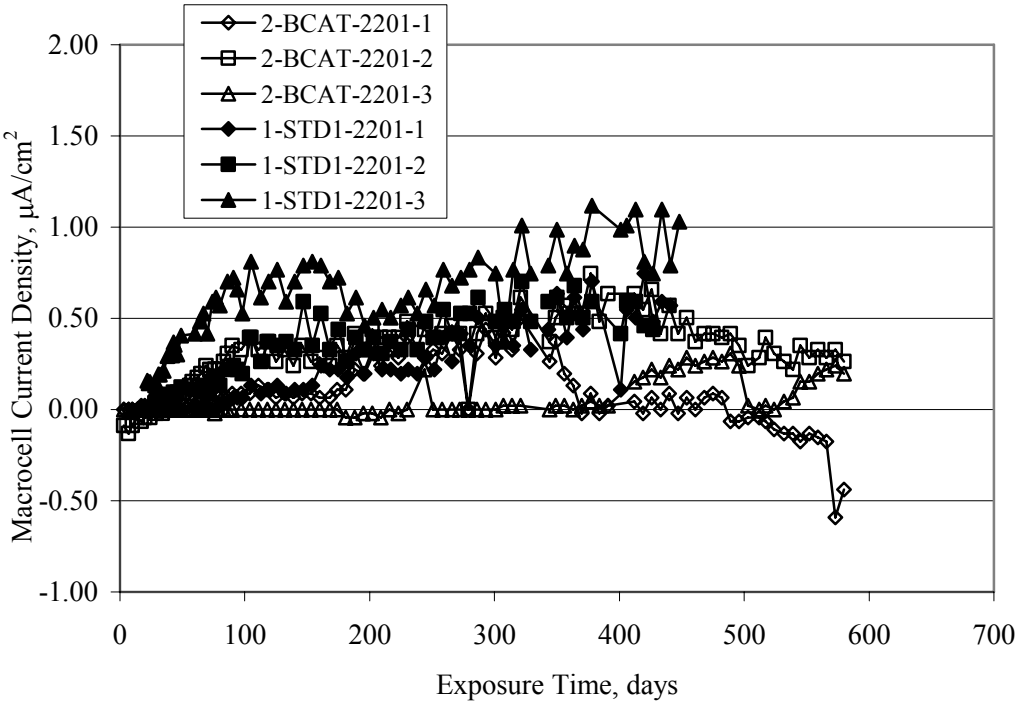

Figure 4.99. Graph. Plot of macro-cell current density versus exposure time for STD1 concrete specimens with top mat 2201 bars and bottom mat black bar compared to ones with all 2201 bars.

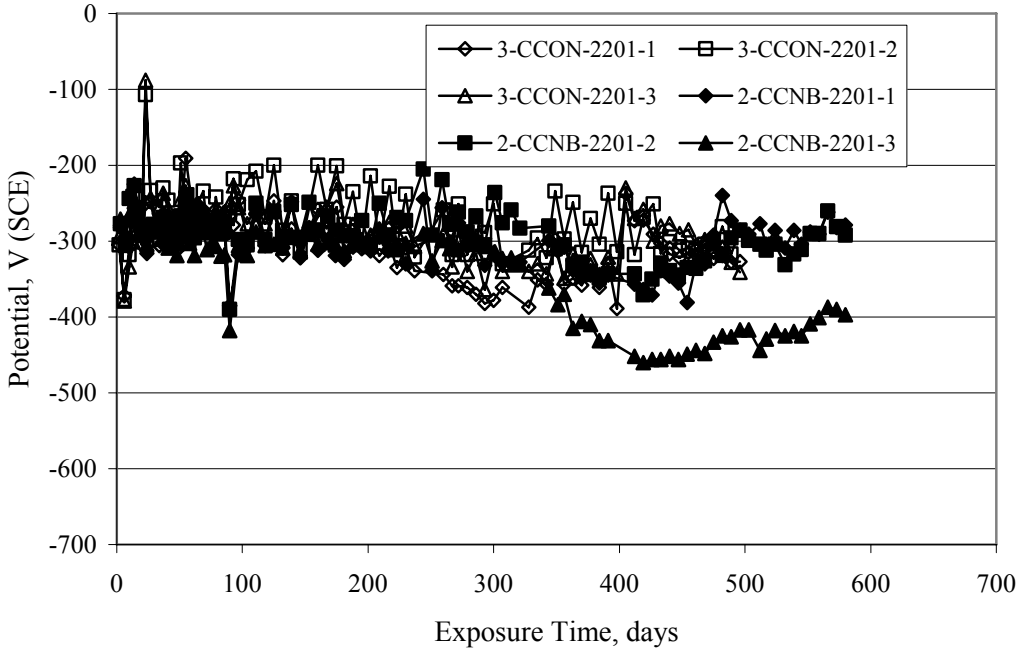

Figure 4.100. Graph. Plot of potential versus exposure time for STD1 concrete specimens with a simulated concrete crack and 2201 reinforcement compared to ones with a simulated crack and black bottom bars.

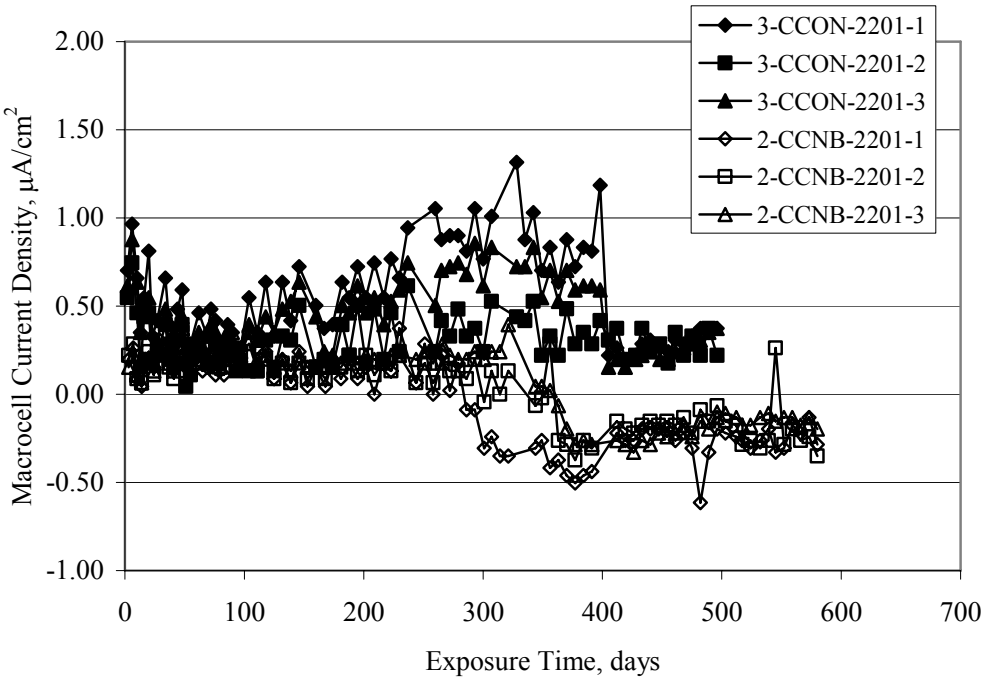

Figure 4.101. Graph. Plot of macro-cell current density versus exposure time for STD1 concrete specimens with a simulated concrete crack and 2201 reinforcement compared to ones with a simulated crack and black bottom bars.

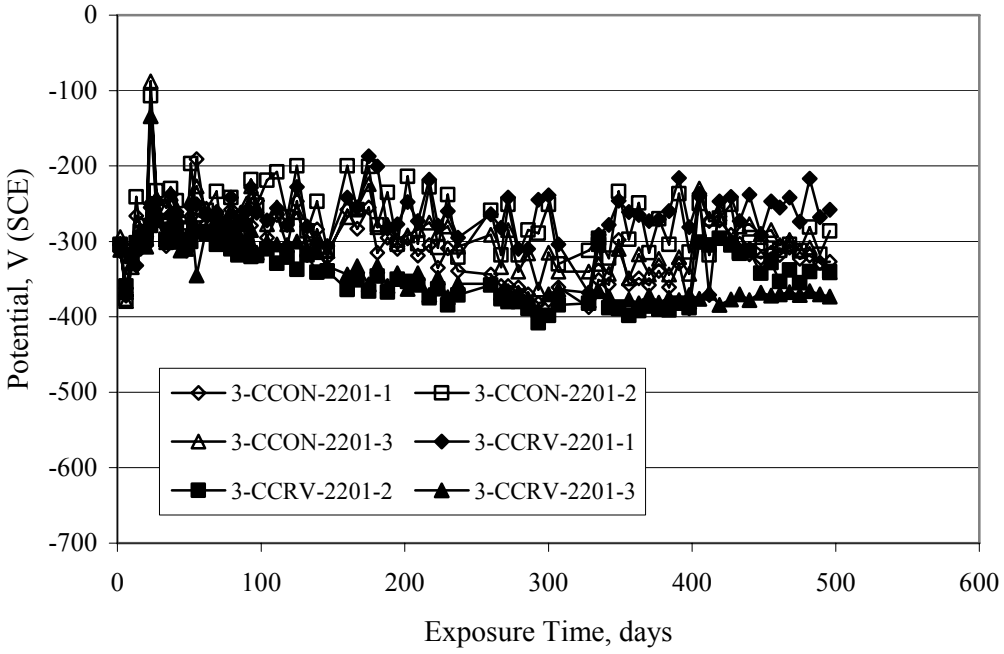

Figure 4.102. Graph. Plot of potential versus exposure time for STD1 concrete specimens with a simulated crack and crevice at top bars (splice) and 2201 reinforcement compared results for ones with cracked concrete and normal top bar placement.

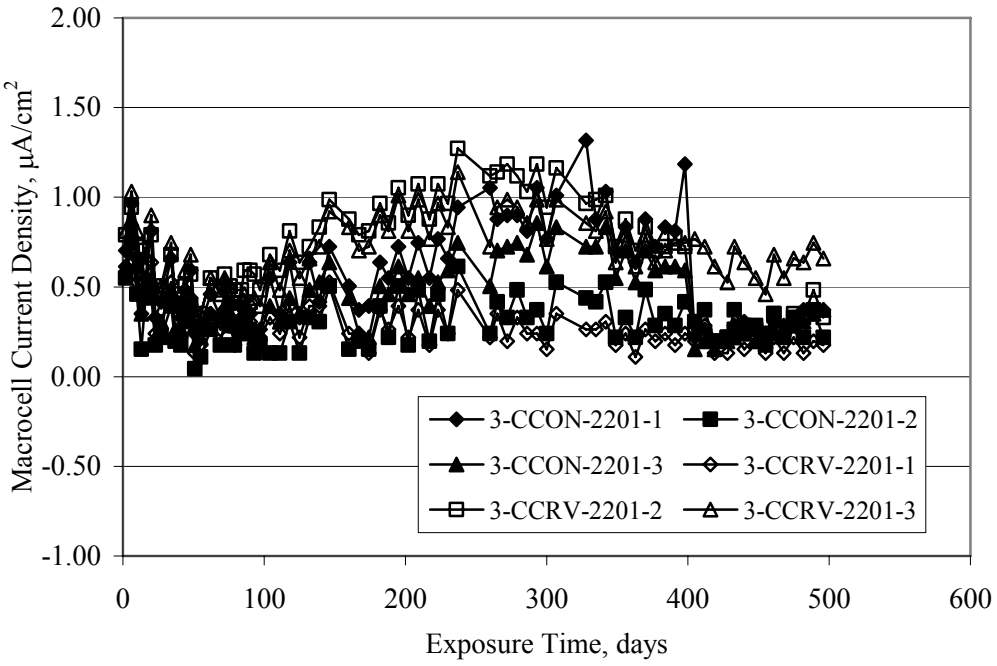

Figure 4.103. Graph. Plot of macro-cell current density versus exposure time for STD1 concrete specimens with a simulated crack and crevice at top bars (splice) and 2201 reinforcement compared results for ones with cracked concrete and normal top bar placement.

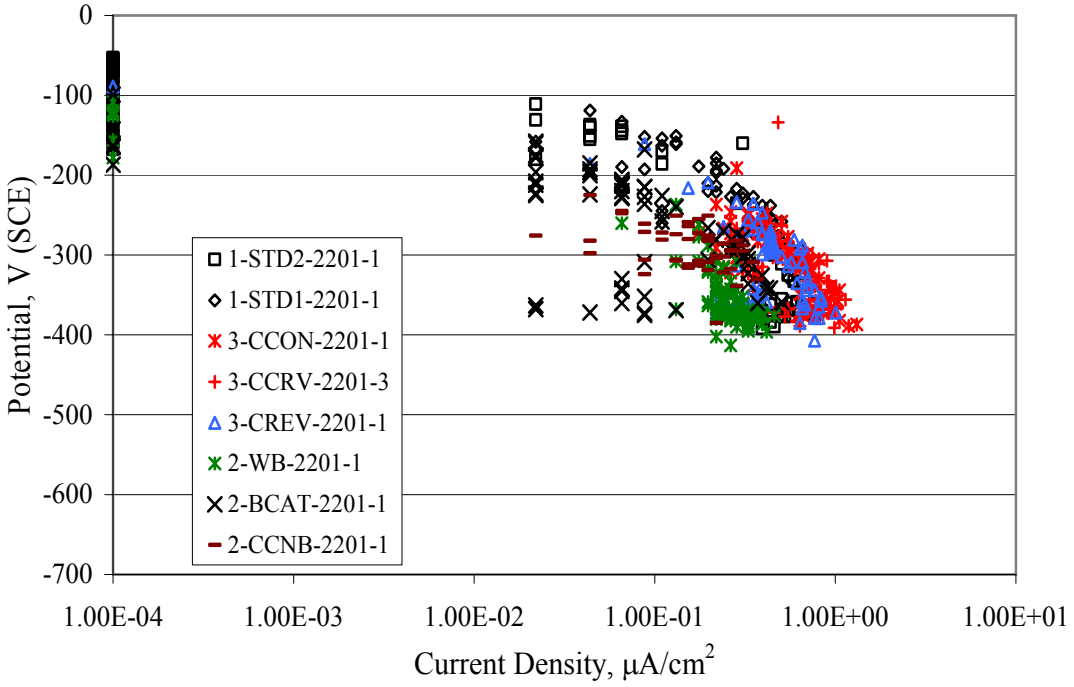

Figure 4.104. Graph. Plot of potential versus macro-cell current density for 2201 reinforced specimens.

Figure 4.105. Photo. Trace of the upper rebars and corrosion products on specimen number 1-STD1-2201-3.

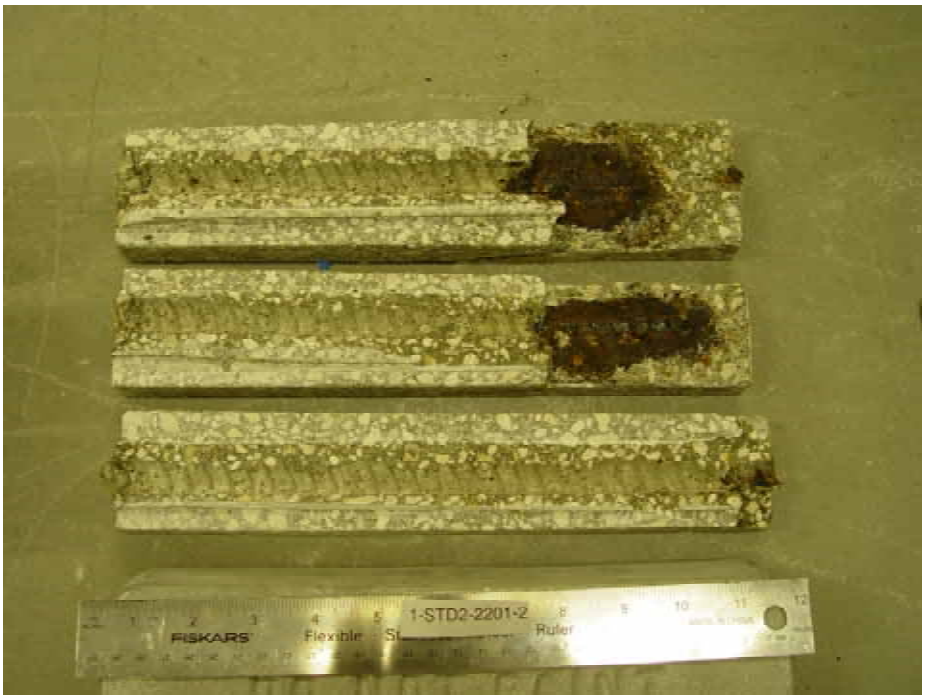

Figure 4.106. Photo. Trace of the upper rebars and corrosion products on specimen number 1-STD2-2201-2.

Figure 4.107. Photo. Trace of the upper rebars and corrosion products on specimen number 1-WB-2201-1.

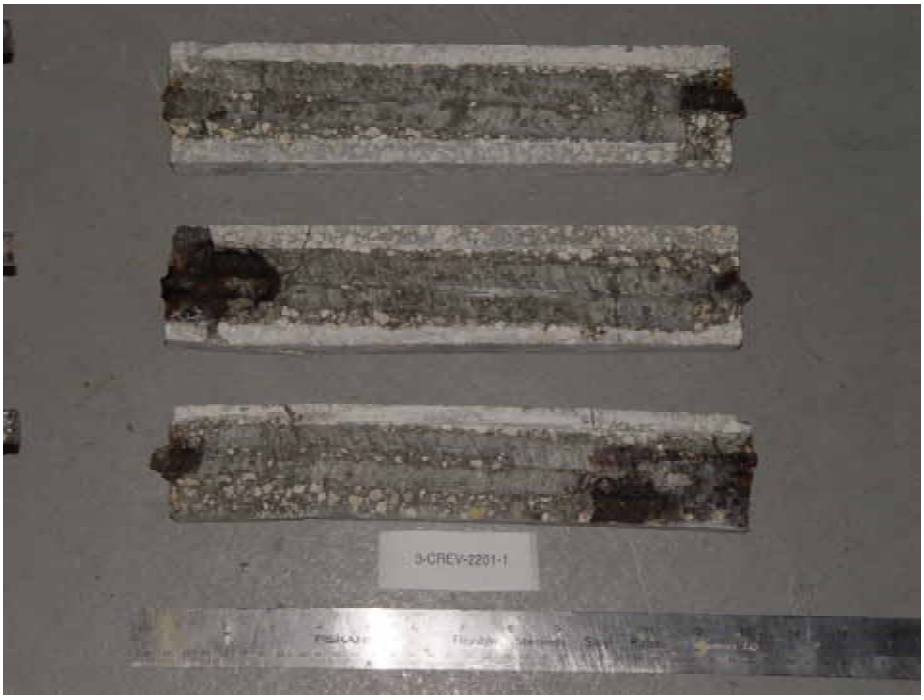

Figure 4.108. Photo. Trace of the upper rebars and corrosion products on specimen number 1-CREV-2201-1.

Figure 4.109. Photo. Trace of the upper rebars and corrosion products on specimen number 1-CCON-2201-1.

Figure 4.110. Photo. Trace of the upper rebars and corrosion products on specimen number 1-BCAT-2201-1.

Figure 4.111. Photo. Trace of the upper rebars and corrosion products on specimen number 1-CCNB-2201-1.

Figure 4.112. Photo. Trace of the upper rebars and corrosion products on specimen number 1-CCRV-2201-1.

Figure 4.113 compares on a single plot the average macro-cell current density versus average potential data for each three specimen set (standard specimens only) of reinforcement types black bar, 3Cr12, MMFX-II™, and 2201 and illustrates that these conform to different trends. For black bar slabs, it was considered that active corrosion commenced once potential dropped to −280 mV_{SCE}, at which point the average macro-cell current density was about 0.26 $\mu A/cm^2$. If it is assumed that this same current density denotes onset of active corrosion for the other reinforcement types as well, then the corresponding potentials are −390, −350, and −195 mV_{SCE} for 3Cr12, MMFX-II™, and 2201, respectively. These potentials were achieved after 35 days (black bar), 64 to 140 days (3Cr12), 91 to 140 days (MMFX-II™), and 64 to 94 days (2201).

Slabs Reinforced With 316 Solid and Clad (Stelax) Stainless Bars

Figures 4.114 and 4.115 show plots of potential and macro-cell current density, respectively, for the standard solid and Stelax clad stainless steel specimens in comparison to that for the black bar ones. This reveals a general trend where potential of the stainless steel specimens tended to become more positive with exposure time with all specimens conforming to a common band. Macro-cell current density has remained nil throughout the exposures. Data for the BCAT, CREV, CCON, CCRV, and CCNB specimen types are not presented since potentials conformed to the same scatter band as for the standard specimens (figure 4.114), and macro-cell current density was nil in all cases.

Thus, for the standard specimen simulated deck slab configuration the reinforcement types rank from best to worst, as:

$$316 \approx \text{Stelax} >> 2201 > \text{MMFX-II™} > 3Cr12 > \text{Black Bar}. \quad (4.2)$$

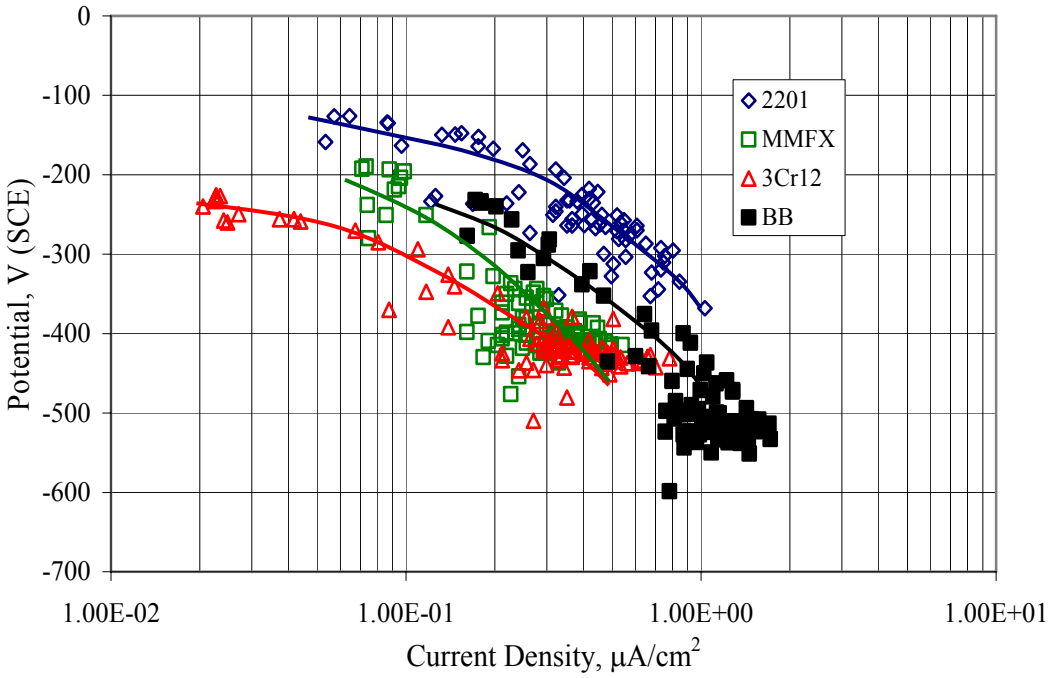

Figure 4.113. Graph. Plot of average potential versus average macro-cell current density at each measurement time for three specimens of the four indicated reinforcement types.

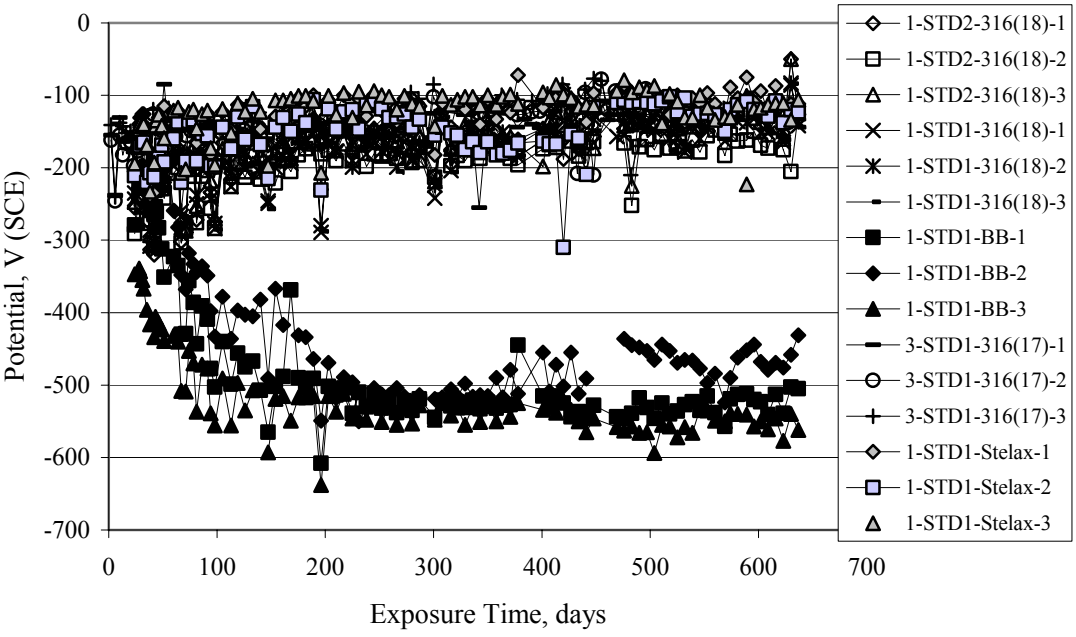

Figure 4.114. Graph. Plot of potential versus exposure time for STD1 and STD2 concrete specimens with 316.18, 316.17, and Stelax reinforcement compared to that for black bar in STD1 concrete.

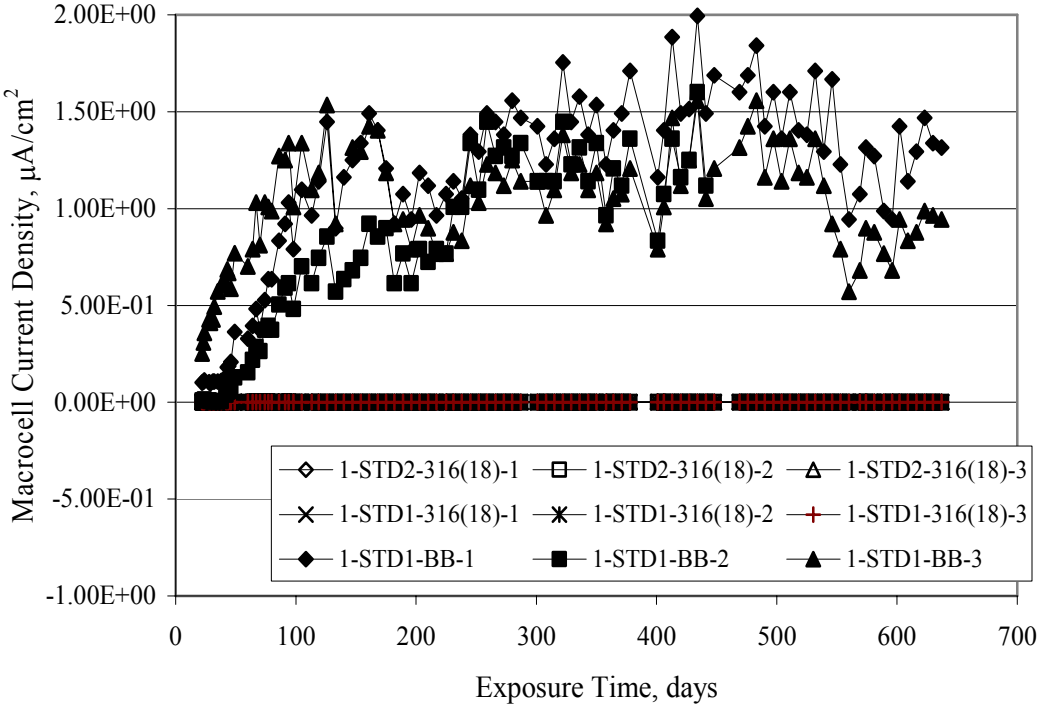

Figure 4.115. Graph. Plot of macro-cell current density versus exposure time for STD1 and STD2 concrete specimens with 316.18 reinforcement compared to ones with black bar in STD1 concrete.

Chloride Concentration

At several times during the exposures, 76 mm diameter cores were taken at the mid-spacing between bars in two of the reinforced STD1 concrete slabs and from blank (nonreinforced) slabs that underwent the same ponding as the reinforced ones. The cores were then sliced, the slices ground to powder, and the powder analyzed for acid soluble [Cl^-] using the FDOT standard method.[19] Figure 4.116 shows the results as a plot of [Cl^-] versus time and indicates that sorption probably contributed to transport of this species in the early stages of the exposures ([Cl^-] = 0.65 kg/m^3 after a single ponding cycle (14 days)). Also apparent is that relatively high Cl^- concentrations resulted during the time frame of the exposures ([Cl^-] ≈ 5 kg/m^3 after about 100 days and 10 kg/m^3 after 300 days).

Three Bar Columns

Square Three Bar Column Specimens

Figure 4.117 presents a time-to- corrosion (defined as potential achieving −280 mV_{SCE}) bar graph for all the S3BC specimens, where each bar in the plot represents the average of two or more specimens. In the case where corrosion has commenced for only one specimen, the total number of days of exposure is shown. The data indicate the following:

1. Black bar specimens had the shortest time-to-corrosion irrespective of mix design. This includes all six STD1 and STD2 specimens.

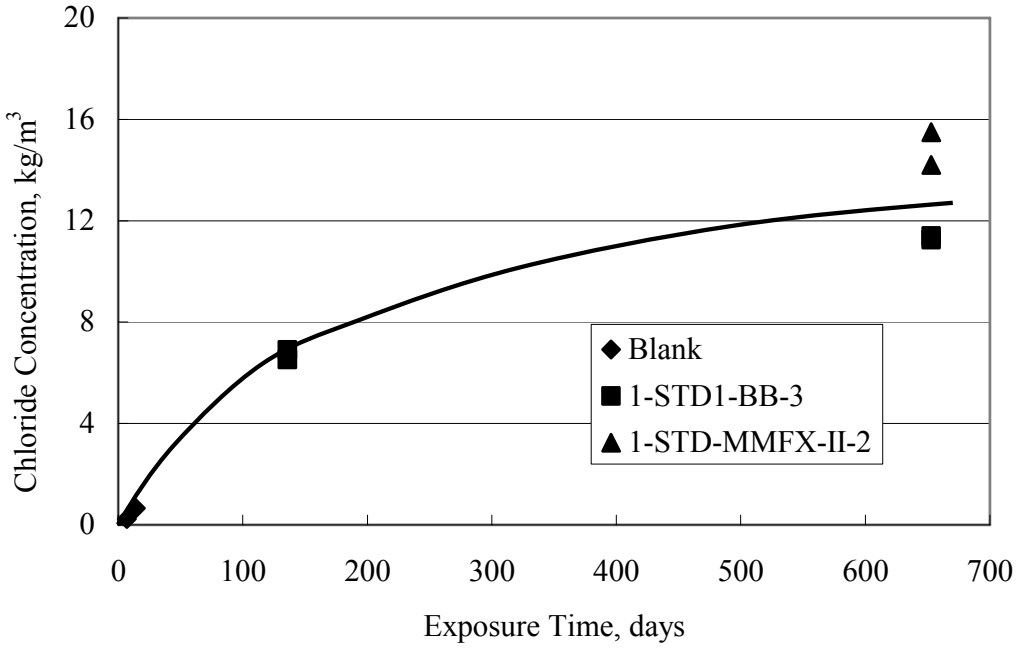

Figure 4.116. Graph. Plot of chloride concentration at 2.54 cm below the exposed surface of STD1 concrete slabs versus exposure time.

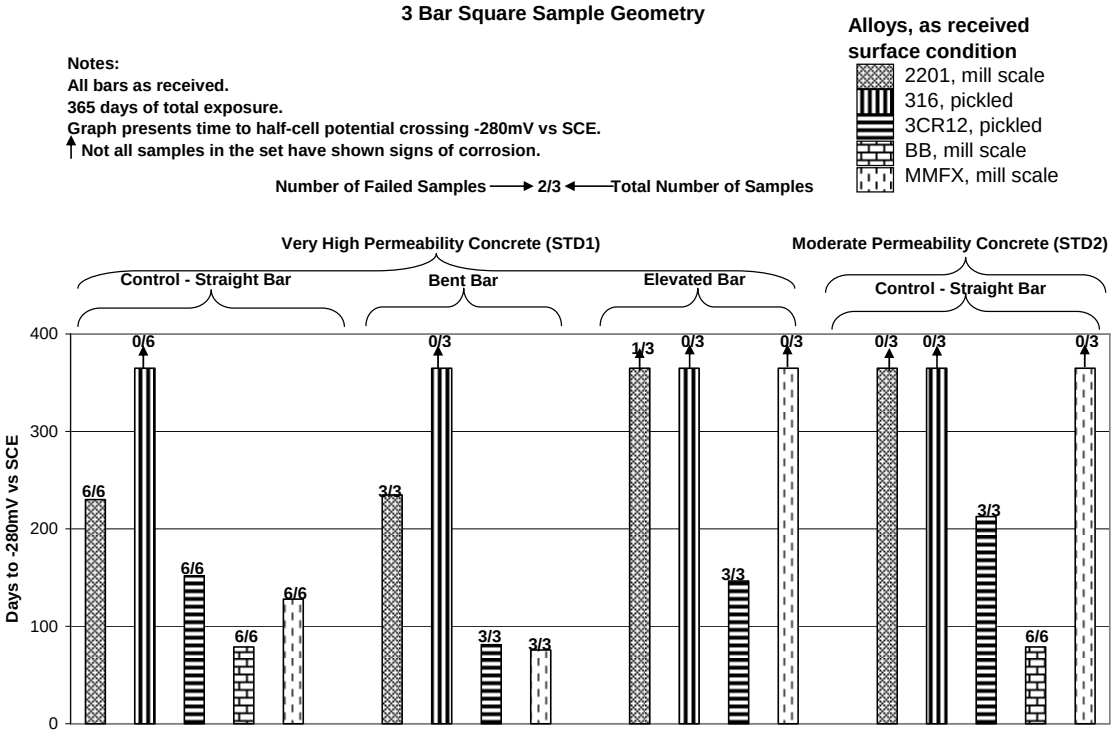

Figure 4.117. Graph. Time-to-corrosion results for square 3-bar column specimens.

2. All 3Cr12 specimens initiated corrosion, irrespective of mix design and specimen type.

3. Specimens reinforced with MMFX-II™ exhibited performance that was equivalent to 3Cr12 in the most aggressive conditions (control and bent bar groups) but outperformed 3Cr12 in the least aggressive cases (elevated bar and STD2 standard).

4. The 2201 reinforced specimens exhibited greater times-to-corrosion for all bars except 316.

5. Irrespective of concrete quality and specimen type, only 316 stainless steel has not initiated corrosion.

6. Bending the anode bar did not appear to have any effect on the time-to-corrosion of 316 and 2201 stainless steel reinforcements; but time-to-corrosion of 3Cr12 and MMFX-II™ was reduced by 47 and 41 percent, respectively.

7. Elevating the bar in the three bar columns resulted in a greater time-to-corrosion compared to the normal configuration (figures 3.19 and 3.20). However, all 3Cr12 and one 2201 specimen initiated corrosion in this configuration.

8. All reinforcement types performed better in the STD2 concrete than STD1 except for black bar, for which no difference was observed.

9. The following ranking resulted based on the time required for potential to shift to −280 mV_{SCE} or more negative (best to worst):

$$316 >> 2201 > \text{MMFX-II™} > 3Cr12 > \text{Black Bar.} \tag{4.3}$$

This is the same as for the simulated deck slab specimens, as indicated above, given that Stelax bars were not included in the three bar column test matrix.

Three Bar Tombstone Columns

Exposure of these specimens only commenced recently; and so there has been insufficient time to acquire meaningful results.

Macro-Cell Slab (MS) Specimens

Figure 4.118 shows a graph of typical potential and current trends with exposure time for macro-cell slab specimens (MMFX-II™ in uncracked STD1 concrete in this case). The same criterion for defining corrosion initiation and time-to-corrosion was used as for the square three bar column specimens (potential ≤ −280 mV_{SCE}). However, in cases where a measurable macro-cell current increase occurred at a different time, corrosion initiation was defined as the time at which this current was detected. For this specimen group, specimen A initiated corrosion at 212 days, B at 69 days, and C after 231 days, for an average of 171 days.

Figure 4.119 shows time-to-corrosion data for STD1 MS specimens without a simulated crack. Based upon these results, the following conclusions were reached:

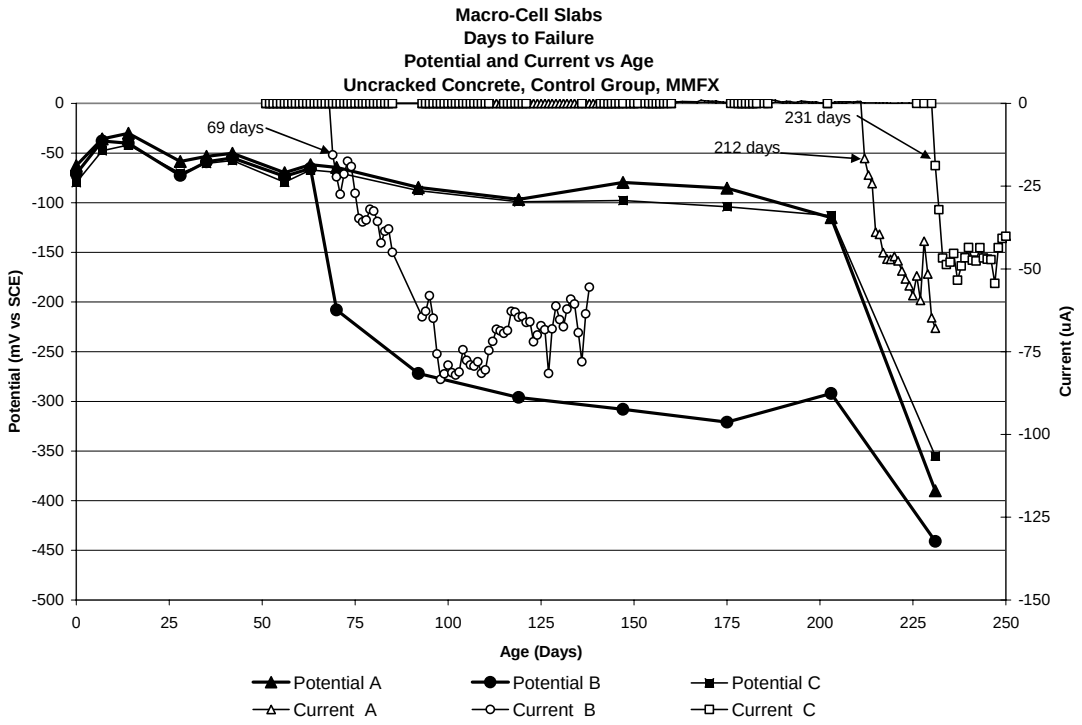

Figure 4.118. Graph. Example potential and current data for macro-cell slab specimens.

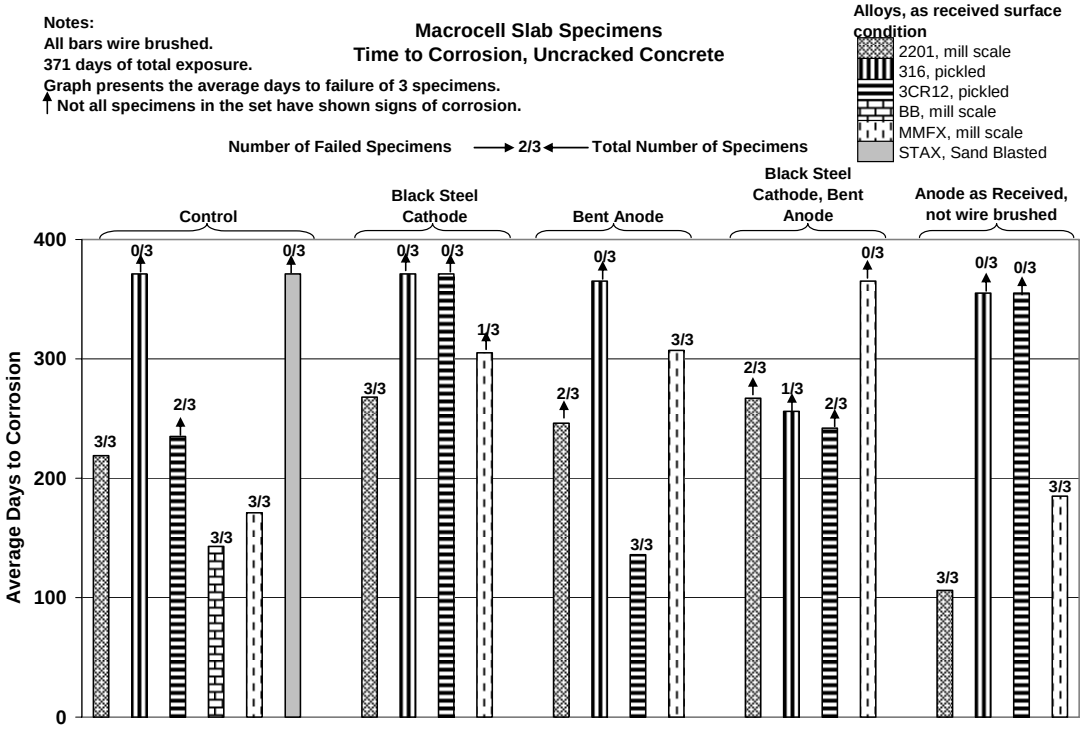

Figure 4.119. Graph. Time-to-corrosion results for the macro-cell slab specimens without a simulated crack.

1. Control STD1 specimens reinforced with black steel exhibited the shortest time-to-corrosion (black steel was not included in the other specimen types except as the cathode bar in the black steel cathode group). Ranking of the different reinforcements in the standard or control specimens was as listed below (best to worst):

   316 ≈ Stelax > 3Cr12 > 2201 >MMFX-II™> Black Bar. (4.4)

   This ordering is the same as for the simulated deck slab and three bar column specimens with the exception that 3Cr12 outperformed 2201 and MMFX-II™. Apparently, the fact that bars in the macro-cell slab specimens were wire brushed was responsible for this, although it cannot be ruled out that the difference in specimen design also may have been a factor. This performance reordering is surprising in the sense that wire brushing of the pickled 3Cr12 was of greater benefit than wire brushing of the as-rolled 2201. Time-to-corrosion of MMFX-II™ was essentially the same in each of the two surface conditions.

2. Reinforcements 3Cr12, MMFX-II™, and 2201 in the BCAT specimen configuration, exhibited greater times-to-corrosion than the corresponding controls. The reason for this improvement is unclear but will be investigated when the specimens are autopsied.

3. The 3Cr12, MMFX-II™, and 2201 reinforcements in the BNTB configuration (see table 3.7) all exhibited greater times-to-corrosion than did the respective controls (the improvement may not be significant in the case of 3Cr12), suggesting that the advantageous feature of either the BENT or BCAT configuration was retained in combination.

4. The best performance for each specimen type was exhibited by the 316 reinforcement. However, corrosion apparently initiated in one of the 316 BNTB specimens after approximately 260 days.

Figure 4.120 shows results for specimens with a simulated crack using the same format as in figure 4.119. This indicates that time-to-corrosion for black bar and 3Cr12 reinforced specimens was either relatively short (control specimens) or nil (BCAT and BENT configurations). The same was true for MMFX-II™ in the BNTB specimens. Otherwise, time-to-corrosion for the MMFX-II™ and 2201 specimens was comparable in general terms with that for the uncracked specimens. With the one exception noted above, none of the 316 reinforced specimens have initiated corrosion.

Field Columns

The field columns have been exposed for only 4 months. Currently, initial readings are all that are available, so there are no observations that can be made at this time.

Correlation of Concrete Specimen Data With Results From Accelerated Testing

Figure 4.121 shows a plot of time-to-corrosion for simulated deck slab and square three bar column specimens as a function of $\left[Cl^-_{th}\right]$, as determined from the AST-2A experiments. This reveals a general trend where, with the exception of the 2201 simulated deck slab data, time-to-

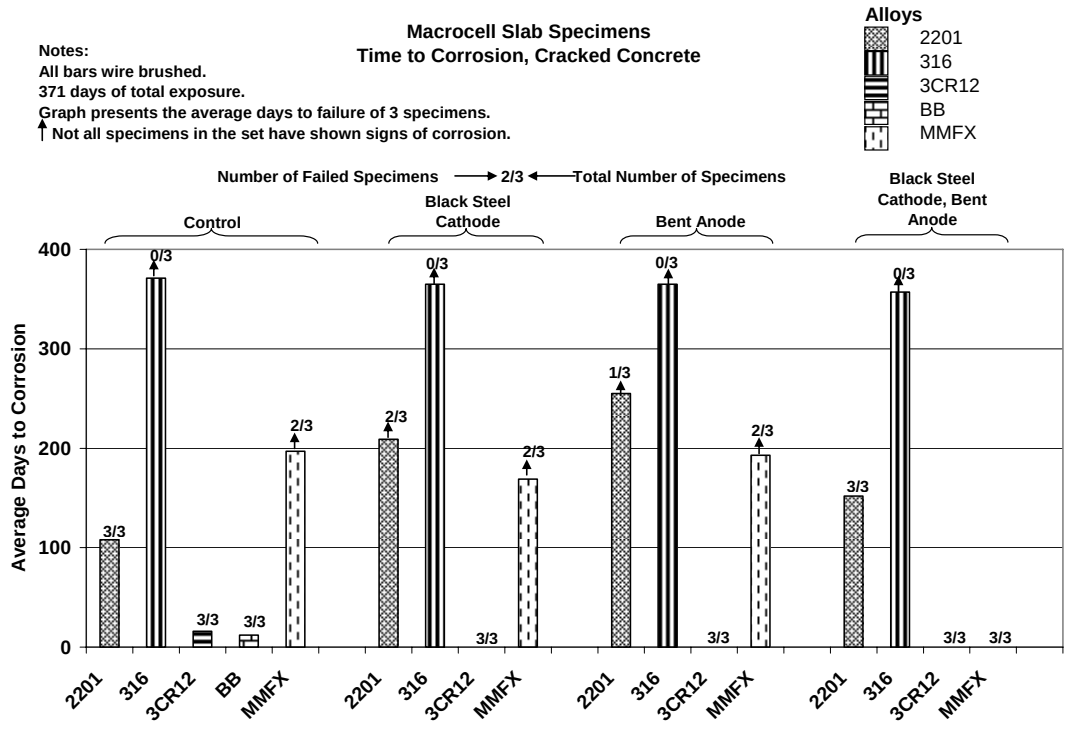

Figure 4.120. Graph. Time-to-corrosion results for the macro-cell slab specimens with a simulated crack.

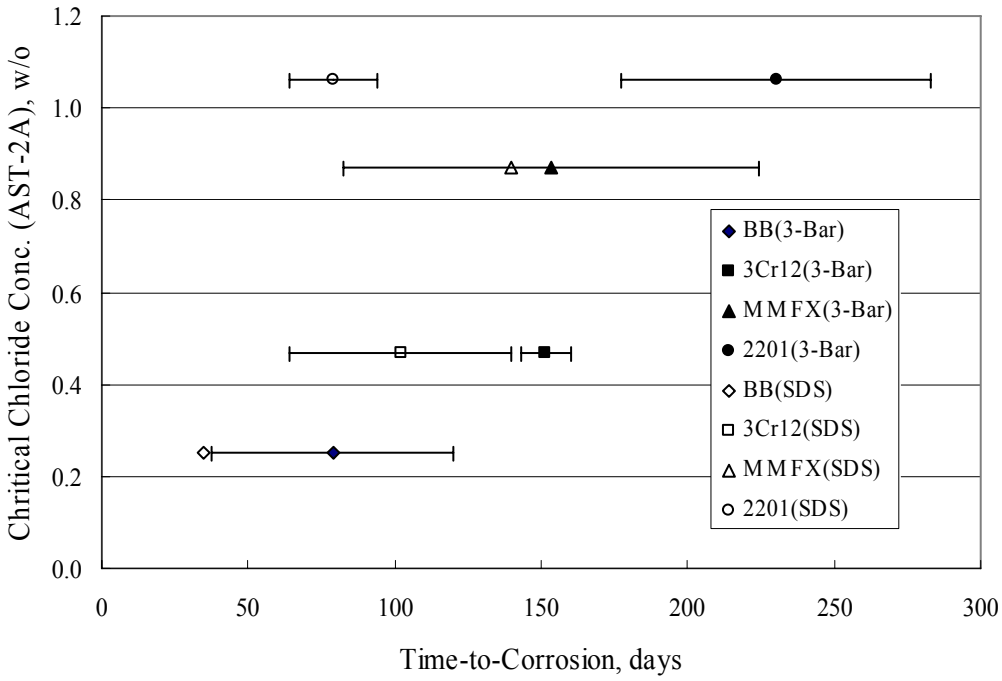

Figure 4.121. Graph. Plot of time-to-corrosion of reinforced concrete specimens as a function of $\left[Cl^-_{th}\right]$ as determined from accelerated testing.

corrosion increased in proportion to $\left[Cl^-_{th}\right]$. The error bands for the three bar column data correspond to one standard deviation, whereas for the simulated deck slabs these correspond to the data range. In comparing results for the two specimen types, the fact that corrosion of the simulated deck slab rebars may have initiated at or near the concrete interface because isolation was not provided here may have affected the results for these specimens. For most bar types in these specimens, concrete cracking, once this occurred, was along the line of the reinforcement; however, in the specific case of the 2201 specimens, cracking often occurred diagonally at the corners. This appeared to have resulted from corrosion of rebar near the concrete surface. Figure 4.122 is a photograph of an example case of this cracking. Subject to this limitation, the fact that time-to-corrosion increased in proportion to $\left[Cl^-_{th}\right]$ supports applicability of the AST-2A potentiostatic test method for projecting long-term reinforced concrete corrosion performance.

Figure 4.122. Photo. Example of corner cracking on a 2201 reinforced simulated deck slab specimen.

A calculation of time-to-corrosion, T_i, of STD1 concrete specimens was made based upon the $\left[Cl^-_{th}\right]$ projected for concrete from the AST-2A data (figure 4:31) using the one-dimensional solution for Fick's second law,

$$\frac{C_s - \left[Cl^-_{th}\right]}{C_s - C_0} = \text{erf}\left[\frac{x}{2\sqrt{D_e \cdot T_i}}\right], \tag{4.5}$$

where C_s is $[Cl^-]$ at the exposed concrete surface, C_0 is the initial $[Cl^-]$ in the concrete, and D_e is the effective diffusion coefficient. A determination of D_e was made from the average of two Cl^- profiles obtained after 136 days of exposure (see figure 4.116), which are shown in figure 4.123, using a least squares best fit algorithm to equation 4.4. This yielded a D_e of $3.20 \cdot 10^{-11}$ m^2/s. Inputs to the Fick's second law solution, in addition to this value for D_e, were cover $2.54 \cdot 10^{-2}$ m and C_s 18 kg/m^3. Table 4.6 lists the calculated time-to-corrosion for black bar, 3Cr12, MMFX-II™, and 2201. The projected times-to-corrosion are in general agreement with the measured values for concrete specimens (figure 4.121) with the exception of the 2201 reinforced simulated deck slab specimens, the reason being as discussed above.

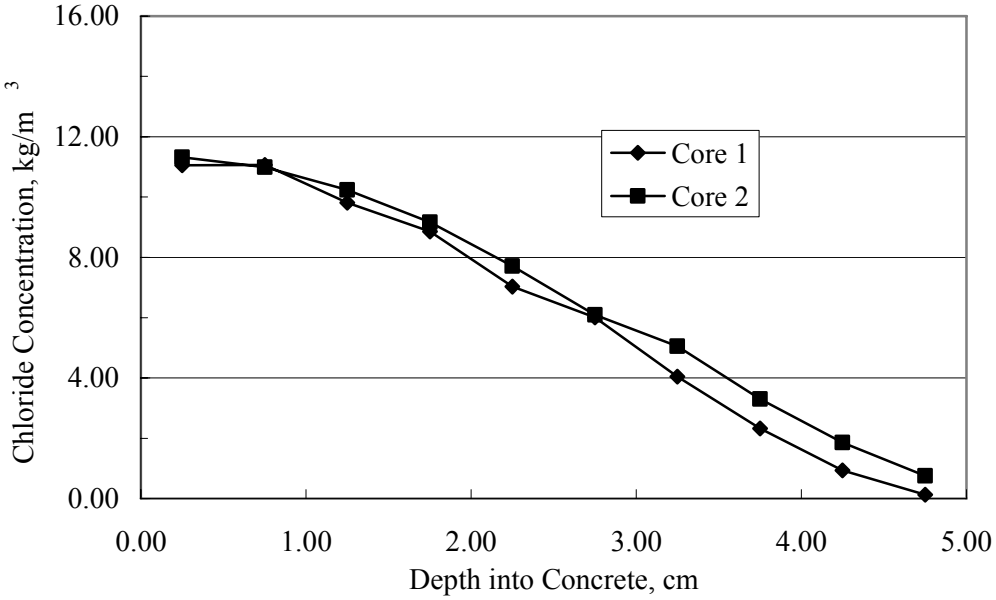

Figure 4.123. Graph. Chloride profile from each of two cores taken from STD1 concrete slabs after 136 days of exposure.

Table 4.6. Calculated times-to-corrosion for concrete specimens.

Bar Type	Cth, w/o cement (Figure 4:30)	Calculated Time-to-Corrosion, days
BB	0.65	81
3Cr12	0.88	99
MMFX	1.22	128
2201	1.34	138

5. CONCLUSIONS

Both short-term laboratory experiments in simulated pore solutions and long-term exposure of concrete specimens reinforced with corrosion resistant rebars exposed to chlorides were performed. The reinforcements included UNS-S31603 (Type 316L stainless steel (SS)), UNS-31803 (Type 2205 SS), ASTM A055-98 (Type 2201LDX SS), UNS-S41003 (Type 3Cr12 SS), ASTM A615, Grade 75 (MMFX-II™), two 316 SS clad steels (Stelax and SMI), and ASTM A615 (black bar). The following conclusions were reached based on results during the initial 3 years of this 5-year study:

1. For Accelerated Screening Test-1 (AST-1), which involved measurement of polarization resistance and weight loss of bars exposed to repetitive 1.75 hours wet—4.25 hours dry cycles in synthetic pore solution with chlorides for a total of 84 days, 316L SS solid bars performed best and black bars the worst. Corrosion rate for the other bars was intermediate and shared a common scatter band. Performance of the clad bars was mixed in that data for some specimens without intentional clad defects approached that of the solid 316L SS, whereas with clad defects polarization resistance approached that of the black bars.

2. Accelerated Screening Test-2A (AST-2A) involved exposure of specimens that were potentiostatically polarized to +100 mV_{SCE} in synthetic pore water to which chlorides were incrementally added. Corrosion initiation was defined as having occurred when current density reached 10 $\mu A/cm^2$. For bars that became active, the average critical Cl^- concentration for corrosion, $\left[Cl^-_{th}\right]$, was 0.25 weight percent (w/o) Cl^- (black bar), 0.47 w/o Cl^- (3Cr12), 0.87 w/o Cl^- (MMFX-II™), and 1.06 w/o Cl^- (2201). By comparison of the presently determined $\left[Cl^-_{th}\right]$ values with those from the literature that were acquired using pore water expression from specimens for which companion chloride thresholds in concrete, C_T, were available, C_T of black bar was projected as 0.54 w/o, for 3Cr12 0.80 w/o, for MMFX-II™ 1.10 w/o, and 2201 1.30 w/o (cement weight basis). A comparison between the AST-1 and AST-2A data indicated that rebars with a polarization resistance greater than $6 \cdot 10^4$ ohm·m^2 had a $\left[Cl^-_{th}\right]$ greater than 5 w/o, whereas below this $\left[Cl^-_{th}\right]$ was about 1 w/o or less. It was unclear if the $\left[Cl^-_{th}\right]$ could be predicted from the Pitting Resistance Equivalent Number (PREN).

3. Three types of reinforced concrete specimens, simulated deck slabs, three bar columns, and macro-cell slabs, have been under either continuous or cyclic wet-dry ponding with a NaCl solution for over 600 days. Similar to the accelerated tests, the best corrosion resistance was exhibited by the 316L reinforcement (both solid and clad); however, no 2205 SS bars have been tested in concrete. For bars with poor or intermediate performance in the accelerated tests (black bar, 3Cr12, MMFX-II™, and 2201), time-to-corrosion in concrete increased in proportion to $\left[Cl^-_{th}\right]$ as determined in the accelerated AST-2A tests. The ranking (best to worst) was:

$$316 \approx \text{Stelax} >> 2201 > \text{MMFX-II™} > 3Cr12 > \text{Black Bar}, \tag{4.2}$$

except for the macro-cell slab specimens where the 3CR12 exhibited longer times-to-corrosion than either 2201 or MMFX-II™. This may have been because these bars were wire brushed; however, if this is the explanation, then wire brushing the pickled 3Cr12 resulted in greater corrosion resistance enhancement than wire brushing the as-rolled 2201 or MMFX-II™.

4. In general, time-to-corrosion of the different reinforcements in concrete increased in direct proportion to the chloride threshold that was determined by accelerated testing (AST-2A).

5. Additional data are still being collected for the concrete specimens with various types of reinforcement that remain under test. Final analysis based on non-destructive data and observed condition of dissected specimens may change the ranking which will be documented in the final report.

APPENDIX A

EXAMPLE PH CALCULATION

From equation 3.1,

$$pH = 14+\log (\gamma_{OH}\cdot[OH^-]), \tag{3.1}$$

where γ_{OH} is the activity coefficient for OH^-, which was taken as 0.7, and $[OH^-]$ is molality of that species. Thus, assuming [OH-] = 0.1,

$$pH = 14+\log (0.7\cdot 0.1) = 14+(\cdot\ 1.15) = 12.85.$$

APPENDIX B

EXAMPLE CALCULATION OF CORROSION RATE FROM POLARIZATION RESISTANCE

Corrosion rate, CR, was calculated from the measured polarization resistance, PR, using a modified form of the Stern-Geary equation,

$$CR = 3.15 \cdot 10^{7} \cdot \frac{Z}{n \cdot F \cdot \rho} \cdot \frac{B}{PR}, \tag{3.2}$$

where Z is atomic weight, n is the number of electrical equivalents, F is Faraday's constant, ρ is alloy density, and B is a term the value for which depends on the Tafel constants. For the case of black bar reinforcing steel, a typical measured value for PR was 10^3 Ω·cm^2. Thus, with values for the other constants as,

Z = 56 grams/mol,
n = 2 equivalents,
F = 96,500 Coulombs/mol·equivalent,
ρ = 7.87 grams/cm^3, and
B = 0.026 V,

$$CR = 3.15 \cdot 10^{7} \cdot \frac{56}{2 \cdot 96{,}500 \cdot 7.87} \cdot \frac{0.026}{10^{3}} = 0.03 \text{ cm/year} = 0.3 \text{ mm/year}$$
$$= 12 \text{ mils/year.}$$

APPENDIX C

EXAMPLE CALCULATION OF CORROSION RATE FROM WEIGHT LOSS DATA

The average corrosion rate, CR, over the exposure duration was determined from before and after specimen weight measurements using the expression,

$$CR = \frac{W}{\rho \cdot A \cdot T}, \tag{3.3}$$

where W is weigh loss, ρ is metal density, A is exposed rebar specimen surface area, and T is exposure time. From the density of iron (steel) and typical experimental parameters:

W = 1.6 grams
$\rho = 7.87 \cdot 10^{6}$ grams/m^3,
$A = 76 \cdot 10^{-4}$ m^2, and
T = 0.0767 years (28 days),

$$CR = \frac{1.6}{7.87 \cdot 10^{6} \cdot 76 \cdot 10^{-4} \cdot 0.0767} = 349 \cdot 10^{-6} \text{ m/year}$$

$$= 0.39 \text{ mm/year} = 15 \text{ mils/year.}$$

BIBLIOGRAPHY

[1] Virmani, Y.P; Jones, W.R.; and Jones, D.H., *Public Roads,* Vol. 84(3), 1984, p. 96.

[2] Koch, G.H.; Brongers, P.H.; Thompson, N.G.; Virmani, Y.P.; and Payer, J.H., "Corrosion Costs and Prevention Strategies in the United States," Report No. FHWA-RD-01-156, Federal Highway Administration, Washington, DC, March 2002.

[3] Yunovich, M.; Thompson, N.G.; and Virmani, Y.P., "Life Cycle Cost Analysis for Reinforced Concrete Bridge Decks," paper no. 03309 presented at CORROSION/03, March 10–14, 2003, San Diego.

[4] Stratfull, R.F.; Jurkovich, W.J.; and Spellman, D.L., Transportation Research Record, Vol. 539, 1975, p. 50.

[5] Code of Federal Regulations, Section 650.305, "Frequency of Inspections," U.S. Government Printing Office, revised April 1, 2002, Washington, DC.

[6] Tutti, K., *Corrosion of Steel in Concrete*, Report No. Fo 4, Swedish Cement and Concrete Research Institute, Stockholm, 1982.

[7] Stafford, R.T., "Epoxy Coated Rebars," *Parking*, March–April 1973, p. 39.

[8] Clifton, J.R.; Beehgly, H.F.; and Mathey, R.G., "Non-Metallic Coatings for Concrete Reinforcing Bars," Report No. FHWA-RD-74-18, Federal Highway Administration, Washington, DC, February 1974.

[9] Virmani, Y.P.; and Clemena, G.G., "Corrosion Protection: Concrete Bridges," Report No. FHWA-RD-98-088, Federal Highway Administration, Washington, DC, September 1998.

[10] Powers, R.G.; and Kessler, R., "Corrosion Evaluation of Substructure, Long Key Bridge," Corrosion Report No. 87-9A, Florida Department of Transportation, Gainesville, FL, 1987.

[11] Powers, R.G., "Corrosion of Epoxy-Coated Rebar, Keys Segmental Bridges, Monroe County," Report No. 88-8A, Florida Department of Transportation, Gainesville, FL, August 1988.

[12] Zayed, A.M.; and Sagues, A.A., "Corrosion of Epoxy-Coated Reinforcing Steel in Concrete," Paper No. 386 presented at CORROSION/89, New Orleans, LA, April 21, 1989.

[13] Gustafson, D.P., "Epoxy Update," Civil Engineering, Vol. 58, No. 10, p. 38, 1988.

[14] Hartt, W.H.; Powers, R.G.; Leroux, V.; and Lysogorski, D.K., "A Critical Literature Review of High-Performance Reinforcements in Concrete Bridge Applications," Report No. FHWA-HRT-04-093, Federal Highway Administration, Washington, DC, July 2004.

[15] McDonald, J.B.; Pfiefer, D.F.; and Blake, G.T., *The Corrosion Performance of Inorganic-, Ceramic-, and Metallic-Clad Reinforcing Bars and Solid Metallic Reinforcing Bars in Accelerated Screening Tests*, Report No. FHWA-RD-96-085, Federal Highway Administration, Washington, DC, October 1996.

[16] Samson, E.; Lemaire, G.; Marchand, J.; and Beaudoin, J.J., "Modeling Chemical Activity Effects in Strong Ionic Solutions," *Computational Materials Science*, Vol. 15, Issue 3, pp. 285–294, August 1999.

[17] Hurley, M.F.; and Scully, J.R., "Threshold Chloride Concentrations of Selected Corrosion Resistant Rebar Materials Compared to Carbon Steel," paper no. 05259 presented at CORROSION/05, April 3–7, 2005, Houston.

[18] Li, L.; and Sagüés, A.A., *Corrosion*, Vol. 57, p. 19, 2001.

[19] Florida Department of Transportation, "Florida Method of Test for Determining Low Levels of Chloride in Concrete and Raw Materials," Designation FM 5-516, Florida Department of Transportation, Tallahassee, FL, September 1994.

Recycled
Recyclable

HRDI-10/07-07(700)E